MIR Difference-Frequency Laser Spectrometer for Industrial Process Control

D i s s e r t a t i o n
zur Erlangung des Grades eines Doktors
der Naturwissenschaften

Vorgelegt von

M.Sc. Alireza Khorsandi
aus Esfahan (Iran)

genehmigt von der
Mathematisch-Naturwissenschaftlichen Fakultät
der Technischen Universität Clausthal

Tag der mündlichen Prüfung
20.07.2004

Die vorliegende Arbeit wurde am Institut für Physik und Physikalische Technologien der Technischen Universität Clausthal angefertigt.

Vorsitzender der Prüfungskommission ..... Prof. Dr. D. Mayer

Hauptberichterstatter ..... Prof. Dr. W. Schade

Berichterstatter ..... Prof. Dr. D. Kip

*To **Mahdi** and **Ali** who are all the world to me*

Summary

The efficiency of combustion processes e. g. in glass melting furnaces depends on how the radiative heat energy is transferred from the combustion chamber to the glass melt. Sensing of a combustion system using in-situ and on-line spectroscopy of the molecular species in the atmosphere of a glass melting furnace provides a deep understanding of the combustion formation at any moment. Furthermore, rapid in-situ and on-line combustion monitoring requires nonintrusive spectroscopic techniques and devices which can be provided by high resolution **laser absorption spectroscopy**.

The carbon monoxide (CO) concentration in the atmosphere of a glass melting furnace is an effective and sensitive measure for optimizing the combustion process to avoid the formation of toxic gases such as NO_x emissions and to promote enough oxidant in the flame required for complete combustion. Therefore, the ability of the in-situ and on-line measurements of the CO concentration in the atmosphere of a glass melting furnace is of great interest. CO is an important combustion-generated species. Since it has strong fundamental absorption lines in the mid-infrared (MIR) spectrum (2000 to 2250 cm^{-1}), it can easily be traced by absorption spectroscopy with a narrow linewidth MIR laser source. From the available laser sources in the MIR spectral region such as quantum cascade lasers and optical parametric oscillators, an all solid-state difference-frequency laser is still an efficient light source in terms of narrow linewidth, broad tunability, room temperature operation and compactness in terms of applicability in an industrial environment.

The aim of the present work is the application of a MIR difference-frequency generation (DFG) laser to the industrial environment as gas sensor. The MIR laser radiation is obtained by difference-frequency mixing of two continuous wave diode-lasers as pump and signal sources in a silver thiogallate ($AgGaS_2$) nonlinear optical crystal through type I 90° noncritical phase-matching. The generated MIR laser radiation is centered at 5 μm. The tunability of the MIR wavelength is provided by proper setting of the temperature and the current of the diode-lasers and the temperature of the nonlinear crystal.

The efficiency of the generated MIR difference-frequency laser radiation is shown in the laboratory environment through room-temperature measurements of the self- and the collisional-broadening coefficients of the CO P(21) (at 2055.5 cm^{-1}) and CO P(27) (at 2027.649 cm^{-1}) absorption lines. The self-broadening coefficient of the NO molecule is also measured at room temperature by shifting the MIR DFG laser to the NO R(26) absorption line at 1955.67 cm^{-1}. This is done by improving the mode behavior of the diode-laser by developing an external short-cavity around the diode-laser pump source. The measured values for the broadening coefficients are in good agreement with the data given by the HITRAN 2003 database. The MIR DFG laser is then combined with the 3-dimensional computerized tomographic (CT) reconstruction technique to image the CO

concentrations in the flame of a methane/air flat flame McKenna burner. Results of the measured CO concentration in the flame are in good agreement with the data obtained with other methods as for example two-photon laser-induced fluorescence spectroscopy and chemical kinetic calculations.

Finally, in the industrial measurements the performance of the MIR DFG laser is shown with CO concentration measurements in the atmosphere of a gas fired glass melting furnace at the Dr. Genthe GmbH&CO. KG., Goslar. The measured CO concentration is found to be in agreement with a typical bypass measurements done by the "Hüttentechnische Vereinigung der Deutschen Glasindustrie". Compared to conventional gas sensor technology, the presented MIR DFG spectrometer applications offer numerous economic and ecologic benefits because of their potential of monitoring gas concentrations nonintrusive and on-line, and therefore this technique can be applied for active industrial process control.

Zusammenfassung

Die Effizienz eines Verbrennungsprozesses, z.B. in Glasschmelzöfen, hngt davon ab, wie die Strahlungsenergie von der Verbrennungskammer auf die Glasschmelze übertragen wird. Die Überwachung des Verbrennungssystems über die insitu und online Spektroskopie der molekularen Spezies in der Atmosphre eines Glasschmelzofens ermöglicht ein grundlegendes Verstndnis des Verbrennungsprozesses zu jedem Zeitpunkt. Weiterhin erfordert eine schnelle insitu und online Überwachung der Verbrennung nicht-invasive spektroskopische Techniken, die mit der hoch auflösenden Laserabsorptionsspektroskopie bereitgestellt werden knnen.

Die Kohlenstoffmonooxidkonzentration (CO) in der Atmosphäre eines Glasschmelzofens ist ein effektives und sensitives Maß für die Optimierung des Verbrennungsprozesses, um die Bildung von giftigen Gasen wie NO_x zu vermeiden und genügend Sauerstoff für eine vollstndige Verbrennung bereitzustellen. Demzufolge sind insitu und online Messungen von der CO-Konzentration in der Atmosphäre eines Glasschmelzofens von großem Interesse. CO ist ein wichtiges Verbrennungsgas. Da es starke fundamentale Absorptionsbanden im mittleren infraroten Spektralbereich (MIR) aufweist (2000 bis 2250 cm^{-1}), kann es leicht durch Absorptionsspektroskopie mit einer schmalbandigen MIR Laserstrahlquelle nachgewiesen werden. Fr eine Anwendung in industrieller Umgebung ist ein festkörperbasierter Differenzfrequenzlaser (DFG-Laser) verglichen mit den vorhandenen Laserquellen für den MIR-Bereich, wie beispielsweise Quantenkaskadenlaser und optisch parametrische Oszillatoren, eine effiziente Lichtquelle wegen seiner Schmalbandigkeit, weiten Durchstimmbarkeit, Betrieb bei Raumtemperatur und Kompaktheit.

Ziel der vorliegenden Arbeit ist die Anwendung einer MIR DFG-Laserquelle in einer industriellen Umgebung als Gassensor. Die MIR Laserstrahlung wird über Differenzfrequenzerzeugung mit zwei kontinuierlich emittierenden Diodenlasern als Pump- und Signalquellen in einem nichtlinearen optischen Silbergalliumsulfid-Kristall über Typ I nichtkritische Phasenanpassung generiert. Die erzeugte Strahlung hat eine Zentralwellenlnge von 5 μm. Die Durchstimmbarkeit wird durch geeignete Einstellung von Temperatur und Strom der Diodenlaser und der Kristalltemperatur erreicht.

Die Effizienz der erzeugten MIR Strahlung wurde in Laborumgebung durch Messungen der Selbst- und Fremdverbreiterungskoeffizienten der CO P(21) (bei 2055.500 cm^{-1}) und CO P(27) (bei 2027.649 cm^{-1}) Absorptionslinien bei Raumtemperatur demonstriert. Der Selbstverbreiterungskoeffizient des NO Moleküls wurde ebenfalls bei Raumtemperatur bestimmt, indem der Laser auf die NO R(26) Absorptionslinie bei 1955.650 cm^{-1} abgestimmt wurde. Dies wurde erreicht, indem das Modenverhalten des Pumplasers durch die Entwicklung eines externen Resonators verbessert wurde. Die gemessenen Werte für die Verbreiterungskoeffizienten sind in guter Übereinstimmung mit Werten aus der HITRAN 2003 Datenbank. Die MIR Strahlquelle wurde dann mit einer 3-dimensionalen computergesttzten tomographischen Rekonstruktionstechnik kombiniert, um CO-Konzentrationsprofile in der Methan/Luft-Flamme eines McKenna Brenners

aufzunehmen. Die gemessenen CO-Konzentrationen sind in guter Übereinstimmung mit Werten, die mit anderen Methoden, wie beispielsweise 2-Photonen-LIF-Spektroskopie oder chemisch kinetischen Berechnungen gewonnen wurden.

Schließlich wurde die Einsetzbarkeit des MIR DFG Lasers in industrieller Umgebung bei Messungen der CO-Konzentration in der Atmosphäre eines gasbefeuerten Glasschmelzofens bei der Dr. Genthe GmbH & Co KG in Goslar gezeigt. Die gemessene CO-Konzentration stimmt gut mit typischen Bypass-Messungen, die von der Hüttentechnischen Vereinigung der Deutschen Glasindustrie durchgeführt werden, überein. Im Vergleich mit konventioneller Gassensor-Technologie zeigt die Anwendung des MIR DFG Spektrometers zahllose konomische und ökologische Vorteile, da ein hohes Potential besteht, Gaskonzentrationen nicht-invasiv und online zu messen und somit eine aktive industrielle Prozesskontrolle ermöglicht wird.

Contents

Glossary

Latin Symbols

A_{kl}	Spontaneous decay rates
a	Voigt parameter
B	Rotational constants
B_{ij}	Einstein coefficient of $\|i\rangle \rightarrow \|j\rangle$ transition
b	Confocal parameter
c_j	Density of the molecule
$\vec{D}$	Displacement vector
d_{ijk}	Nonlinear coefficient
$\vec{E}$	Electric field
E	Energy of the molecular states
F_c	Coherence factor
f	Oscillator strength
g	Statistical weight of an atomic level
h	Plank's constant
$h(\mu, \xi)$	Focusing factor
I	Intensity
J	Total angular momentum
$\vec{k}$	Wave vector
k_B	Boltzman's constant
Δk	Momentum phase mismatch
L	Crystal length
L_c	Coherence length
l	Orbital angular momentum
n	Refractive index
$\vec{P}$	Macroscopic charge polarization
P	Output power
$P(r, \theta)$	Projection profile of the function $F(x, x)$
p	Pressure

$\vec{p}$	Dipole moment operator
$\vec{p}$	Linear momentum
$Q(T)$	Total partition function at a particular temperature
$S_{n,m}$	Absorption linestrength of $\|n\rangle \rightarrow \|m\rangle$ transition
$\vec{S}$	Poynting vector
T	Absolut temperature
U	Dielectric energy density
$V(\vec{r})$	Symmetrical and asymmetrical potential energy
v	Vibrational quantum number
$x(t)$	Deviation of the harmonic oscillator

Greek Symbols

α	Absorption coefficient
γ_{ij}	Broadening coefficient
γ	Total damping constant of an oscillator
$\Delta\bar{\nu}_C$	Lorentzian half width at half maximum (HWHM)
$\Delta\bar{\nu}_D$	Doppler half width at half maximum (HWHM)
δ	Optical phase difference for a round trip of light inside a Fabry-Perot cavity
ϵ	Permittivity
η	Conversion efficiency
θ	Polar angle
κ	Spring constant of the oscillation
Λ	Modulation period of the nonlinear crystal
λ	Wavelength
μ	Permeability
ν	Linear frequency
$\bar{\nu}$	Wavenumber
ρ	Density matrix
σ	Conductivity
$\tau(\bar{\nu})$	Absorbance
ϕ	Azimuthal angle
ϕ_C	Collisional Lineshape function
ϕ_D	Doppler Lineshape function
ϕ_V	Voigt Lineshape function
χ	Susceptibility
ψ	Wave function
ω	Angular frequency
$\Re\{F(x,y)\}$	Radon transform
Π	Electronic states

1 Introduction

Researches in the field of combustion have been intensified recently since an efficient combustion combined with low pollution is required. In order to obtain a deeper understanding of combustion processes it is necessary to perform studies of combustion parameters such as concentration and temperature distribution measurements. For this reason a wide area of spectroscopic monitoring techniques and devices have been developed and investigated in the recent years. Reviewing potential in-situ gas analysis techniques for improving combustion control, it is concluded that optical methods can provide the most reliable and active sensing of combustion systems. All the spectroscopic techniques can be divided into two general categories: *intrusive* and *nonintrusive* methods. The usefulness of intrusive methods is often limited because they introduce errors and disturbances to the flame measurements. Three examples of intrusive methods are

1. gas sampling and
2. nonlinear surface vibrational spectroscopy [1] such as
    - second-harmonic generation (SHG) and sum-frequency generation (SFG), and
3. semiconductor probes.

Gas sampling methods such as *wet chemical analysis* require high maintenance and frequent calibrations. Especially for the "sticky" gases like HCl, HF, and NH_3 sampling is accompanied with analytical errors since these gases are easily absorbed on surfaces and a large fraction can be lost during the sampling. SHG and SFG surface vibrational spectroscopy are high sensitive optical methods for the probing surfaces and are advantageous over conventional surface spectroscopic methods in which, for example, beams of charged particles are used as probe beam. However, their major drawback is that they require the insertion of a probe material into the combustion chamber [2] and therefore the setup parameters such as gas flow and local temperature can be influenced.

In contrast, purely nonintrusive optical methods such as laser spectroscopic techniques as there are

1. lasers-induced fluorescence (LIF) spectroscopy,
2. near-infrared (NIR) absorption spectroscopy, and
3. mid-infrared (MIR) absorption spectroscopy

have been developed as high sensitive and efficient techniques which allow nonintrusive measurements of multidimensional temperature and species distributions in combustion systems. They play an important role in the validation of the existing mathematical combustion models as well as in the development of active combustion control applications. However, all the combustion diagnostics requirements cannot be satisfied simultaneously by a single of those laser based spectroscopic methods. For example LIF suffers from quenching effects due to the inelastic interatomic collisions especially at high pressure levels. Photon excitation of light atoms is, however, not always possible since very high energetic photons are required to excite the atomic states. Furthermore, for absolute quantitative measurements, a calibration of the optical detection system is required (which can be done with the aid of Rayleigh scattering). Two-photon absorption LIF spectroscopy [3] circumvents these problems and the measurements of ppm-level concentrations of atmospheric molecules such as nitric oxide (NO) and carbon monoxide (CO) and of atoms such as oxygen (O) and hydrogen (H) is done by this newly emerged technique. However, the cross section of the two-photon excitation process is much lower than that of a single-photon process and thus the atomic levels cannot be excited efficiently.

Even though NIR laser sources (and detectors) are cheap and compatible with low-loss inexpensive optical fibers [4], NIR absorption spectroscopy can not be used due to the absence of strong absorption lines for the molecular species in the NIR spectral region [5]. In principle, the detection of such weak NIR molecular transition lines is possible but requires high sensitive detection techniques, for example wavelength modulation spectroscopy [6]. However, this makes the detection system very complex. Higher sensitivity in NIR absorption spectroscopy is also obtained by extending the path length using multipass cells (White cell and Herriot cell); a much higher sensitivity is obtained using cavity-ring down spectroscopy (CRDS) where the photon decay time (ring-down) in a high finess optical cavity is measured as the absorption sensitive observable [7]. In spite of high sensitivity and fast response of CRDS its application is still limited because of the need of high quality cavity mirror with a reflectivity which is designed to be high over a narrow spectral region (e. g. R = 99.95-99.98% in the MIR region). Furthermore, measurements of multiple species in different spectral regions can not be performed without mechanically changing the mirrors and due to the high reflectivity the output intensity can be in the order of 10% of the input intensity. Recently G. Engel et al. at Princeton University, have developed a prism-based CRDS to overcome the limitations of a mirror-based CRDS [8]. The wide spectral coverage of the prism allows the detection of multiple species without mechanical changes.

Laser absorption spectroscopy in the MIR spectral region is very interesting for combustion monitoring since nearly all molecules such as CO, water vapor (H_2O), NO, methane (CH_4), sulfur dioxide (SO_2), dinitro oxide (N_2O), and carbon dioxide (CO_2) exhibit strong fundamental absorption bands between 2 and 20 μm. The performance of spectroscopy in this region is advantageous in terms of high sensitivity and high selectivity. For MIR

high resolution absorption spectroscopy, laser sources with high spectral purity as well as continuous tunability are required. Some essential requirements of an ideal laser source for MIR absorption spectroscopy as well as approaches to meet them are composed in Figure 1.1.

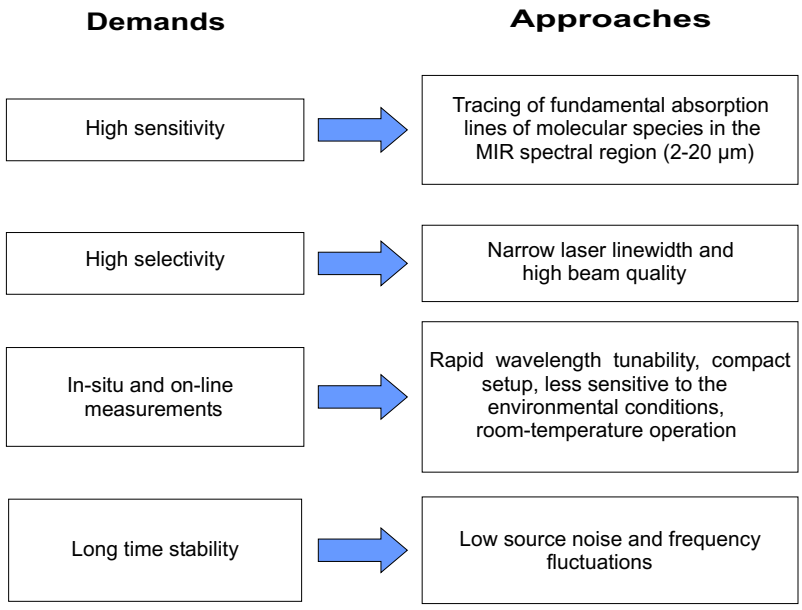

Figure 1.1: *The demands and approaches for an efficient laser source for spectroscopic applications in the MIR region.*

However, depending on the application, some of those requirements become more important and clearly all of those are not satisfied simultaneously. According to F. K. Tittel [9], MIR laser sources can be divided into two overall groups known as *class A* and *class B*. Class A MIR lasers are generated directly from a gain medium such as gas discharge, rare-earth materials, and semiconductors while class B MIR lasers sources are generated indirectly based on nonlinear conversion effects such as optical parametric down- and up-conversion and parametric oscillators. Each group of lasers is specified by its own special characteristics which enable different applications in specific operating regions.

From class A MIR laser sources

1. Lead-salt diode-lasers

2. Antimonide diode-lasers, and

3. Quantum Cascade (QC) lasers

are regarded as most important and practical. The common requirement for operation of those laser sources is the *cryogenic cooling*[1].

Lead-salt diode-lasers have been developed for the operation from 3 to 30 μm with a typical output power between P_{out} = 100-500 μW. These lasers can be tuned over a frequency range of $\bar{\nu}$ = 100 cm^{-1} when an appropriate operating temperature between T = 15-80 K is provided [10].

Contrary, the typical output power of an antimonide diode-laser is up to P_{out} = 20 mW but still it requires cryogenic cooling for reliable single-mode operation. Furthermore, some additional optical configurations such as an external cavity are required to reduce the linewidth of the laser [9].

A wide range of the MIR wavelengths from λ = 3.5 to 24 μm is covered by QC lasers. The QC lasers were invented at Bell Labs in 1994. Physically, QC lasers are based on the intersubband transitions in quantum wells and, therefore, unlike other semiconductor laser sources, their emitted wavelength is not determined by the band gap of the used material. In a conventional diode-laser, a photon is emitted when an electron combines with a hole, but in a QC laser a photon is emitted every time an electron moves from a higher to a lower energy level as it cascades down an energy staircase created by the applied voltage. Thus, the emission wavelength is determined by the thickness of the quantum well and barrier layers of the active region. Since only one type of charges (electrons) is needed for the operation of a QC laser, it is known as *unipolar semiconductor* laser. The linewidth of a typical cw QC laser is about a few MHz but reaches to about $\delta\bar{\nu}$ = 150 MHz when it is operated in pulsed regime [9]. These lasers also have the capability to generate a few hundreds of mW output power which is quite sufficient for spectroscopic applications. However, besides these excellent properties their tuning range is still limited and their beam divergence is large and astigmatic. A tunability of $\delta\lambda \sim 35$ cm^{-1} is obtained for a QC laser at a fixed temperature if an additional external cavity configuration is applied around the laser. A cw QC laser requires cryogenic cooling and rather high supply voltages. Therefore, the room-temperature operation is only feasible for pulsed QC lasers[2] operating in Fabry-Perot style. Most recently, QC lasing of P_{out} = 200 mW at T = 25°C is achieved for pulsed operation and of P_{out} = 10 mW at liquid-nitrogen temperature for cw operation at Bell Labs. Distributed feed back (DFB) QC laser have also been investigated for a reliable and stable single frequency operation for spectroscopic applications [11]. Quite recently, the operating wavelength of QC lasers has been extended to a new attractive region of the electromagnetic spectrum which ranges from a few hundred μm to a few millimeters. This special region and its associated research field is called as ***terahertz (THz)*** spectroscopy [12]. Taking into account all those limitations of class A lasers, this type of laser sources shows a considerable disadvantage compared

[1] For pulsed QC lasers there are some that can be operated at room temperature.
[2] Early QC lasers operated at temperatures lower than about T = 93 K.

to the lasers sources of class B. From class B lasers optical parametric oscillators (OPO) and difference-frequency generation (DFG) are of the most interesting sources in MIR spectral region.

In an OPO the nonlinear optical crystal is placed in a resonator and hence oscillation is possible either in a single resonant arrangement (SRO) or in a double resonant configuration (DRO). The OPO laser sources can be operated either in pulsed or in cw regime. Pulsed OPO lasers are commercially available while cw OPOs still have some practical shortcomings because the pump-power threshold and the damage threshold are in the same order of magnitude for the used optical nonlinear crystals. For pulsed OPO lasers the threshold oscillation can easily be achieved, but it is of course necessary to reach threshold before the pump pulse is turned off. Therefore, pump pulses with high peak power are needed. For the early cw OPO lasers DRO cavities were used because of their much lower threshold compared to SRO cavities. The first cw DRO-OPO laser was reported by Smith et al. in 1968 [13] and it was based on a $Ba_2NaNb_5O_{15}$ nonlinear crystal which was pumped by a frequency doubled Nd:YAG laser at $\lambda = 532$ nm. Typical output powers of OPOs lie in the milliwatt range. The generated OPO laser wavelength depends on the nonlinear crystal; typical nonlinear optical crystals are KTP, LBO, PPKTP, and $LiNbO_3$. As reviewed by M. Ebrahimzadeh and M. H. Dunn [14] the OPO wavelengths generated by those nonlinear crystals are limited to about $\lambda = 4$ μm and therefore, can not be used for the spectral region centered around $\lambda = 5$ μm where the strong absorption lines of NO molecules are present. Recently, quasi-phase matching (QPM) in periodically poled $LiNbO_3$ (PPLN) offers several advantages over cw OPOs such as a high effective nonlinear coefficient in the wavelength region of $\lambda \leq 4\mu$m. However, the setup of an OPO is very complicated since it needs an external resonator which makes wavelength tuning more difficult.

In contrast a DFG laser using two laser beams as pump and signal sources at different frequencies overcomes the limitation of the laser sources presented above. It is an important source in the MIR region in terms of narrow linewidth ($\delta\bar{\nu} = 0.01$ cm^{-1} at FWHM) and wide tunability (more than $\delta\lambda = 6$ μm in an $AgGaS_2$ nonlinear optical crystal). The narrow linewidth of the generated idler wave is associated with the pump and signal linewidths and is a unique property of a DFG laser which makes it a very attractive alternative to other laser sources. Furthermore, the DFG-based laser source has a superior output beam quality compared to conventional diode-lasers. This output beam can be used for absorption spectroscopic measurements with only one simple optical focusing element. As reported by Richter et al. [15] for the first time, the cross section of the measured DFG beam is uniform, circular, and fits to a Gaussian intensity profile to better than 95%, and the minimum laser beam width is measured to be $d = 1.5$ mm. They mixed an Yb-fiber amplifier and a fiber laser in PPLN to generate $P_{out} = 0.75$ mW MIR radiation at $\lambda = 3.53$ μm. The laser sources based on difference-frequency generation in both $AgGaS_2$ and PPLN nonlinear crystals have recently been used for

multi-component trace gas analysis. However, low power and/or discontinuous tunable diode-laser sources used in the DFG process reduce the MIR DFG output power and limit its radiation to some specific wavelengths. The output power of the DFG radiation can be enhanced to hundreds of μW using diode-laser sources in combination with fiber amplifiers and a nonlinear crystal with high nonlinearity, e. g. PPLN [16]. However, the laser wavelength generated in systems based on PPLN is limited to about 4 μm due to the transparency range of the material. In this thesis, the application of a novel cw MIR DFG laser in $AgGaS_2$ for combustion diagnostics and industrial process control is presented. The performance of the MIR DFG laser is finally shown determining CO concentration in the atmosphere of an industrial gas fired glass melting furnace at Dr. Genthe GmbH&Co. KG, Germany.

In chapter 2 and 3 the theoretical principles of nonlinear optics and the qualitative and quantitative DFG down-conversion are considered, respectively. Chapter 4 discusses the basics of molecular laser absorption spectroscopy in the MIR region in brief. The efficiency of the MIR DFG laser is demonstrated in chapter 5 by measuring the broadening coefficients of CO and performing CO-concentration measurements in the flame of a methane/air fired McKenna flat flame burner. In chapter 6 two relatively mature technologies, MIR DFG laser absorption spectroscopy and computerized tomographic (CT) reconstruction, are combined to obtain a very valuable diagnostic tool for environmental monitoring as well as combustion diagnostics. In this chapter, to our knowledge for the first time, the imaging of the CO concentration distribution in the flame of the McKenna burner is performed using 3-dimensional tomographic reconstruction and MIR DFG laser radiation. Chapter 7 presents the modified MIR DFG system in order to obtain a wide tuning range over 71.5 cm^{-1} for simultaneous measurements of CO and NO molecules at room temperature. This modification is obtained by constructing an external short-cavity around the pump diode-laser. Finally in chapter 8 the features of the MIR DFG laser are demonstrated as an efficient CO-sensor for in-situ and on-line monitoring of combustion species in industrial applications.

2 Nonlinear optics in brief

Many physical phenomena follow a linear law if the perturbance on the system is small. When it exceeds a certain limit, the linear description of the physical system is no longer valid. If electromagnetic radiation propagates through a medium, it will induce a motion of the charged particles of the material. The contribution from the magnetic field part of that electromagnetic radiation and from electric quadrupoles are much weaker than the electric dipoles and are usually neglected. The optical disturbing electric field contribution, $\vec{E}$, is capable to redistribute the outermost loosely bound electrons of the medium in the direction of the applied electric field. The medium is then polarized, resulting in an induced electric oscillating dipole moment, $\vec{p}$. In a dielectric medium charges are bound together and will start to oscillate in the applied electric field. This is called the **electric-dipole approximation** [17]. The oscillating dipoles add up to a macroscopic charge polarization, $\vec{P}$ (defined as the sum of the microscopic electrical dipole moments in the media per unit volume) depending on the magnitude of the applied electric field. For low field intensities, the charges can follow the field almost exactly and the relationship between $\vec{E}$ and $\vec{P}$ is essentially linear. This linearity can be shown as

$$\vec{P} = \epsilon_0 \chi^{(1)} \vec{E}, \tag{2.1}$$

where ϵ_0 is the dielectric constant of free space and $\chi^{(1)}$ [m volt^{-1}], is the linear field-independent optical susceptibility constant of the medium, which is a scalar quantity and responsible for linear optical properties of the medium such as reflection, refraction, dispersion, absorption, and birefringence. In the limit of intense optical fields, the optical susceptibility and the corresponding dielectric constant of the medium can become functions of the electric field. If a medium is irradiated by a laser with an intense electric field of 10^6 to 10^7 volts cm^{-1}, the field strength is in the order of the atomic field strength and too large to allow the relationship between $\vec{E}$ and $\vec{P}$ to be treated as linear. Under this special condition, the optical susceptibility and the corresponding dielectric constant can be expanded in a Taylor series as

$$\chi(\vec{E}) = \chi^{(1)} + \chi^{(2)} \cdot \vec{E} + \chi^{(3)} : \vec{E}\vec{E} + \cdots \tag{2.2}$$

or

$$\epsilon(\vec{E}) = \epsilon^{(1)} + \epsilon^{(2)} \cdot \vec{E} + \epsilon^{(3)} : \vec{E}\vec{E} + \cdots$$

where $\epsilon^{(1)} = \epsilon_0(1 + \chi^{(1)})$ and $\epsilon^{(i)} = \epsilon_0 \chi^{(i)}$ for $i \geq 2$. Therefore, the induced macroscopic polarization in the medium contains terms that depend nonlinearly on the field as

$$\begin{aligned} \vec{P} &= \epsilon_0 \left[\chi^{(1)} \cdot \vec{E} + \chi^{(2)} : \vec{E}\vec{E} + \chi^{(3)} \vdots \vec{E}\vec{E}\vec{E} + \cdots \right] \\ &= \vec{P}^{(1)} + \vec{P}^{(2)} + \vec{P}^{(3)} + \cdots \end{aligned} \tag{2.3}$$

In general, $\vec{P}$ and $\vec{E}$ are not parallel in the most crystalline media, and they are related by the tensor notation as it is written in Equation (2.3). $\chi^{(i)}$ is the susceptibility tensor of rank (i+1) of the medium with the relative magnitudes of $\chi^{(1)} : \chi^{(2)} : \chi^{(3)} \simeq 1 : 10^{-8} : 10^{-16}$ [14]. Therefore, as the field intensity increases, the nonlinear polarization terms $\vec{P}^{(i\geq 2)}$ become more pronounced and will lead to a large variety of nonlinear optical effects. However, the most widely studied of these nonlinear effects are, of course, those associated with the lower-order terms in Equation (2.3). The second-order nonlinear susceptibility $\chi^{(2)}$ gives rise to nonlinear optical processes such as the linear electro-optic (Pockels) effect, the optical parametric generation (OPG) and amplification (OPA), second-harmonic generation (SHG), and difference-frequency generation (DFG). Examples of the third-order nonlinearity effects due to the $\chi^{(3)}$ term are third-harmonic generation, two photon absorption, self-focusing, four-wave mixing, phase conjugation, the optical Kerr effect, and stimulated Raman, Brillouin, and Rayleigh scattering. There is also a large variety of dynamic nonlinear optical effects such as photon echo, optical Rabi effect, self-induced transparency and picosecond and femtosecond quantum beats. In addition to the nonlinear optical processes involving only photons that are related to the nonlinear dependence on the electrical field, the medium can become nonlinear indirectly through other types of excitations, e. g., by molecular vibrations, or acoustic and plasma waves.

2.1 Optical linearity and nonlinearity

2.1.1 The origin of optical linearity

The linear optical properties of a medium such as absorption and dispersion can be understood as a result of classical harmonic motion of the electrons in a combined field of the atom and the coulombian force due to the applied external field. This resultant force is described in terms of damped harmonic oscillators. The response of these oscillators to the resultant force is identified by a symmetrical potential energy, $V(\vec{r})$. A symmetrical potential energy must reflect the crystal symmetry. By this assumption, in the harmonic oscillator potential expansion only even powers of $\vec{r}$ are kept as

$$V(\vec{r}) = \frac{1}{2} m\omega_0 \vec{r}^{\,2} + \frac{1}{4} m\beta \vec{r}^{\,4} + \cdots \tag{2.4}$$

where ω_0 is the angular resonant frequency of the electronic oscillators, β is a constant, and m is the electron mass. In the linear approximation in which the linear polarization is proportional to the electric field, the driven force is therefore accounted for by the first term in the Equation (2.4). This simple description of the medium is known as Lorentz model. In this model the medium is represented by a collection of identical independent harmonic oscillators which are characterized by five parameters; a spring constant κ, a total damping constant γ , a mass m, a charge e, and a dimensionless oscillator strength f. Undoubtedly, the latter is the most important quantity which can be used to represent the fraction of the atomic oscillators effective for each resonant frequency. Specifically, in the

case of absorption, the f value can be related to the so called absorption coefficient via the linear susceptibility of the medium through treating the one-dimensional (for simplicity) equation of motion for a damped oscillator as [18]

$$\left[\frac{\partial^2}{\partial t^2} + \gamma\frac{\partial}{\partial t} + \omega_0^2\right] x^{(1)}(t) = -\frac{e\sqrt{f}}{2m}E(t), \tag{2.5}$$

where $x^{(1)}(t)$ is the deviation of the harmonic oscillator from its equilibrium position in the absence of the monochromatic driven field $E(t) = \frac{1}{2}[E(\omega_0)e^{-i\omega_n t} + c.c.]$. Substituting $E(t)$ into the Equation (2.5) and knowing $P^{(1)}(t) = Nex^{(1)}(t)$ leads to a straightforward expression for the linear polarization as

$$P^{(1)}(\omega_n) = \frac{Ne^2 f}{m[(\omega_0^2 - \omega_n^2) + i\omega_n\gamma]}E(\omega_n) + c.c. \tag{2.6}$$

for N oscillators in the volume. Comparing the last expression with the Equation (2.1) gives the corresponding real and imaginary parts of the linear complex susceptibility $\chi^{(1)}(\omega_n)$ as

$$\chi^{(1)}(\omega_n) = \frac{Ne^2 f}{m\epsilon_0}\cdot\frac{1}{(\omega_0^2 - \omega_n^2) + i\omega_n\gamma}. \tag{2.7}$$

The imaginary part of the susceptibility is responsible for the absorption properties of the medium. For a real medium, the results must be summed over all the effective oscillators which are close to the resonance frequency ($\omega_n \approx \omega_0$). Then

$$Im\chi^{(1)}(\omega_n) = \sum_j \frac{N_j e^2 f_j}{m\epsilon_0\omega_{0j}}\cdot\frac{\gamma_j}{(\omega_{0j} - \omega_n)^2 + \gamma_j^2} \tag{2.8}$$

for all effective oscillators in the medium leads to an expression for the absorption coefficient, $\alpha(\omega_n)$ as

$$\alpha(\omega_n) = \sum_j \frac{N_j e^2 f_j}{2m\epsilon_0 c}\cdot\frac{\gamma_j/2}{(\omega_{0j} - \omega_n)^2 + (\gamma_j/2)^2} \tag{2.9}$$

which can be used for any absorbing medium containing gases or vapors. c is the speed of light. These results show that the absorption lineshape near the resonance frequency[1] is a *Lorentzian* function with a linewidth of γ_j as shown in the Figure 2.1.
The f value can be used to specify the transition probability. It is approximately unity for a strong resonance transition. Since in such linear medium the induced polarization is, at any moment, proportional to the applied field, $\vec{P}$ oscillates near $\omega_n \approx \omega_0$. Integrating over the absorption line gives [19]

$$\int_{line}\alpha(\omega)d\omega = \frac{N_j\pi e^2}{2m\epsilon_0 c}f_{j\to k}, \tag{2.10}$$

[1]This absorption occurs if a transition between atomic or molecular states takes place.

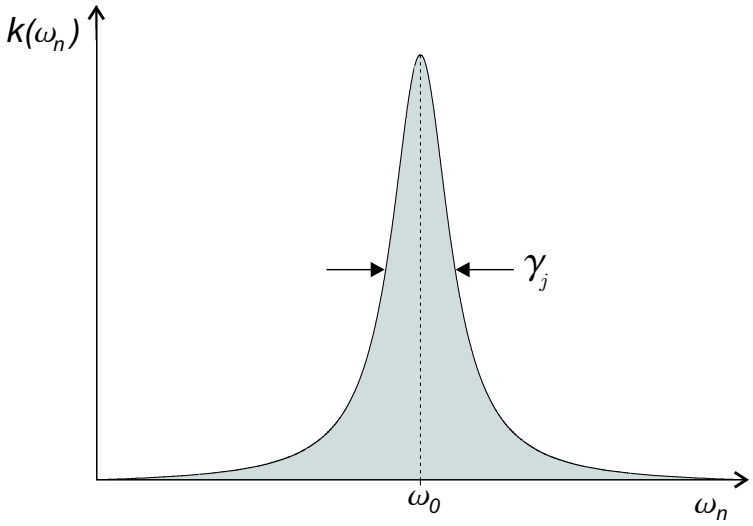

Figure 2.1: *Absorption coefficient $k(\omega_n)$ as a function of angular frequency for a medium containing j classical oscillators at resonance frequency ω_0 and damping constant Γ_j.*

which is assumed $\omega_0 \gg \gamma$ for the $j \rightarrow k$ transition. The last equation can be used to relate the well-known Einstein coefficient B_{jk} to the f value by

$$f_{jk} = \frac{m\epsilon_0 h}{\pi^2 e^2}\omega_{jk}B_{jk}. \tag{2.11}$$

h is Planck's constant and f_{jk} implies the absorption line strength of the $j \rightarrow k$ transition. As a consequence absorption phenomena in a linear gaseous media can be used occasionally to determine B_{jk}. The emission linestrength f_{kj} can be related to the absorption linestrenght by

$$f_{kj} = -\frac{g_j}{g_k}f_{jk} \tag{2.12}$$

where g is the statistical weight of the corresponding atomic level. The oscillator strength can also be represented by the gf values so that they can be applied either to emission or to absorption.

2.1.2 The origin of optical nonlinearity

An extension of Equation (2.5) with the inclusion of suitable anharmonicities in the oscillator serves as a useful starting point in understanding the microscopic origin of the optical nonlinearity. In this case the spring constant of the oscillator representing the medium is no longer linear and the motion of the electron is large enough so that the Taylor expansion has significant terms of quadratic or higher orders. This is true for nearly all crystalline

media. Consequently, the potential energy of the oscillator is not only a quadratic function of the deviation from the equilibrium position but it contains odd powers of the position as well:

$$V(\vec{r}) = \frac{1}{2}m\omega_0\vec{r}^{\,2} + \frac{1}{3}m\zeta\vec{r}^{\,3} + \cdots, \tag{2.13}$$

where ζ is a constant, which reflects the asymmetry response of the potential energy of the oscillator to a harmonic field. Clearly, the larger the anharmonicity corresponding to larger asymmetry in the oscillator potential energy is, the larger is the nonlinear contribution of the susceptibility $\chi^{(2)}$ in the response. To relate this nonlinearity to the applied electric field, the $\zeta\vec{r}^{\,3}$ term has to be added to the one-dimensional Equation (2.6) to give

$$\frac{\partial^2}{\partial t^2}x(t) + \gamma\frac{\partial}{\partial t}x(t) + \omega_0^2 x(t) + \zeta x^2(t) = -\frac{e\sqrt{f}}{2m}[E(\omega_n)e^{i\omega_n t} + c.c.], \tag{2.14}$$

which is complicated to solve. The solution to the above nonlinear equation can be obtained by the use of perturbation techniques, assuming that the anharmonic term is small compared to the harmonic one. This assumption involves neglecting the nonlinear term in the potential energy expansion by setting its coefficient equal to zero, $\zeta = 0$. The resulting equation of motion is called the *zero-order approximation*. Inserting the zero-order solution into Equation (2.14) gives the first- and the second-order approximation solutions. The displacement $x(t)$ can be expanded according to the powers of the $\vec{E}$-field as

$$x(t) = x^{(1)}(t) + x^{(2)}(t) + \cdots, \tag{2.15}$$

where $x^{(1)}(t)$ and $x^{(2)}(t)$ are the harmonic and anharmonic deviations of oscillators from their equilibrium position and are proportional to the first and second powers of the electric field, respectively. Inserting the last expression into Equation (2.14) and equating the coefficients of nth power of the electric field on both sides of the equation gives

$$\left[\frac{\partial^2}{\partial t^2} + \gamma\frac{\partial}{\partial t} + \omega_0^2\right] x^{(2)}(t) = \zeta\left[x^{(1)}(t)\right]^2. \tag{2.16}$$

The same mathematics as applied to the first-order deviation $x^{(1)}(t)$ can be used here to calculate the second-order deviation $x^{(2)}(t)$ since it is proportional to $[x^{(1)}(t)]^2$ and hence to $\vec{E}^2$. It is desirable to consider a bichromatic form for the applied optical field as $E(t) = \frac{1}{2}[E(\omega_n)e^{-i\omega_n} + E(\omega_m)e^{-i\omega_m} + c.c.]$ to specify the frequency mixing aspects of the nonlinear media. The linear response $[x^{(1)}(t)]^2$ is contained in the terms which are oscillating at frequency $\omega_n \pm \omega_m$ as well as in dc components.

In the case of a monochromatic driven field, there is only one applied optical frequency and therefore the possible combinations are $\omega_n \pm \omega_n$, which results in the second-harmonic oscillation at frequency $2\omega_n$ and the optical rectification or dc component oscillating at zero frequency. In the case of second-harmonic generation (SHG), a part of energy of the optical wave at frequency ω_n is converted to that of a wave at frequency $2\omega_n$. Historically, SHG was the first nonlinear generation when *Franken* et. al. in 1961 generated the second

harmonic ($\lambda = 347$ nm) of a ruby laser beam ($\lambda = 694$ nm) which was focused on a quartz crystal. Optical rectification can also be viewed as a special case of difference-frequency generation (DFG) due to a bichromatic optical field oscillating at zero difference frequency. An example of optical rectification is the Pockels effect. Taking the difference-frequency component in the expansion of $[x^{(1)}(t)]^2$ yields

$$\left[x^{(1)}(t)\right]^2 = \frac{e^2 f}{2m^2} \cdot \frac{E(\omega_n)E^*(\omega_m)}{(\omega_0^2 - \omega_n^2 + i\gamma\omega_n)((\omega_0^2 - \omega_m^2 + i\gamma\omega_m)}. \tag{2.17}$$

Therefore the final expression for $x^{(2)}(t)$ can be written by inserting Equation (2.17) into Equation (2.16) for a number of discrete frequencies as

$$x^{(2)}(t)|_{\omega=\omega_n-\omega_m} = \frac{\zeta e^2 f}{2m^2} \sum_n \sum_m \frac{E(\omega_n)E^*(\omega_m)}{(\omega_0^2 - \omega_n^2 + i\gamma\omega_n)(\omega_0^2 - \omega_m^2 + i\gamma\omega_m)} \cdot \frac{1}{[\omega_0^2 - (\omega_n - \omega_m)^2 - i\gamma(\omega_n - \omega_m)]}. \tag{2.18}$$

Since the second-order polarization $\vec{P}^{(2)}(t)$ is related to the second-order deviation $x^{(2)}(t)$ by $\vec{P}^{(2)}(t) = Nex^{(2)}(t)$, the second-order nonlinearity $\chi^{(2)}(t)$ is

$$\chi^{(2)}(\omega_n, \omega_m) = \frac{\zeta e^3 f}{2\epsilon_0 m^2} \sum_n \sum_m \frac{1}{(\omega_0^2 - \omega_n^2 + i\gamma\omega_n)(\omega_0^2 - \omega_m^2 + i\gamma\omega_m)[\omega_0^2 - (\omega_n - \omega_m)^2 - i\gamma(\omega_n - \omega_m)]} \tag{2.19}$$

and

$$\vec{P}^{(2)}(\omega_n, \omega_m) = \epsilon_0 \sum_n \sum_m \chi^{(2)}(\omega_n, \omega_m)E(\omega_n)E^*(\omega_m).$$

Both the nonlinear susceptibility and the corresponding polarization are proportional to either oscillator strength f and the asymmetry constant ζ. Therefore, a larger anharmonicity results in a larger f value and hence a larger nonlinearity. This is the key for the generation of the difference-frequency radiation through a nonlinear medium and hence crystalline media with a high asymmetrical response are of great interest in this regard. $\vec{P}^{(2)}(\omega = \omega_n - \omega_m)$ can be generalized by summing over all possible frequencies as

$$\vec{P}^{(2)}(\omega) = \epsilon_0 \int_{-\infty}^{\infty} d\omega_n \int_{-\infty}^{\infty} d\omega_m \chi^{(2)}(\omega_n, \omega_m)E(\omega_n)E^*(\omega_m)\delta[\omega - (\omega_n - \omega_m)]. \tag{2.20}$$

The δ-function ensures that the induced polarization reaches its maximum only if ω is equal to the difference frequency $\omega_n - \omega_m$. Equation (2.19) can be stated in terms of the first-order susceptibility as

$$\chi^{(2)}(\omega_n, \omega_m) = -\frac{\zeta m}{2N^2 e^3 \sqrt{f}} \chi^{(1)}(\omega_n)\chi^{(1)}(\omega_m)\chi^{(1)}(\omega_n, \omega_m) \tag{2.21}$$

to introduce the so-called *Miller's coefficient* as

$$\delta = \frac{\chi^{(2)}(\omega_n, \omega_m)}{\chi^{(1)}(\omega_n)\chi^{(1)}(\omega_m)\chi^{(1)}(\omega_n, \omega_m)\epsilon_0^2} = -\frac{\zeta m}{2\epsilon_0^2 N^2 e^3 \sqrt{f}} \tag{2.22}$$

which was first suggested by R. C. Miller. Miller assumed that δ is approximately a constant for all materials, and its magnitude was found to be in the order of 2-3$\times 10^6$ [esu]. Therefore, to find materials with large nonlinearity, one simply should look for materials with large values of $\chi^{(1)}(\omega_n)$, $\chi^{(1)}(\omega_m)$, and $\chi^{(1)}(\omega_n, \omega_m)$. Therefore, the magnitude of the nonlinearity for many classes of nonlinear optical materials can be estimated using Miller's coefficient. This rule is known as Miller's rule. However, many classes of materials such as organic crystals do not fit into this rule. However, in the Equation (2.19) ω_0 represents an eigenmode which corresponds to an eigenstate of the medium and hence it is desirable to treat the problem of the nonlinearity quantum mechanically.

2.2 Quantum behavior of the nonlinear susceptibility and energy diagram

From the quantum mechanics point of view the nonlinear optical susceptibility originates from the higher order terms in the perturbation solutions of the appropriate Schrödinger equation. In this method the properties of a system including N identical particles (atoms, molecules, etc.) can be described as a solution of the time-dependent Hamilton operator including an interaction term between the applied electric field $\vec{E}(\vec{r}, t)$ and the system which is characterized by the dipole moment operator $\vec{p}$ induced by the electric field as $H' = -\vec{E}(\vec{r}, t) \cdot \vec{p}$. The main task of the quantum mechanics is to determine an appropriate wave function, $|\psi\rangle$, which contains the maximum available information about the physical system. This can be done either by use of the

- density matrix representation, or
- the time-dependent Schrödinger equation.

The solution of the density matrix ρ to the nonlinear susceptibility and hence to the nonlinear polarization can be obtained by using the formal property of ρ as

$$\vec{P} = \langle \vec{p} \rangle = NTr\rho\vec{p} \tag{2.23}$$

where $\vec{P}$ is the polarization of the medium. It is suitable to consider the ρ in the so-called *interaction* representation[2] where the equation of motion is written as

$$i\hbar \frac{\partial}{\partial t} = [V_I(t), \rho_I(t)], \tag{2.24}$$

where $V_I(t) = -\vec{E}(\vec{r}, t) \cdot \vec{p}$ is the potential function in the interaction picture. Therefore, the terminology of the equation of motion can be pictured as

[2] In this representation the time dependence is divided between the operators and states.

{A change of the density operator in time} $\Leftrightarrow$ {A change of density of states in system}.

In this picture the density operator can be expanded as

$$\rho_I(t) = \underbrace{\rho_I^{(0)}(t)}_{\sim|E(t)|^0} + \underbrace{\rho_I^{(1)}(t)}_{\sim|E(t)|^1} + \underbrace{\rho_I^{(2)}(t)}_{\sim|E(t)|^2} + \cdots + \underbrace{\rho_I^{(n)}(t)}_{\sim|E(t)|^n} + \cdots, \tag{2.25}$$

where the zeroth order term, $\rho_I^{(0)}(t)$, which is independent of the applied electric field, is given by the Boltzman distribution at thermal equilibrium. Taking the third term in Equation (2.25) leads to a final expression for the second-order nonlinearity $\chi_{ijk}^{(2)}$ as [20]

$$\chi_{ijk}^{(2)}(\omega_n, \omega_m) = -\frac{N}{\epsilon_0 \hbar^2} \int_{-\infty}^{0} dt' \int_{-\infty}^{0} dt'' Tr\left\{\rho_I(t_0)\left[[p_i, p_{Ij}(t')], p_{Ik}(t'')\right]\right\} e^{-i(\omega_n t' + \omega_m t'')} \tag{2.26}$$

when the Equation (2.23) is followed. Therefore the second-order susceptibility $\chi_{ijk}^{(2)}$ is a tensor of rank 3 and its tensor elements and their magnitudes are associated with the process involving the interaction of the nonlinear medium and two incident light beams at ω_n and ω_m.

In the Schrödinger representation the equation of motion can be written on the base of the time-dependent *probability amplitudes* $a_m^{(l)}$ which determine the probability of the system to be found in the eigenstate when it is perturbed. Therefore, the equation of motion for a multi-level system is

$$\begin{aligned} \frac{\partial}{\partial t} a_m^{(l)} &= -\frac{i}{\hbar} \sum_p a_p^{(l-1)}(t) \langle u_m | \xi V(t) | u_p \rangle e^{i\omega_{mp} t} \\ &= \underbrace{\frac{\partial}{\partial t} a_m^{(0)}}_{\sim|\xi|^0} + \underbrace{\frac{\partial}{\partial t} a_m^{(1)}}_{\sim|\xi|^1} + \underbrace{\frac{\partial}{\partial t} a_m^{(2)}}_{\sim|\xi|^2} + \cdots + \underbrace{\frac{\partial}{\partial t} a_m^{(n)}}_{\sim|\xi|^n} + \cdots, \end{aligned} \tag{2.27}$$

where ω_{mp} is the transition frequency between states $|m\rangle$ and $|p\rangle$ and ξ is a continuously varying parameter which determines the maximum perturbation ($\xi = 1$) applied to the system. Taking the third term in the Equation (2.27) again leads to an expression for the second-order susceptibility $\chi_{ijk}^{(2)}$ if the corresponding wavefunctions are used in the following expansion for $\vec{P}^{(2)}$ as

$$\langle \vec{P}^{(2)} \rangle = \underbrace{\langle \psi^{(0)} | \vec{p} | \psi^{(2)} \rangle + \langle \psi^{(1)} | \vec{p} | \psi^{(1)} \rangle + \langle \psi^{(2)} | \vec{p} | \psi^{(0)} \rangle}_{\sim|\xi|^2}. \tag{2.28}$$

Finally, the second-order susceptibility can be written as

$$\chi^{(2)}_{ijk}(\omega_q \pm \omega_l, \omega_q, \omega_l) = \frac{N}{\epsilon_0 \hbar^2} \Im_I \sum_n \sum_m \{ \frac{p^i_{gn} p^j_{nm} p^k_{mg}}{[\omega_{ng} - (\omega_q \pm \omega_l)](\omega_{mg} - \omega_q)} + \frac{p^j_{gn} p^i_{nm} p^k_{mg}}{(\omega^*_{ng} \pm \omega_l)(\omega_{mg} + \omega_q \pm \omega_l)} + \frac{p^j_{gn} p^i_{nm} p^k_{mg}}{(\omega^*_{ng} \pm \omega_l)(\omega_{mg} - \omega_q)} \} \tag{2.29}$$

where the $\Im_I$ is known as intrinsic permutation operator. More details can be found in [21]. The different terms in the Equation (2.29) are distinguished by the photon creation and annihilation processes. Far off resonance two photons with energies $\hbar\omega_q$ and $\hbar\omega_l$ are annihilated and a new photon at sum frequency $\hbar(\omega_q + \omega_l)$ is created while the material system remains in the initial system. In the DFG process a photon at $\hbar\omega_q$ is annihilated and two new photons at $\hbar\omega_l$ and $\hbar(\omega_q - \omega_l)$ are created. The energy diagrams of the SFG and DFG processes are depicted in Figure 2.2.

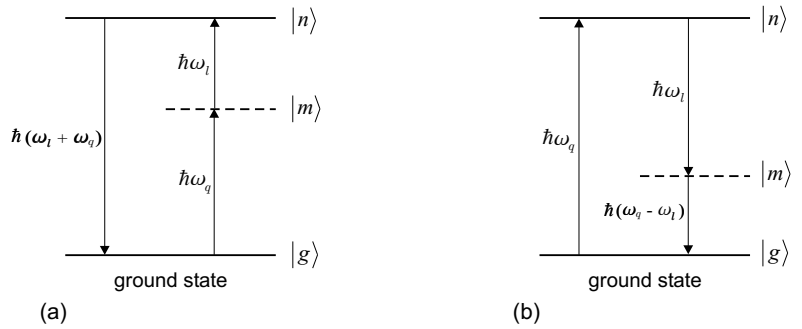

Figure 2.2: *The energy diagram of (a) SFG and (b) DFG processes.*

Therefore, the nonlinearity $\chi^{(2)}_{ijk}$ describes the coupling between three electromagnetic waves. Each of those is characterized by a complex amplitude E, angular frequency ω, wave vector $\vec{k}$, and polarization direction.

2.3 The nonlinear susceptibility tensor

In most crystalline media where inversion symmetry is not present, or in the case of birefringence, $\vec{P}$ and $\vec{E}$ can be treated by tensor representation through the nonlinear susceptibility tensor, $\chi^{(2)}_{ijk}(\omega_n, \omega_m)$. In general, it is a third-rank tensor with 27 independent coefficients. However, in practice many of these components vanish under certain symmetry conditions, so that the total number of independent components is generally smaller. In media that lack inversion symmetry the $\chi^{(2)}_{ijk}(\omega_n, \omega_m)$ tensor is nonzero and a number of symmetry arguments can be involved to reduce the number of nonzero terms of the tensor. These symmetry arguments can be classified into four categories as

1. intrinsic permutation symmetry,

2. reality condition,

3. overall permutation symmetry, and

4. causality.

Intrinsic permutation symmetry. Because of the fact that in Equation (2.20) the electric field component product commutates the frequencies can be permuted with the coordinates for the above equality to hold,

$$\chi^{(2)}_{ijk}(\omega_n, \omega_m) = \chi^{(2)}_{ikj}(\omega_m, \omega_n)$$

for all combination of i, j, k. This property where the direction indices and frequency arguments can be permuted [e. g. $(j, \omega_n) \Leftrightarrow (k, \omega_m)$] is called *intrinsic permutation*. Taking into account the intrinsic permutation symmetry condition, the number of the independent coefficients of the tensor reduces to 18.

Reality condition. The electric field and the induced macroscopic polarization density of the medium are the physical quantities and hence must be real. The requirements for the optical susceptibility is then

$$\chi^{(2)}_{ijk}(-\omega_n, -\omega_m) = [\chi^{(2)}_{ijk}(\omega_n, \omega_m)]^*$$

which is known as the *reality condition*.

Overall permutation symmetry. If the nonlinear polarization is only due to the electronic motion and there are no absorption resonances in the spectral region containing ω_n, ω_m, and $\omega_n - \omega_m$, then the dispersion of the nonlinearity is negligible and all frequencies act in an equivalent manner. Under this condition, nondispersive media, in addition to the intrinsic permutation symmetry, show also an overall permutation symmetry where the combination $(i, -\omega_n, -\omega_m)$ is included in the sets which can be permuted leaving the nonlinear susceptibility invariant, which means all elements of the nonlinear optical coefficient tensor formed by permuting i, j, and k, are equal. So

$$\chi^{(2)}_{ijk}(\omega_n, \omega_m) \cong \chi^{(2)}_{ikj}(\omega_n, \omega_m)$$

Obviously, the overall permutation symmetry is just an approximation, but it is valid in the most cases of interest. Furthermore, when the nonlinear polarization is of electronic, rather than ionic origin and the crystal is transparent throughout a region that includes all the frequencies involved in the nonlinear process, the polarization is a single-valued function of the electric field, if the frequencies of the mixing fields are well below the electronic absorption region. The mathematical statement of the above condition my be written as [22]

$$\oint_c d(\vec{P} \cdot \vec{E}) = 0 \tag{2.30}$$

where c is any arbitrary closed path in the $\vec{E}$ space. In a medium where the frequency of the macroscopic polarization density is far from the resonance frequency, the applied electric radiation is no longer absorbed and hence that medium is lossless. The last expression is the characteristics of any lossless medium and can be written as

$$-\oint_c \vec{P} \cdot d\vec{E} = \oint_c \vec{E} \cdot d\vec{P}. \tag{2.31}$$

The right-hand side of the above equation is the work done on the macroscopic polarization by the applied electric field. It is equal to zero for a lossless medium, and thus the medium can be characterized by a potential function. Combining this characteristic with the overall permutation symmetry means that the nonlinear susceptibility is invariant under permutations of the direction indices. This gives

$$\chi^{(2)}_{ijk}(\omega_n, \omega_m) \cong \chi^{(2)}_{jik}(\omega_n, \omega_m)$$

which is known as *Kleinman* symmetry that applies in the low frequency limit, far from any material resonance.

Causality. The causality means that any feature in the applied electric field cannot affect the output polarization at earlier time. As an example, if the Fourier transformation is applied to write the first-order optical polarization in the time domain, then

$$P^{(1)}_i(t) = \frac{\epsilon_0}{2\pi} \sum_j \int_{-\infty}^{\infty} \chi^{(1)}_{ij}(\tau) E(t-\tau) d\tau$$

which means that the convolution $E(t-\tau)$ cannot influence $P(t)$ if $t < t-\tau$ that is $\tau < 0$. This requires $\chi^{(1)}_{ij} = 0$ for $\tau < 0$.

The $\chi^{(2)}_{ijk}(\omega_n, \omega_m)$ is the quantity calculated by theoreticians. However, the experimentalists measure the nonlinear coefficient denoted by $d_{ijk}(\omega_n, \omega_m)$. It can be defined as

$$d_{ijk}(\omega_n, \omega_m) = \frac{1}{2} \chi^{(2)}_{ijk}(\omega_n, \omega_m). \tag{2.32}$$

From the intrinsic permutation symmetry and if the electric field has components along the y and the z axes, there will be a polarization generated parallel to the x axis and therefore, the $d_{i(jk)}(\omega)$ tensor can be written in the form of d_{lm}. The index l can be varied from 1 to 3 while the m index varies from 1 to 6, so that

(jk)				32	31	21
	11	22	33	23	13	12
m	1	2	3	4	5	6

which is called as Voigt notation. By using this representation, the coefficients can be expressed as the elements of a 3×6 matrix rather than a 3×3×3 tensor, which is called the d-matrix. The electric field products can also be written in the $(EE)_m$ form including the following components

$$\begin{aligned}(EE)_1 &= E_1^2 \qquad (EE)_2 = E_2^2 \qquad (EE)_3 = E_3^2 \\ (EE)_4 &= 2E_2E_3 \quad (EE)_5 = 2E_1E_3 \quad (EE)_6 = 2E_1E_2\end{aligned} \tag{2.33}$$

The d-matrix independent coefficients can be reduced if both the Kleinman symmetry and the group theory are included. The typical symmetry properties of a medium also may further reduce the number of those coefficients. As an example, in the case of the point group symmetry $\bar{4}2m$, the total number of the independent elements of the d-matrix reduces to three and the induced polarization density components are then written as

$$P_x = 2\epsilon_0 d_{14} E_y E_z \qquad P_y = 2\epsilon_0 d_{14} E_z E_x \qquad P_z = 2\epsilon_0 d_{36} E_x E_y. \tag{2.34}$$

Again Kleinman symmetry requires that the number of two independent coefficients reduces to one, since $d_{14} = d_{36}$. It is quite normal to split the fields into magnitude and direction, that is $\vec{E}(\omega_n) = \hat{e}_n E(\omega_n)$, where $\hat{e}_n$ is a unit vector. A scalar quantity d_{eff} which is known as the effective nonlinear coefficient is commonly used which hides the details of the tensor multiplication

$$d_{eff} = \hat{e}_p \cdot [\vec{d}(\omega_n, \omega_m) : \hat{e}_n \hat{e}_m].$$

This allows the vector representation for the nonlinear polarization as

$$\vec{P}(\omega_n, \omega_m) = 2\epsilon_0 \vec{d}(\omega_n, \omega_m) : \vec{E}(\omega_n)\vec{E}(\omega_m).$$

2.3.1 Calculation of the effective nonlinear coefficient

To demonstrate the procedure used to calculate the effective nonlinear coefficient, a crystal belonging to the $\bar{4}2m$ crystal class is considered. In these crystals, there are two different propagating waves, one with polarization normal to the optical axis of the crystal known as ordinary wave and the second with a polarization parallel to the optical axis of the crystal known as extraordinary wave. The characteristics of these ordinary and extraordinary waves and their contributions to the DFG process will be discussed in more detail in the next chapter. For the ordinary wave the electric field vector $\vec{E}$ is perpendicular to the z-direction and hence

$$\vec{E}_o^{\omega_n} = E_o^{\omega_n}[-\sin\phi\hat{e}_x + \cos\phi\hat{e}_y + 0\hat{e}_z] \tag{2.35}$$

and for the extraordinary wave

$$\vec{E}_e^{\omega_m} = E_e^{\omega_m}[\cos\theta\cos\phi\hat{e}_x + \cos\theta\sin\phi\hat{e}_y - \sin\theta\hat{e}_z]. \tag{2.36}$$

These situations are depicted in Figure 2.3. Therefore, in the non-degenerate interaction the components of the macroscopic polarization can be expressed as

$$\begin{aligned} P_x^{\omega} &= -\varepsilon_0 d_{14} E_o^{\omega_n} E_e^{\omega_m} \cos\phi \sin\theta \\ P_y^{\omega} &= \varepsilon_0 d_{14} E_o^{\omega_n} E_e^{\omega_m} \sin\theta \sin\phi \\ P_z^{\omega} &= \varepsilon_0 d_{36} E_o^{\omega_n} E_e^{\omega_m} \cos\theta \cos 2\phi. \end{aligned} \tag{2.37}$$

If the generated radiation due to the macroscopic polarization is an ordinary wave[3] then

$$\begin{aligned} P_o^{\omega} &= P_x \sin\phi - P_y \cos\phi \\ &= -\varepsilon_0 d_{36} E_o^{\omega_n} E_e^{\omega_m} \sin\theta \sin 2\phi \end{aligned} \tag{2.38}$$

where the Kleinman symmetry is applied so that $d_{14} = d_{36}$. Therefore, the effective nonlinear coefficient d_{eff} can be defined as

$$d_{eff} = -d_{36} \sin\theta \sin 2\phi. \tag{2.39}$$

The d_{eff} is maximum if $\theta = 90^\circ$ and $\phi = 45^\circ$, and hence $d_{eff,max} = d_{36}$.

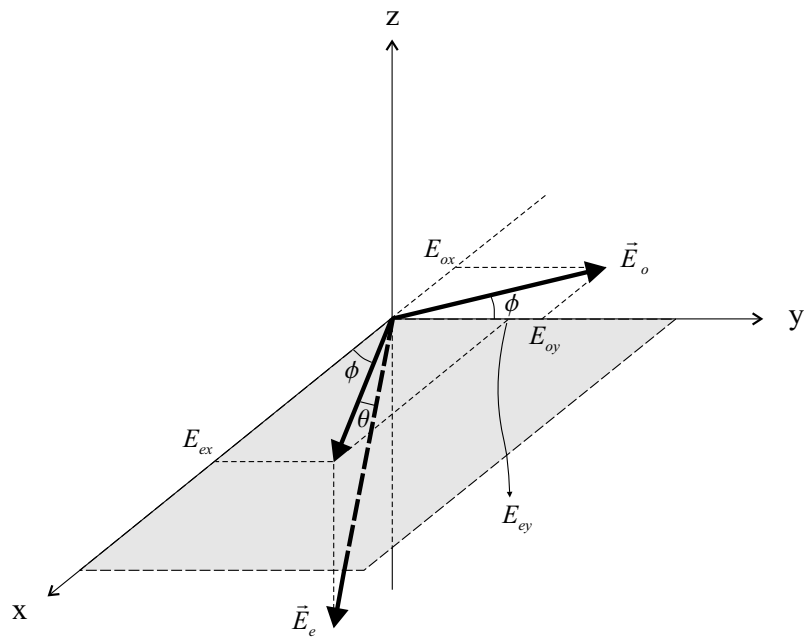

Figure 2.3: *Indication of the projection of the electric fields for two orthogonally polarized waves onto the coordinate axis.*

[3]This is known as type I nonlinear interaction which will be discussed in detail in the next chapter.

3 Difference-frequency generation (DFG) in nonlinear media

3.1 Qualitative considerations

Difference-frequency generation is a frequency down-conversion process which is due to the macroscopic polarization induced by an applied electromagnetic field. The nonlinear polarization gives rise to a new radiation at difference frequency of two incident waves and it can be used to describe the response of the nonlinear optical crystal. The importance of the induced polarization can be understood from the fact that any oscillating dipole also emits radiation at the frequency of oscillation, and thus modifies the optical field that induced the polarization. To demonstrate the difference-frequency down-conversion qualitatively a nonlinear medium which is subjected to a total electric field is assumed[23]:

$$\vec{E}(\vec{r},t) = \sum_i \vec{E_i}(\vec{r})\cos(\omega_i t - \vec{k_i}\cdot\vec{r}) \tag{3.1}$$

where the wave vector $\vec{k_i}$ and the angular frequency ω_i are related through the refractive index of medium by $|\vec{k_i}| = \frac{n_i\omega_i}{c}$. Substituting for E components from the above equation into the Equation (2.5) and assuming the interaction at $z = 0$, gives

$$\begin{aligned} P_{NL}^{(2)} &= \frac{1}{2}\epsilon_0 \sum_{jk} \chi_{ijk}^{(2)}\{(E_{1j}E_{1k} + E_{2j}E_{2k}) \\ &\quad + E_{1j}E_{1k}\cos(2\omega_1 t) + E_{2j}E_{2k}\cos(2\omega_2 t) \\ &\quad + 2[E_{1j}E_{2k} + E_{2j}E_{1k}][\cos(\omega_1+\omega_2)t + \cos(\omega_1-\omega_2)t]\}. \end{aligned} \tag{3.2}$$

It can be seen that in addition to the dc component, the nonlinear polarization has Fourier components at second harmonic frequencies $2\omega_1$ and $2\omega_2$, at the sum frequency at $\omega_1+\omega_2$ and difference frequency at $\omega_1-\omega_2$. Physically, the difference frequency component of the polarization at $\omega_1-\omega_2$ can act as a source of polarization at ω_3 with power flow from the fields at ω_1 into those at ω_2 and ω_3. Therefore, in the difference-frequency mixing process, the lower *signal* frequency photon at ω_2, stimulates the split of the highest *pump* frequency into two photons, one at ω_2 and one at the lowest *idler* frequency at ω_3 [24]. Thus both photons at ω_2 and ω_3, are amplified and the interaction between these three fields has gain. This phenomena can be better understood in terms of the quantum theory of radiation as discussed briefly in the previous chapter. For example, two photons can be annihilated to produce a new photon that carries the energy of the two that disappeared. What idler frequency will be generated in the DFG process is governed by the conservation

laws which can be written as:

$$\begin{array}{ll} \text{Energy conservation:} & \omega_3 = \omega_1 - \omega_2 \\ \text{Momentum conservation:} & \vec{k_3} = \vec{k_1} - \vec{k_2}. \end{array}$$

In this three-frequency mixing process two input waves at frequencies ω_1 and ω_2 interact together to generate an output at frequency ω_3, and the output in turn interacts with each of the inputs. For a nonlinear medium with a plane boundary at $z = 0$, two waves at ω_3 are propagating in the medium starting with almost equal amplitude and positive phase [25]:

- one wave which is a solution of the homogeneous wave equation with wave number $k_3 = \frac{\omega_3}{c} n(\omega_3)$, and
- the other which is a solution of the inhomogeneous wave equation driven by the nonlinear polarization, with the wave number $k_3 = \frac{\omega_2}{c} n(\omega_2) - \frac{\omega_1}{c} n(\omega_1)$.

The generated *driven* wave is a time-varying polarization wave and it radiates a *free* electromagnetic wave. However this interaction does not reach an equilibrium, but there is a periodic energy exchange. The exact nature of this exchanging depends on the *phase* relationship between the different waves and for the energy to be coupled from the driven wave to the free wave, the latter has to have a phase lead. For the optimum coupling this lead has to be 90°. Further, the relative phase of the interacting waves determines the direction of the generated power flow. The energy exchanging in this wave-mixing process can be compared to the energy exchange between two weakly coupled pendulums. If the pendulums have identical periods, all the energy is transferred from one to the other and back again in a given time, otherwise only a part of the energy is transferred within a shorter time. In addition to the direction of energy flow, the amount of the energy stored in any electromagnetic field can also be performed by the work which is done on the bound electric charges (i. e. dipoles) in the medium by the applied electric field. This stored energy can be stated in term of the energy density u as [26]

$$-\frac{\partial}{\partial t} \int_{volume} u dv = \int_{surface} \vec{I} \cdot \vec{ds} + \int_{volume} \langle \vec{E} \cdot \frac{\partial \vec{P}}{\partial t} \rangle$$

where

$\int_{volume} \langle \vec{E} \cdot \frac{\partial \vec{P}}{\partial t} \rangle$ is the average of the work done by the applied electric field on the polarization density. Therefore :

- if it is zero then the continuity equation is obtained; the energy lost in the medium is equal to the net power flowing through the surface bounding the medium i.e. $\int_{surface} \vec{I} \cdot \vec{ds}$

- if it is not zero, some of the energy "lost" is transferred to the medium via the polarization density. In the case of linear optics where the susceptibility is real there is no work that is done by the applied electric field, and thus the field and the polarization vectors are in phase. However, in dielectric media the situation is different:

    1. when the phase difference between the polarization and the electric field $\Delta\phi$ is $0 < \Delta\phi < \pi$, work is done by the electric field on the polarization and the field amplitude decreases. This is the case of absorption where the energy "lost" appears in the form of *heat* or other radiations.
    2. when $-\pi < \Delta\phi < 0$, the electric field would do negative work on the polarization density which means the medium does work on the applied field and therefore, the field amplitude grows. At this moment the power flowing out through the surface of the medium increases. **This is the case of nonlinear optics where an amplification of the electric field occurs via nonlinear susceptibility**.

Lasers are commonly used as input waves in this energy exchanging process and therefore even if one input laser beam is weak, one can still generate a relatively strong output by making sure that the other input laser beam is strong enough. The new radiated *free* electromagnetic *idler* wave, at frequency ω_3 is essentially a laser but it operates in a different way if compared with a laser which can be explained as follows:

1. A laser derives its gain from the energy in the upper energy levels of the atoms or molecules, which has been stored through excited transitions between different states. Contrary the *idler* (ω_i) wave receives its gain from the *pump* (ω_p) and the *signal* (ω_s) waves via interaction in a nonlinear medium.

2. The tuning range or *bandwidth* of a laser is limited because these transitions have an inherent *linewidth*. In contrast the tunability of a DFG laser depends mainly on the special characteristics of the medium and the tunability of the input sources.

3. Laser activity can be achieved only when the *population inversion* is realized and the gain in the active medium exceeds the total cavity loss. In contrast, population inversion is not required for an *idler* wave in the DFG process.

3.1.1 Energy coupling in the DFG process

For efficient energy coupling to the new generated *idler* light both energy and momentum need to be conserved. The possible DFG wavelengths are specified by the energy conservation law which is considered in the coupled equation

$$\frac{1}{\lambda_i} = \frac{1}{\lambda_p} - \frac{1}{\lambda_s} \tag{3.3}$$

and the phase difference between the interaction waves is governed by the momentum conservation law

$$\Delta\vec{k} = \vec{k_p} - \vec{k_s} - \vec{k_i} \tag{3.4}$$

where $\Delta\vec{k}$ describes the phase mismatch between the driven polarization wave and the free electromagnetic wave, resulting from different phase velocities in the nonlinear crystal. A typical nonlinear crystal causes the frequency dependent dispersion and hence leads to the *group velocity dispersion* (GVD). The physical consequence of the dispersion is that the polarization wave and the electromagnetic input wave will turn out of phase and therefore the radiation at frequency ω_i will be stopped and even reversed if the phase differs by 180°. Then destructive interference will take place and the original build up of the wave at ω_i will be destroyed. Therefore, if there is dispersion, the phase relationship between three interacting waves changes with the interaction length and complete conversion is never achieved. Instead, the wave at ω_i is built up only over a special length known as *coherence length*. It is a measure of the maximum interaction length over which amplification of parametric fields can be sustained in the presence of dispersion [14]. After travelling this length, the phase difference between the *driven* and the *free* waves is changed by π radian. This phase shift leads to a reversal of the energy flow between those waves after every coherence length; in the first coherence length output power at ω_i is produced and in the second section there is an out of phase generation at ω_i resulting in a low *frequency conversion efficiency*. For efficient frequency conversion, the critical requirement is that the interacting waves must stay in phase along their path through the nonlinear medium. However, in the presence of dispersion, only the frequency for which this dispersion has been compensated is generated efficiently. For this frequency the interaction is said to be *phase-matched*.

3.2 Phase matching in frequency-mixing process

The phase matching can be most easily understood by considering the interaction to occur between an optical wave and an identical nonlinear polarization source wave at the same frequency. As long as those waves travel with the appropriate relative phase, energy is transferred constructively into the optical wave. The maximum energy transformation only occurs within the coherence length as mentioned above. Phase matching can simply be divided into [27]

1. Noncollinear, and

2. Collinear beam propagation.

The effects of noncollinear phase-matching are discussed in References [28] and [29] theoretically and experimentally, respectively. The collinear phase-matching can also be subdivided into *critical* and *noncritical* phase-matching. In the noncollinear type the angle between the three interacting waves plays an important role in the efficiency of the DFG process. When this angle is too large, the overlap region between the focused beams becomes too small and the efficiency of the DFG conversion decreases. Maximum overlap is achieved for collinear propagation of all three waves where the momentum conservation can be written in a scalar form. Immediate physical consequence of the phase-matching is the conservation of the linear momentum $\vec{p}$, so that $\Delta\vec{k} = 0$, which is the key point for the efficient conversion when followed by the "Maxwell equation" treatment. Clearly $\Delta\vec{k} = 0$ is satisfied if $\Delta n = 0$, which is obviously a hard task. Therefore, the success of any nonlinear optical process depends upon compensating for the frequency-dependent dispersion of the phase velocities, that is offsetting the effect of dispersion so that the interacting waves travel in synchronism inside the nonlinear crystal.

3.2.1 Birefringent phase-matching

The most common technique to obtain phase-matching is to use *birefringence* to compensate for the dispersion. The basic idea of birefringent phase-matching is that the interacting waves of different frequencies are polarized differently, so that their corresponding phase velocities can be adjusted so that the phase-matching condition can be satisfied. This situation can be realized in *anisotropic* crystals where the inversion symmetry is lacking [30]. In such media the second-order susceptibility $\chi^{(2)}_{ijk}$ is nonzero. Gases and liquids are *isotropic* and, of course, can not be used for nonlinear conversion since $\chi^{(2)}_{ijk} = 0$ for those media. In such media the susceptibility is a scalar quantity and will be a complex function of frequency, and also the electric field vector is always perpendicular to the wave vector. Even for an isotropic medium in the near vicinity of the surface, where atoms occupy positions that lack the inversion symmetry the second-order susceptibility is nonzero, and therefore the generation of nonlinear surface effects is observed [31]. However, the intensity of the radiation from the surface is quite small and thus for the efficient generation of intense radiation a long optical path interaction is required, which can be realized in an anisotropic medium.

The polarization of an incoming wave on the surface of an anisotropic crystal can, in general, be written as combination of two different polarizations. Except for the specific case where the polarization is exactly parallel the *principal axes*[1] of the crystal, the polarization of the refracted beam possesses components along two different axes. Therefore, these two types of polarizations correspond to two different indices of refraction which are solutions to the "Fresnel equation". Different indices of refraction imply two different propagation

[1]The principal axes are defined as a coordinate system in the crystal for which the susceptibility tensor is diagonal.

directions. The physical effect of the double refraction or birefringence is thus, the splitting of an incoming wave into two waves with orthogonal polarizations that propagate under different angles through the crystal. The dielectric energy density associated with the incoming electric field is

$$U_e = \frac{1}{2}\vec{D}\cdot\vec{E} = \frac{1}{2}\left[\frac{D_x^2}{\epsilon_x} + \frac{D_y^2}{\epsilon_y} + \frac{D_z^2}{\epsilon_z}\right] \tag{3.5}$$

where $\vec{D}_i = \epsilon_i \vec{E}_i$ is the displacement vector. Normalizing the $\vec{D}$ field by $\vec{r} = \frac{\vec{D}}{\sqrt{2\epsilon_0 U_e}}$ leads to the equation of an *ellipsoid* as

$$\frac{x^2}{n_x^2} + \frac{y^2}{n_y^2} + \frac{z^2}{n_z^2} = 1 \tag{3.6}$$

where $n_i = \sqrt{\frac{\epsilon_i}{\epsilon_0}}$. The ellipsoid associated with Equation (3.6) is shown in Figure 3.1.

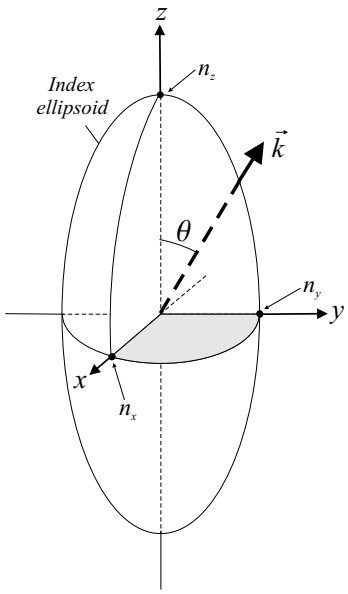

Figure 3.1: *The index ellipsoid for determination of the refractive indices of ordinary and extraordinary waves.*

This ellipsoid is known as *index ellipsoid*, and it can be used to find two indices of refraction for two orthogonal polarizations which describe the relative energy distribution among the specific direction. Crystals are classified according to certain structural symmetries which, in turn, impose symmetries upon the index ellipsoid :

1. Type (1); These include for example Si, GaAs, and CdTe crystals. They have cubic symmetry and three equivalent directions $\epsilon_1 = \epsilon_2 = \epsilon_3$. In this case the ellipsoid is a sphere and the material is isotropic.

2. Type (2); These include for example calcium carbonate, quartz, $LiNbO_3$, $AgGaS_2$ and calcium sulfide. They have trigonal, tetragonal, or hexagonal structure. There

is one axis of symmetry, which is one of the principal axes, thus $\epsilon_1 = \epsilon_2 \neq \epsilon_3$. Such crystals are known as *uniaxial* crystals [2]. Uniaxial crystals have a single optical axis and for two identical indices of refraction the plane intersecting perpendicular to the one optical axis forms a circle. Therefore

$$\frac{x^2}{n_o^2} + \frac{y^2}{n_o^2} + \frac{z^2}{n_e^2} = 1 \tag{3.7}$$

where $n_o = n_x = n_y$ and $n_e = n_z$ are the ordinary and extraordinary refractive indices, respectively. If the direction of the wave vector makes a certain angle to the optical z-axis, then n_o and n_e can be found from the intersecting plane of the ellipsoid perpendicular to the wave vector. n_o is independent of the direction of propagation just as in optically isotropic crystals, and the corresponding ordinary wave has a polarization normal to the optical axis. The corresponding phase velocity in the ordinary direction is then $v_{po} = \frac{c}{n_o}$. n_e builds a wave with the polarization vector in the plane containing the optical axis and hence the phase velocity of $v_{pe} = \frac{c}{n_e}$ which depends on the direction of propagation. The difference $\Delta n = n_e - n_o$ is a measure of birefringence. If $\Delta n < 0$ the crystal is said to be a uniaxial *negative* crystal and if $\Delta n > 0$ then it is a uniaxial *positive* crystal. Many useful transparent crystals in nonlinear optics have a very small birefringence ($|\Delta n| \ll 1$) and $\vec{E}$ and $\vec{D}$ are parallel. For a propagation at an angle θ with respect to the z-axis, the extraordinary refractive index and hence the corresponding phase velocity is a function of θ so that [32]

$$n_e(\theta, \lambda) = \frac{n_e n_o}{\sqrt{n_o^2 \sin^2\theta + n_e^2 \cos^2\theta}} \tag{3.8}$$

as can be seen in the Figure 3.2. In the special case where $\theta = 0$ there is no birefringence; both polarizations have the same refractive index n_o. Therefore, the dispersion properties of a uniaxial nonlinear crystal are determined only by the angle between the direction of propagation and the optical axis of the crystal. To find the phase-matching direction in a typical uniaxial crystal it is sufficient to determine the corresponding angle θ_{pm} for three interacting waves which is independent of azimuthal angle ϕ. However, at the same time the efficiency of the nonlinear conversion process is determined by both θ_{pm} and ϕ.

3. Type (3); these crystals have no axis of symmetry ($\epsilon_1 \neq \epsilon_2 \neq \epsilon_3$). Their typical structures are orthorombic, monolitic or triclinic. All three principal axes of the ellipsoid are different which is the characteristic of *biaxial* crystals. Biaxial crystals have two optical axis and the phase-matching condition is satisfied by two different angles with respect to two different optic axes.

[2] In uniaxial crystals, there is a single axis of symmetry, commonly designated the z-axis, which coincides with the principal optical axis. The plane containing the z-axis and the wave vector $\vec{k}$ of the light wave is termed " principal plane " .

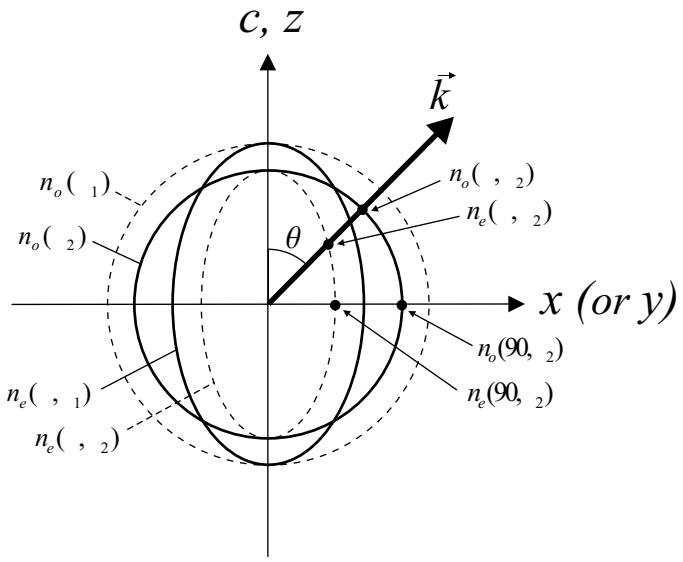

Figure 3.2: *The propagation direction as well as the refractive indices in a negative uniaxial crystal.*

3.2.2 Type of phase-matching in a uniaxial optical crystal

Two different types of phase-matching referred to as *type I* and *type II* can be identified in a uniaxial optical crystal [33]. If the polarization of signal and idler waves are identical, the type of phase-matching is known as type I (e. g. $eo \rightarrow o$ or $oe \rightarrow e$), while the case of different polarizations for signal and idler waves corresponds to type II (e. g. $eo \rightarrow e$ or $oe \rightarrow o$). The phase-matching discussed so far is achieved by propagating the input waves at a particular angle with respect to the crystal optical axis which is known as *critical* phase-matching and suffers from the *walk-off* effect arising from the dispersion, thereby affecting the nonlinear conversion efficiency even in collinear interaction. An important physical consequence for the wave propagation in anisotropic media can be considered by the *Poynting* vector. It shows the direction of the power flow in the medium and is written as

$$\vec{s} = \vec{E} \times \vec{H} \tag{3.9}$$

which in general is not along $\vec{k}$ in any anisotropic media. Therefore, when a plane light wave propagates in a uniaxial crystal, the direction of energy flow ($\vec{s}$) does not coincide with the direction of propagation. In other words, the group velocity and the phase velocity of the light beam are different and make an angle with respect to each other [34]. This so-called walk-off angle ρ can be obtained through the fact that the direction of propagation of an e-wave is not the same as the direction of energy propagation, and thus

$$\rho(\theta) = \arctan\left[\left(\frac{n_o}{n_e}\right)^2 \tan(\theta_{pm})\right] \theta_{pm} \tag{3.10}$$

As can be seen from Equation (3.10) at $\theta_{pm} = 0$ and 90° the walk-off vanishes. However, it can often be on the order of a few degrees, and is largest at $\theta_{pm} = 45°$. Therefore, for both type I and type II phase-matching the effective length of the nonlinear crystal would be limited due to the incomplete overlap of the waves during the interaction in the medium. In an isotropic medium the walk-off angle is zero.

3.2.3 Noncritical type I phase-matching

To increase the interaction length with zero walk-off, phase matching can be maintained at $\theta_{pm} = 90°$ which is known as *noncritical* phase matching (NCPM), as shown in Figure 3.3. NCPM is advantageous over critical phase-matching for four reasons [35] :

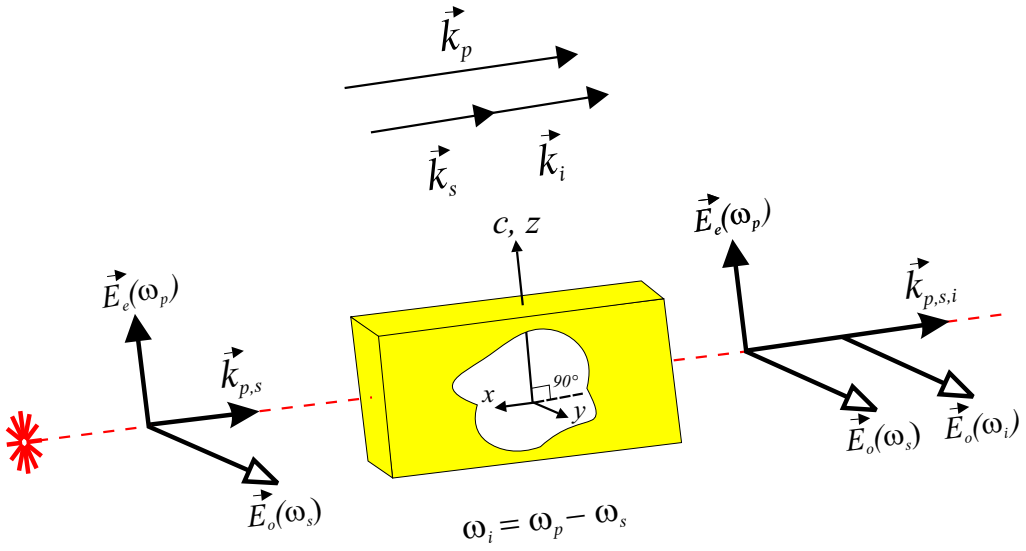

Figure 3.3: *A schematic of type I noncritical phase-matching.*

1. It is less sensitive to beam divergence which degrades the conversion efficiency,
2. The walk-off angle is zero in this case, which places less constraint on the beam size and the crystal length,
3. It allows a larger interaction length compared to $\theta_{pm} \neq 90°$,
4. The effective nonlinear coefficient d_{eff} has its largest value in this direction and hence the largest conversion efficiency is obtainable.

The indices of refraction can be changed through external influences which affect the lattice spacing of the crystal in the three dimensions. In the case of NCPM, all indices of refraction are dependent on the temperature and therefore, phase-matching can be realized

by merely changing the temperature of the crystal. By changing the temperature of the crystal $\Delta k = 0$ is realized at $\theta_{pm} = 90°$ for different wavelengths, and the phase matching condition is

$$\frac{n_o(\lambda_i, T)}{\lambda_i} = \frac{n_e(\lambda_p, T)}{\lambda_p} - \frac{n_o(\lambda_s, T)}{\lambda_s} \tag{3.11}$$

for a typical type I ($eo \rightarrow o$) DFG interaction. However, temperature tuning of the crystal is more advantageous where fast tuning is not required. In order to determine the required phase matching temperature for a given crystal, the refractive indices at the pertinent frequency have to be determined through so-called Sellmeier equations which reflect the frequency dependence of the refractive index for each crystal. A typical form of the Sellmeier equation is

$$n^2(\lambda) = A + \frac{B\lambda^2}{\lambda^2 - C} + \frac{D\lambda^2}{\lambda^2 - E}$$

where A,...,E are the constant coefficients derived from the least square fitting to measured data [36].

3.2.4 Critical phase-matching

In addition the indices of refraction of extraordinary waves are dependent on the angle of beam direction $\vec{k}$ and the polarization of the transmitted wave in the crystal and thus phase-matching can also be achieved by angular orientation of the optical axis of the crystal with respect to the propagation direction of the incident laser beams. Since the refractive index of the crystal is a function of incident wavelength at given pump and signal wavelengths, the idler wavelength corresponds to a specific phase-matching angle. The necessary phase matching angle θ_{pm} can be calculated through the following relation e.g. for type I phase matching

$$\frac{n_o(\lambda_i, T)}{\lambda_i} = \frac{n_e(\theta, \lambda_p, T)}{\lambda_p} - \frac{n_o(\lambda_s, T)}{\lambda_s}$$

where $n_e(\theta)$ is given by Equation (3.8). This type of phase matching, however, may introduce a walk-off effect in the Poynting vector for the e-wave which leads to a reduction of the spatial overlapping between the interacting waves, and thus degrades the parametric conversion efficiency. Since angle phase-matching is less sensitive to the temperature, it can be realized even at room temperature which makes it more suitable for field measurements where fast tuning is required. The effective nonlinearity d_{eff} can also be maximized in the angle phase-matching scheme if type II interaction is used [37].

3.2.5 Quasi-phase-matching (QPM)

The realization of both critical and noncritical phase-matching through birefringence does not lead necessarily to an efficient conversion since d_{eff} can be very small depending on

the type of crystal and rather for a fixed combination of used polarizations phase-matching condition can not be realized. Both the second-order nonlinear susceptibility tensor elements and the refractive indices of the crystal determine the range of the particular wavelengths at which the interaction is phase matched. Efficient nonlinear conversion requires not only that phase-matching is satisfied for the wavelength of interest, but also that the nonlinear optical coefficient corresponding to the chosen polarization direction is large. The idea behind the quasi-phase-matching (QPM) is that if two pump and idler waves are out of phase due to the propagation in a medium with nonlinear optical coefficient d_1, they can be made in-phase again if they enter to a medium with nonlinear optical coefficient with d_2 = -d_1. Therefore the effective nonlinear coefficient would be enhanced [38]. Consequently, the conversion efficiency increases continuously with the interaction length. It can be shown that the phase mismatch can be written as

$$\Delta k = k_p - k_s - k_i = \frac{2\pi}{\Lambda}$$

where $\Lambda = 2L_c$ is a modulation period of the nonlinear crystal according to the first-order QPM. The significant advantage of QPM is that any interaction within the transparency range of the material can be noncritically phase-matched at a specific engineering of crystals with an appropriate period and temperature for tuning, even interactions for which birefringent phase-matching is impossible [39]. Further, the interacting waves can be chosen so that coupling occurs through the largest element of the d-matrix.

3.3 Quantitative investigation of difference-frequency generation

The mathematics of the three-wave interaction is governed by the classical Maxwell equations. Following the derivation of an equation for the electromagnetic radiation generated at ω_i in a typical DFG process assuming $\vec{\nabla} \cdot \vec{E} = 0$ (if there is no free charge) leads to

$$\nabla^2 \vec{E}(t) = \mu\sigma \frac{\partial \vec{E}(t)}{\partial t} + \mu\epsilon \frac{\partial^2 \vec{E}(t)}{\partial t^2} + \mu \frac{\partial^2 \vec{P}_{NL}(t)}{\partial t^2} \tag{3.12}$$

where σ is the conductivity of the medium and $\vec{P}_{NL}$ is the nonlinear polarization given by Equation (2.3). To interpret the physical significance of the above nonlinear wave equation the interacting waves at ω_p and ω_s and a new generated wave at ω_i can be assumed as three plane waves propagating along the z-direction, so that

$$E(z,t) = \frac{1}{2} \sum_j [E_j(z) e^{i(\omega_j t - k_j z)} + c.c.]. \tag{3.13}$$

In the case of a DFG down-conversion process this expression can be used to account for the input beams, i. e. the pump and signal waves with components at frequencies ω_p and

ω_s, respectively. The second-order derivation of the nonlinear polarization at the difference frequency $\omega_i = \omega_p$ - ω_s according to Equation(3.2) is then

$$\frac{\partial^2}{(\partial t)^2} P_{NL}(\omega_i \ = \omega_p \ - \omega_s \ , z, t) = \\ \frac{1}{2}(\omega_p - \omega_s)^2 \epsilon_0 (2d_{eff}) E_p(\omega_p, z) E_s^*(\omega_s, z) e^{i[(\omega_p - \omega_s)t - (k_p - k_s)z]}, \tag{3.14}$$

where $E_s(-\omega_s) = E^*(\omega_s)$. Assuming that all three interacting waves are travelling in the z-direction the field gradient in Equation(3.12) can be written as

$$\nabla^2 E(z,t) = \frac{\partial^2}{\partial z^2} E(z,t)$$

and hence

$$\left[\frac{d^2}{dz^2} - \mu\sigma\frac{\partial}{\partial t} - \mu\epsilon\frac{\partial^2}{\partial t^2}\right] E(z,t) = \\ -\frac{1}{2}\left[2ik\frac{\partial}{\partial z} + k^2 + \frac{\partial^2}{\partial z^2} + i\omega\mu\sigma\frac{\partial}{\partial t} - \omega^2\mu\epsilon\frac{\partial^2}{\partial z^2}\right] E(z,t). \tag{3.15}$$

If the variation of the field amplitudes is small within the distance of one wavelength, the so-called *slowly varying amplitude* [40] approximation can be used as

$$|2ik\frac{\partial}{\partial z} E(z)| \gg |\frac{\partial^2}{\partial z^2} E(z)|$$

to simplify the Equation(3.15). Finally the equation governing the new generated idler wave at frequency ω_i in the DFG mixing process can be obtained as:

$$\frac{\partial}{\partial z} E_i(z) = -\frac{\sigma}{2}\sqrt{\frac{\mu}{\epsilon}} E_i(z) - i\frac{\omega_i \epsilon_0}{2}\sqrt{\frac{\mu}{\epsilon_i}} (2d_{eff}) E_p(z) E_s^*(z) e^{-i\Delta k z}, \tag{3.16}$$

where $\Delta k = (k_p - k_s) - k_i$ is the momentum mismatch between the driven and the free electromagnetic waves. Similarly, the equations for the two input fields $E_p(z)$ and $E_s(z)$ can be derived. However, the solution to these three coupled equations is complicated and involves elliptic integrals. In the most experimental situations the variation in the amplitude of either one or two of three frequencies can be considered negligible. Therefore, for our particular DFG case only Equation(3.16) must be considered assuming $E_p(z)$ and $E_s(z)$ are constant over the length of the crystal. The nonlinear interaction can be interpreted as a *scattering* process [38]. The phase difference Δk indicates the momentum change in the scattering event :

- if the scattering event is elastic, then $\Delta k = 0$ and momentum is conserved,
- if $\Delta k \neq 0$ then scattering is inelastic.

If we set $\sigma = 0$ at all three interacting waves to define a lossless nonlinear medium, the energy conservation in a typical DFG conversion is obtaining through three coupled equations for E_i, E_p, and E_s, respectively. This can be easily done by multiplying each separate equation to its complex conjugate. Comparing these new set of equations leads to

$$\frac{1}{\omega_i}\sqrt{\frac{\epsilon_i}{\mu}}\frac{\partial}{\partial z}(E_i E_i^*) = \frac{1}{\omega_s}\sqrt{\frac{\epsilon_s}{\mu}}\frac{\partial}{\partial z}(E_s E_s^*) = -\frac{1}{\omega_p}\sqrt{\frac{\epsilon_p}{\mu}}\frac{\partial}{\partial z}(E_p E_p^*) \tag{3.17}$$

Therefore, the requirement $\omega_i = \omega_p - \omega_s$ leads to the energy conservation since Equation(3.17) can be stated in terms of the power flow per unit area using $I = \frac{1}{2}\sqrt{\frac{\epsilon}{\mu}}EE^*$. Thus

$$\frac{1}{\omega_i}\frac{\partial I_i}{\partial z} = \frac{1}{\omega_s}\frac{\partial I_s}{\partial z} = -\frac{1}{\omega_p}\frac{\partial I_p}{\partial z}. \tag{3.18}$$

The above equation is known as *Manley* and *Rowe* relation. It states that, in the photon picture, a photon of energy $\hbar\omega_p$ splits into two photons of energies $\hbar\omega_s$ and $\hbar\omega_i$. In other words, generation of the difference frequency wave also results in parametric amplification at the lower of the two input frequencies at ω_s. Therefore in a typical DFG conversion, in addition to the generation of the output at frequency ω_i, there is an amplification of the lowest frequency input at ω_s.[3] This DFG parametric amplification is shown in Figure 3.4, schematically. This amplification occurs far from the material resonance, in which the state of the energy of the material does not change [41]. Therefore, only energy can be exchanged between waves of different frequencies, and the loss can be neglected in such media allowing the overall permutation to be valid. This might be taken into account as *forth* difference between an ordinary laser obtained from a gain media in a cavity and a difference-frequency laser.

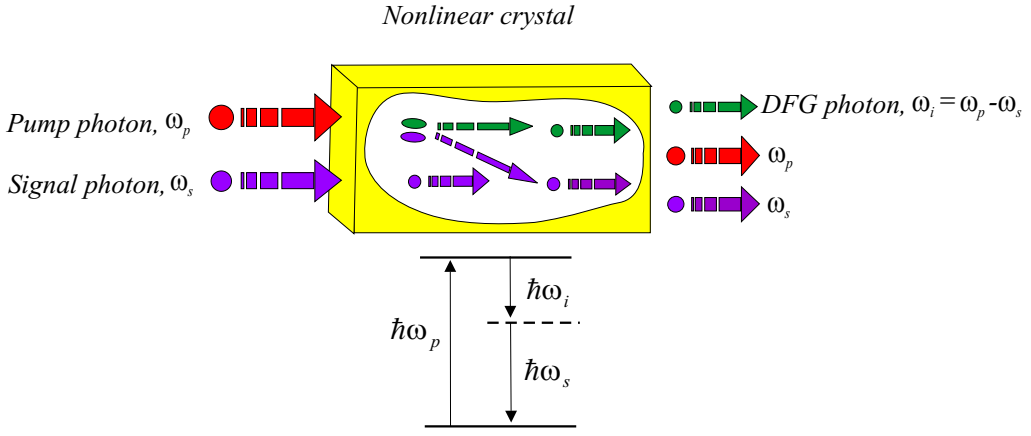

Figure 3.4: *Energy conservation diagram in a typical DFG nonlinear process.*

[3]The total number of photons in the nonlinear DFG process is of course not conserved. Therefore, $\Delta N_i = \Delta N_s = -\Delta N_p$, where N is the number of the generated and annihilated photons.

3.3.1 DFG output power density and conversion efficiency

As a result Equation (3.16) can be integrated over the crystal length L, to obtain the amplitude of the electric field just inside the exit face of the crystal. This can be done by assuming any depletion of frequency at ω_s and ω_p to be neglected as it is true in the case of low conversion efficiency, i. e. $\frac{\partial E_p}{\partial z} = \frac{\partial E_s}{\partial z} = 0$, which is quite commonly observed in the experimental situations. Including those assumptions then

$$E_i(L) = -\frac{\omega_i d_{eff}}{n_i c} E_s^* E_p \left[\frac{e^{-i\Delta k L} - 1}{\Delta k}\right]$$

and the corresponding output intensity (power density) can be obtained as

$$I_{\omega_i} = \frac{2\omega_i d_{eff}^2}{n_i n_p n_s c^3 \epsilon_0} L^2 I_p I_s \left[\frac{\sin(\frac{\Delta k L}{2})}{(\frac{\Delta k L}{2})}\right]^2 \tag{3.19}$$

where I_i, I_s and I_p are the intensities at ω_i, ω_s, and ω_p respectively, and n_i, n_s, and n_p are the corresponding refractive indices[4]. As it is clear from the above equation the output power of the generated difference-frequency radiation depends linearly on the two input powers. Therefore the efficiency of the DFG conversion is determined by the pump power density on the nonlinear crystal, and the output density power at the new generated DFG radiation is only restricted by the damage threshold of the crystal. As can be described through Equation (3.19) the *coherence factor* is defined as:

$$F_c = L^2 \left[\frac{\sin(\frac{\Delta k L}{2})}{(\frac{\Delta k L}{2})}\right]^2 . \tag{3.20}$$

A graph of the coherence factor F_c is given in Figure 3.5. The point where the function is reduced by $\frac{1}{2}$ is

$$\Delta k = \frac{2.784}{L}$$

which can be defined as *phase-matching bandwidth* at half-width at half-maximum (HWHM). The maximum output intensity at the difference-frequency ω_i is reached if the thickness of the nonlinear crystal is equal to

$$L_c = \frac{\pi}{\Delta k}$$

where L_c is the coherence length as introduced in the section 3.1.1, and there is no more advantage in using a longer crystal, since after twice the coherence length the intensity of the DFG wave falls back to zero. Therefore, the generated difference-frequency intensity oscillates as a function of the crystal length unless :

$$\Delta k = 0 \qquad \text{is satisfied.}$$

Under $\Delta k \neq 0$ condition, the interacting fields periodically step out of phase and interfere constructively and destructively as they travel through the crystal. Therefore, the solution with $\Delta k \neq 0$ is nevertheless of interest. Contrary at $\Delta k = 0$ since $F_c \to 1$ then :

[4]Here SI units are assumed.

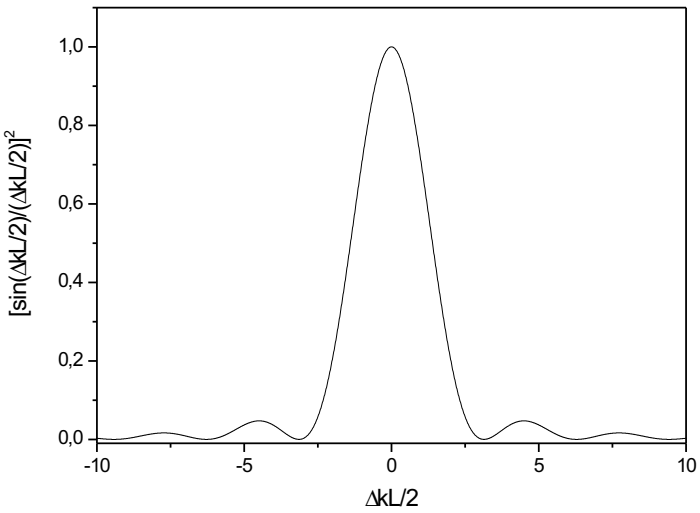

Figure 3.5: *Indication of coherence factor. The coherence factor as well as DFG output reach to the maximum when* $\Delta k = 0$.

1. according to the Equation (3.19) the DFG intensity is increased quadratically with the length of the crystal,
2. the coherence length is infinite, and
3. the phase velocity synchronism between the interacting fields can be maintained indefinitely.

If the approximation of nondepleted pump and signal waves is used, the conversion efficiency of the nonlinear frequency generation can be defined as

$$\eta = \frac{P_i}{P_s} \tag{3.21}$$

which can be related to the given parameters via Equation (3.19) for the phase-matching condition $\Delta k = 0$ so that

$$\eta = \frac{8\pi^2 d_{eff}^2 L^2}{n_i n_s n_p c \lambda_i^2 \epsilon_0} I_p. \tag{3.22}$$

Practically, the conversion efficiency η is defined as $\eta = \frac{P_i}{P_p P_s L}$ [42]. In the Equation (3.22) last expression the quantity $\frac{d_{eff}^2}{n_i n_s n_p}$ is defined as the *nonlinear figure of merit* (FOM).

3.3.2 Perfect phase-matching condition

In the derivation of Equation (3.19) the depletion of the input beams is assumed to be negligible. In the case of *perfect* phase-matching, the conversion efficiency is influenced

by some permanent effects such as *damage*, *absorption*, and *heating* of the crystal which results in the conversion efficiency to be degraded. Bulk damage and surface damage of the nonlinear crystal can occur at high power densities although the surface threshold is usually lower than the bulk damage threshold and depends strongly on the optical quality of the crystal[5]. When the effect of absorption is included, the coherence factor defined by Equation (3.20) may be replaced by [23]

$$\frac{1+e^{-\Delta\alpha L}-2e^{-\frac{\Delta\alpha L}{2}}\cos(\Delta kL)}{(\Delta kL)^2+(\frac{\Delta\alpha L}{2})^2}$$

where $\Delta\alpha=\alpha_p+\alpha_s+\alpha_i$ for the absorption coefficients α_p, α_s, and α_i at frequencies ω_p, ω_s, and ω_i, respectively. Heating of the crystal can also be related to some thermodynamical parameters of the nonlinear crystal such as the heat conduction coefficient and the environmental conditions.

3.3.3 DFG with focused Gaussian input beams

At the beginning of this section the nonlinear interactions of the input lights are treated in the plane wave approximation, which is no longer valid when the input laser beams are focused. For laser beams of constant radii w, ordinary and extraordinary beams become separated by $l\simeq\frac{2w}{\tan\rho}$, where ρ is the walk-off angle. Therefore, decreasing the beam size (i. e. focusing the beam) is often used to enhance the conversion efficiency due to a appreciable increase in the intensity and a reduced separation of ordinary and extraordinary beams within the interacting length. In the absence of absorption, the center of the crystal should be at the optimum location of the focus, as shown in Figure 3.6. To include the effect of the focusing in the DFG process the focusing factor $h(\mu,\xi)$ is introduced by Boyd and Kleinman [43] and for 90° noncritical phase-matching it can be written as

$$h(\mu,\xi)=\frac{1}{2\xi}\int_0^{\xi}d\tau''\int_{-\xi}^{\xi}d\tau'\frac{1+\tau'\tau''}{(1+\tau'\tau'')^2+\frac{1}{4}\left[\frac{(1-\mu}{1+\mu}\right]+\left[\frac{(1-\mu}{1+\mu}\right]^2(\tau'-\tau'')^2},$$

where

$$\mu=\frac{k_s}{k_p}\qquad\text{and}\qquad\xi=\frac{L}{b}$$

are dimensioless parameters and provide the optimum focusing. b is known as confocal parameter which is defined as

$$b=k_pw_{0p}^2=k_sw_{0s}^2$$

Therefore, the DFG output power can be written as

$$P_i=\frac{4\omega_i^2d_{eff}^2L}{n_sn_pn_i\epsilon_0\pi c^3}\cdot\frac{k_s}{1+\mu}h(\mu,\xi)P_sP_p \tag{3.23}$$

[5]Damage threshold for short pulses is normally higher than that for continuous wave (cw) radiation. Also it increases by decreasing the repetition rate of the pulses.

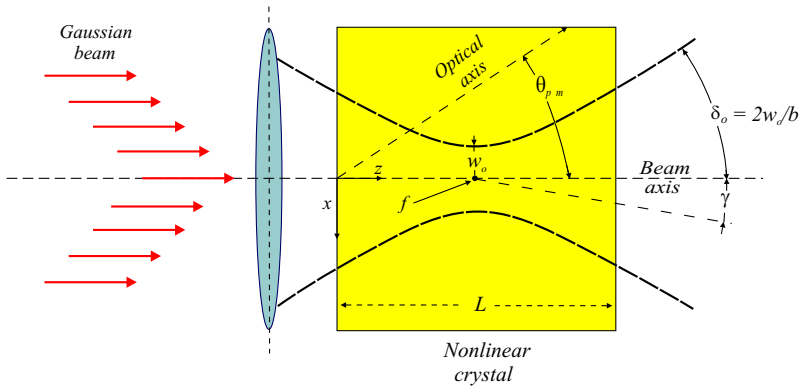

Figure 3.6: *DFG conversion with focused beams. In the efficient DFG process two inputs should be focused at the center of the nonlinear crystal. δ_0 is the diffraction half-angle and γ is the double refraction angle.*

Therefore, the DFG output power is proportional to the length of the crystal L when Gaussian input beams are applied while it is proportional to the L^2 when the plane-wave approximation is assumed [in according to Equation (3.19)]. In the case of the near-field approximation $\xi \to 0$ and $h(\mu, \xi) \to \xi$ then the power can be written as:

$$P_i = \frac{4\omega_i^2 d_{eff}^2}{n_s n_p n_i \epsilon_0 \pi c^3} \cdot \frac{L^2}{\omega_s^2 + \omega_p^2} h(\mu, \xi) P_s P_p. \tag{3.24}$$

Equation (3.24) is the practical useful formula as it is applied by Pine [44] to estimate the DFG output power obtained from $LiNbO_3$ nonlinear crystal[6].

3.4 Silver thiogallate ($AgGaS_2$) as efficient nonlinear optical crystal

In the nonlinear mixing process the nonlinear crystal is the heart of the system. Since the discovery of second-harmonic generation (SHG) by Franken et. al. in 1961, efforts have been made and are still ongoing to develop efficient nonlinear crystals for nonlinear conversion processes. Every nonlinear crystal should have :

1. a wide transparency range for all three interacting waves,
2. large birefringence,
3. high damage threshold, and
4. a large nonlinear coefficient.

[6]If the absorption of the nonlinear crystal is included, a new focusing factor $h(\mu, \xi, \alpha)$ should be defined through a so-called *double refraction parameter* as $B = \frac{\rho}{2}\sqrt{(k_p - k_s)L}$.

Silver thiogallate ($AgGaS_2$) is perhaps the most suitable crystal for DFG down conversion within its transparency region which is typically reported from 0.47 to 13 μm as shown in Figure (3.7) [45]. It is 90° phase matchable from 2 to 10 μm. Due to the two-photon absorption around 14 μm its transparency decreases beyond 15 μm. In this wide transparency range, many visible and near-infrared (NIR) lasers can be used as pump and signal sources to set up a DFG laser in the mid-infrared region. $AgGaS_2$ is a negative uniaxial crystal[7] and it belongs to the $\bar{4}2m$ crystal group. Its effective nonlinear coefficient can be written as

$$\begin{aligned} d_{eff} &= -d_{36}\sin\theta\sin 2\phi \qquad \text{for type I phase-matching} \\ &= d_{36}\sin 2\theta\cos 2\phi \qquad \text{for type II phase-matching,} \end{aligned}$$

with $d_{36} = 17.5\frac{pm}{volt}$ at $\lambda = 1064nm$ [45]. For various wavelengths a wide range of values for the d_{36} nonlinear coefficient from 9 to 57 $\frac{pm}{volt}$ of $AgGaS_2$ has been reported [46, 47]. From the various reported values for the Miller parameter δ_{36}, the one given by Yodh et al. (1991)($\delta_{36} = 0.08\ \frac{pm}{volt}$) has proven to be the most useful to predict the DFG output power [48]. The nonlinear coefficient of $AgGaS_2$ is found to be four times larger than that of $LiNbO_3$. It shows a large damage threshold if irradiated by pulsed laser sources ($P_D \sim 10\ \frac{MW}{cm^2}$ at $\lambda = 694$ nm and $\tau = 10$ ns) and is less sensitive to damage by visible laser radiation [49]. Due to the poor thermal conductivity of $AgGaS_2$ ($\kappa \sim 0.115\frac{W}{cm\cdot K}$) it suffers from *thermal lensing* effects, especially if high power pump sources at wavelengths close to the band gap of the material ($\lambda \sim 500$ nm) are used [50]. For a given mixing wavelength the phase-matching condition is relatively insensitive to the crystal orientation.

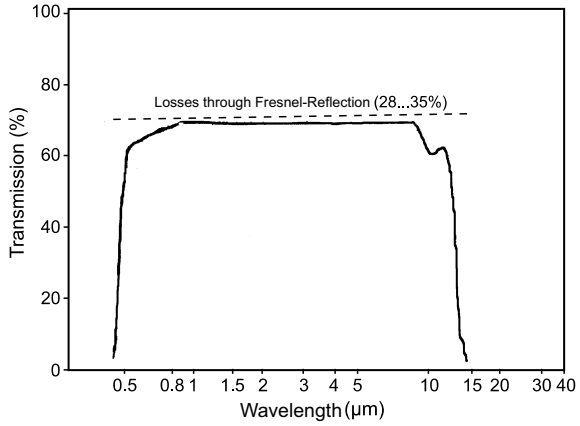

Figure 3.7: *Transparency region of the $AgGaS_2$ nonlinear crystal [45].*

3.4.1 Sellmeier and temperature-dispersion equations

The refractive index of any optical material can be calculated through Sellmeier equations as functions of the input wavelength λ at room temperature. As reviewed by Willer et

[7] At wavelengths $\lambda < 0.497\mu m$ it is known as possitive uniaxial crystal.

al. [51] the first Sellmeier equation of the $AgGaS_2$ nonlinear crystal was reported by Chemla et al. in 1971 [52] in the form of

$$n_{e,o}^2 = A_{e,o} + \frac{B_{e,o}}{\lambda^2 - C_{e,o}} - D_{e,o}\lambda^2$$

where A, B, C, and D are the corresponding coefficients for the extraordinary and ordinary beams. Three years later, the form of the above Sellmeier equation was modified by Bhar and Smith [53] with a new set of different coefficients compared to that of Chemla et al. as:

$$n_{e,o}^2 = A_{e,o} + \frac{B_{e,o}}{1 - \frac{C_{e,o}}{\lambda^2}} + \frac{D_{e,o}}{1 - \frac{E_{e,o}}{\lambda^2}}$$

In 1984 Fan et al. [54] obtained different coefficients for the Sellmeier equation with the same form as Bhar and Smith to provide a basic equation for the experimentalists. Soon after the Sellmeier equation was modified again either in its form or in its coefficients by

- Kato in 1984 [55],
- Bhar in 1988 [56],

and most recently

- Roberts in 1996 [57], and
- Takaoka and Kato in 1999 [58].

However, in the literature from 1971 since then the calculation of experimental parameters such as phase-matching angle and temperature have not been fitted to those calculated by using one Sellmeier equation. The temperature-dispersion equation of $AgGaS_2$ which is the dependency of the refractive indices on the temperature dn/dT has also been investigated. Bhar et al. in 1983 [59] published this dependency in the form:

$$2n_{e,o}\frac{dn_{e,o}}{dT} = A_{e,o}R_{e,o} + B_{e,o}R_{e,o}^2, \qquad R_{e,o} = \frac{\lambda^2}{\lambda^2 - \lambda_{ge,o}^2} \tag{3.25}$$

where A, B, and R are the corresponding extraordinary and ordinary coefficients and λ_g is the constant band wavelength corresponding to those extraordinary and ordinary waves. Most recently Takaoka and Kato [58] have developed new temperature-dispersion equations as

$$\begin{aligned}\frac{dn_o}{dT} &= \left(\frac{0.3180}{\lambda^3} + \frac{2.8968}{\lambda^2} - \frac{0.8685}{\lambda} + 15.2679\right) \times 10^{-5} \\ \frac{dn_e}{dT} &= \left(\frac{6.1742}{\lambda^3} + \frac{12.0868}{\lambda^2} - \frac{8.2485}{\lambda} + 14.4365\right) \times 10^{-5}\end{aligned} \tag{3.26}$$

which have proven to be extremely useful for the estimation of the parameters for angle and temperature phase-matching for $AgGaS_2$. Most recently, the accuracy of all the available Sellmeier and temperature-dispersion equations for $AgGaS_2$ have been considered and compared to the obtained experimental results in the DFG down-conversion process by Willer et al. [51]. This complete investigation indicates that the Sellmeier equation provided by Roberts [57] and the temperature-dispersion equation given by Takaoka and Kato [58] are in good agreement with the measured data compared to the other equations as shown in Figure 3.8 for a typical 90° type I noncritical phase-matching DFG process in a $AgGaS_2$ nonlinear crystal.

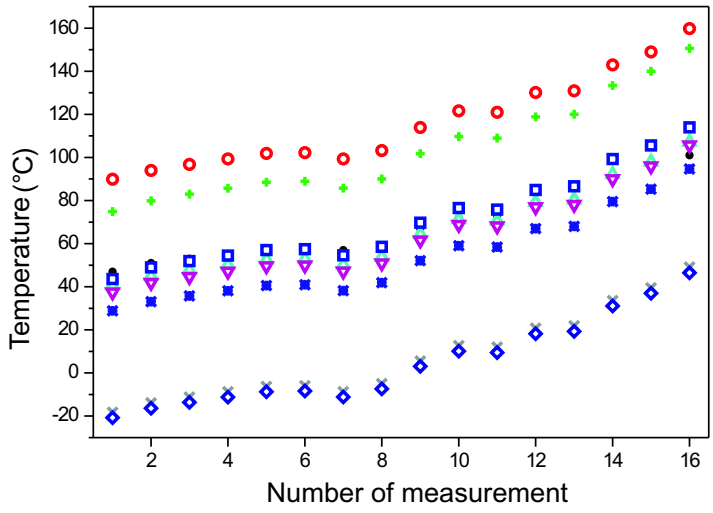

Figure 3.8: *Measured (•) and calculated phase matching temperature obtained from different Sellmeier and temperature-dispersion equations. The best results are obtained regarding the equations from (⋆)Takaoka and Kato and from (▽) Roberts [51].*

3.4.2 Temperature phase-matching bandwidth in nonlinear crystals

In the real frequency conversion some factors such as diverging of the converted radiation and crystal temperature instabilities should be taken into account. In the mathematical language these factors may be calculated in terms of angular, spectral, and temperature bandwidths which correspond to the maximum permissible deviations from the stable conditions. Since $\Delta\vec{k}$ is a function of phase-matching temperature T, frequencies of interacting waves ν, and the deviation from the phase-matching angle $\delta\theta = \theta - \theta_{pm}$, $\Delta\vec{k}$ can (for a first approximation) be expanded in a Taylor series as:

$$\Delta k \backsimeq \Delta k(0) + \frac{\partial(\Delta k)}{\partial T}\Delta T + \frac{\partial(\Delta k)}{\partial \delta\theta}\Delta\delta\theta + \frac{\partial(\Delta k)}{\partial \nu}\Delta\nu, \tag{3.27}$$

where $\Delta k(0)$ is the mismatch for the exact phase-matching and therefore it can be set to zero. To determine the temperature bandwidth, the second term in the right-hand side of the last equation can be used for a typical type I interaction. Therefore, ΔT_{BW} can be calculated as

$$\Delta T_{BW} = \frac{\Delta kL}{2\pi \left[\frac{1}{\lambda_p}\frac{\partial n_p^e}{\partial T} - \frac{1}{\lambda_s}\frac{\partial n_s^o}{\partial T} - \frac{1}{\lambda_i}\frac{\partial n_i^o}{\partial T}\right]} \tag{3.28}$$

where $\Delta kL = 2.784$ is the phase-matching bandwidth at HWHM.

4 Mid-infrared laser spectroscopy

4.1 Molecular spectra

The main target of quantitative spectroscopic measurements is to determine macroscopic parameters such as concentration, temperature, and the speed of a gas flow through trace gas detection in both laboratory and industrial scales. The requirement for such measurements is to determine the macroscopic parameters through the microscopic structure of atoms and molecules within a gas system. Each atom and molecule is characterized by a set of energy levels. In atoms, the energy levels, and orbital configurations depend on the states of the electrons which can be represented by four quantum numbers n, l, m, and s. The probability of an electron with a particular energy being at a particular state, can be predicted through solving the wave function Schrödinger equation. In the presence of a radiation field transitions can occur between the energy levels of a typical molecule. In the quantum mechanics point of view, two eigen-wave-functions of atomic states should satisfy the orthogonality condition. The statement that " *two wave functions are orthogonal* " is the same as the statement that " *the overlap of those states characterized by wave functions is zero* ". In the spectroscopy language such states are represented by orthogonal wave functions and " *do not mix* ". If the applied radiation field is represented by E then the transition will occur if

$$\langle \phi_m | E | \phi_n \rangle \neq 0.$$

Therefore, the transitions between these energy levels is governed by some *selection rules* identified by [19]:

$$\Delta l = \pm 1, \Delta J = 0, \pm 1 \qquad J = 0 \rightarrow J = 0 \text{ is not allowed,}$$

where l is the orbital angular momentum and J is the total angular momentum of the atom. These selection rules indicate that transition are allowed between any S level ($l = 0$) and any P level ($l = 1$), but the transition between P and D level ($l = 2$) is more complex, since the second rule on J should be satisfied, simultaneously. In molecules the situation is different and more complex. In a molecule, atoms do not remain in a fixed relative positions and three separate effects can be identified. The molecular transitions may be classified as

1. electronic,
2. vibrational, and
3. rotational

transitions when the molecule is subjected to an electromagnetic radiation. Because of the very different orders of magnitude of the spacing of electronic, vibrational, and rotational energy levels, molecular transitions occur in three different regions of the spectrum. Thus, the total energy of the molecule is

$$E_{total} = E_{elec.} + E_{vib.} + E_{rot.} \tag{4.1}$$

and the wave functions contain vibrational and rotational as well as electronic quantum numbers. Since the electrons move faster than the nuclei, the nuclei can usually be assumed in an equilibrium position and therefore the molecule problem can be separated into an electronic and a nuclear one, where the rotational modes are unaffected by the vibrational effects, since the energies of the two motions are very different. This simplification is known as *Born-Oppenheimer* approximation [60].

4.1.1 Rotational spectra of diatomic molecules

The simplest molecular motion is to consider a molecule as a rigid body whose shape is determined by the equilibrium position of the nuclei. The rotational kinetic energy of the molecule is then

$$E = BJ(J+1) \quad (cm^{-1}) \tag{4.2}$$

where $B = \frac{\hbar}{4\pi cI} \times 10^{-2}$ is the rotational constant, and $I = \mu R_0^2$ is the moment of inertia[1]. For a rotational transition the Eigen-functions of L^2 are the spherical harmonics, and the angular momentum of a rotating molecule is quantized which produces a $(2J+1)$-fold degeneracy for a rotational state. In this case the selection rule is

$$\Delta J = \pm 1$$

with forbidden $\Delta J = 0$ transition, and allowed transitions only between the adjacent levels with the energy spacing of $\Delta E_{rot.} = 2B$. Pure rotational spectra fall in the microwave of far-infrared region of electromagnetic spectrum depending on the type of the molecule. For example for the CO molecule $B = 1.92$ cm^{-1} [61], which puts the spacing between rotational levels in the microwave region. If the charge is symmetrically distributed in a molecule, as in the case of *homonuclear* diatomic molecules such as H_2 and N_2 molecules, it does not have any pure rotational spectra because of the absence of a permanent electric dipole moment of the molecule. In contrast, in *heteronuclear* diatomic molecules such as CO and NO molecules pure rotational transitions are permanently present.

4.1.1.1 Rotational transition intensity

The intensity of rotational lines is proportional to the difference population of the levels participating to the transition as final and initial levels; $\Delta N = N_{final} - N_{initial}$, while the

[1] where μ is the reduced mass of the molecule and R_0 is the center separation of two atoms of the molecule.

population of each level is determined by a Boltzman distribution. Therefore, the number of molecules occupying rotational levels is a combination of the degeneracy of a rotational level and the population of each level so that

$$\begin{aligned} N_J &= (2J+1)e^{-E_{rot.}/k_BT} \\ &= (2J+1)e^{-hcBJ(J+1)/k_BT} \end{aligned} \tag{4.3}$$

where $k_B = 0.69504 \quad \mathrm{cm}^{-1}\ \mathrm{K}^{-1}$ is the Boltzman constant and T is the absolute temperature. Thus the transition intensity reaches a maximum at a certain quantum number J and then diminishes as shown in Figure 4.1.

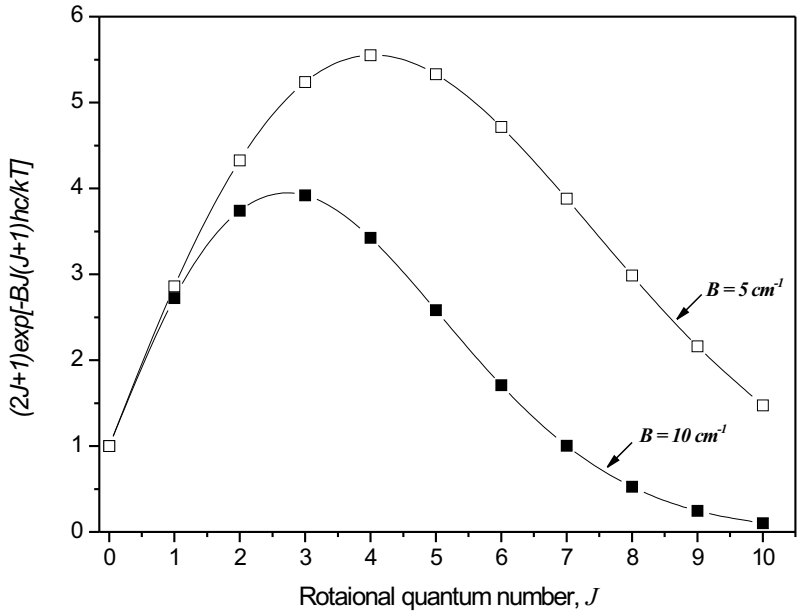

Figure 4.1: *Rotational intensity transition versus rotational quantum number J for two different rotational constant B.*

The maximum transition intensity depends highly on the J number which can be determined by [60]

$$J = \sqrt{\frac{k_BT}{2hcB}} - \frac{1}{2}. \tag{4.4}$$

In addition, the separation between energy levels with the same J number depends also on the particular *isotope* of a molecule, so that heavier species have smaller energy level separations.

4.1.2 Vibrational spectra of diatomic molecules

Each molecule can have a large number of vibrational modes such as

- symmetrical,
- asymmetrical,
- stretching, and
- bending

modes, which makes the molecular spectra very complex. A pure vibrational transition only happens for polar molecules such as HCl molecule. Like a rotating molecule, the energy levels of each of those vibrational modes are quantized, and are rather equally spaced by the order of 10^3 cm^{-1}. The potential energy for the vibrational transition modes can be approximated by the *Morse potential* ($\sim r^2$) and thus the vibrational energy levels can be written in terms of a simple harmonic oscillator as

$$E_v = (v + \frac{1}{2})\hbar\omega_0 \tag{4.5}$$

where v is the *vibrational quantum number*. For the CO molecule $\hbar\omega_0 \cong 2161.56$ cm^{-1} [19] and the vibrational transitions fall in the infrared region of the spectrum and therefore obtained by *absorption spectroscopy*. In the harmonic oscillator model for a vibrating diatomic molecule the selection rule can be obtained through solving the following equation [20]

$$\langle\phi_{v'}|p|\phi_v\rangle = \sqrt{\frac{v+1}{2}}\delta_{v',v+1} + \sqrt{\frac{v}{2}}\delta_{v',v-1}$$

which leads to

$$\Delta v = \pm 1, \tag{4.6}$$

where ϕ_v is the harmonic oscillator Eigen-function, and p represents the electric dipole transition. To be more realistic, the molecule does not vibrate harmonically, and rather the zero point energy is slightly different. By this inharmonic approximation the vibrational levels are crowded together as v increases and the selection rule given by the Equation (4.6) can be replaced by

$$\Delta v = \pm 1, \pm 2, \pm 3, ... \tag{4.7}$$

which then gives rise to numerous lines in the vibrational spectrum.

4.1.2.1 Vibrational transition intensity

The most intense transitions are those associated with $\Delta v = \pm 1$, and as Δv increases, the intensity drops rapidly. Mostly, molecules occupy the lowest vibrational state $v = 0$ at room temperature, and all the transitions starting at $v = 1$ or more can be ignored. Therefore, the most intense absorption band is the $v = 0 \rightarrow v = 1$ transition which is called *fundamental* transition. Transitions corresponding to $v = 0 \rightarrow v = 2, 3, ...$ are called *overtone* bands. When the temperature is raised the population of the $v = 1$ state may become appreciable and hence transitions starting from this vibrational state are known as *hot bands*. Different vibrational transition bands are illustrated in Figure 4.2.

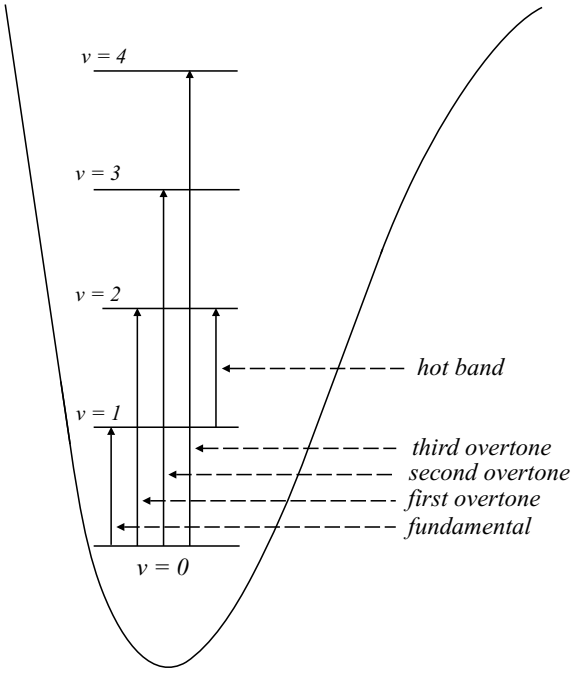

Figure 4.2: *Intensity of vibrational transition bands.*

4.1.3 The interaction of rotation and vibration (breakdown of the Born-Oppenheimer approximation)

Individual molecules may vibrate and rotate simultaneously. Transitions between molecular rotational-vibrational states occur subsequently which fall into the infrared *fingerprint* region of the electromagnetic spectrum, approximately between the wavelengths of 2.5 and 25 μm. In this spectral region the electronic states can not be excited since infrared radiation is of too low energy to do so. In the ultraviolet (UV) spectral region where the energy of photons is sufficient, the transition between electronic states can occur. In general, the excitation of vibrations requires more energy than that for rotations and thus to each vibrational level there correspond several rotational levels as shown in Figure 4.3. In

this case the total energy of the molecule is the combination of both rotation and vibration and hence the selection rules for the combined motion are the same as those for each one separately. Therefore

$$E_{total} = E_{vib.} + E_{rot.} \tag{4.8}$$

and

$$\Delta v = \pm 1, \pm 2, ... \quad \Delta J = \pm 1. \tag{4.9}$$

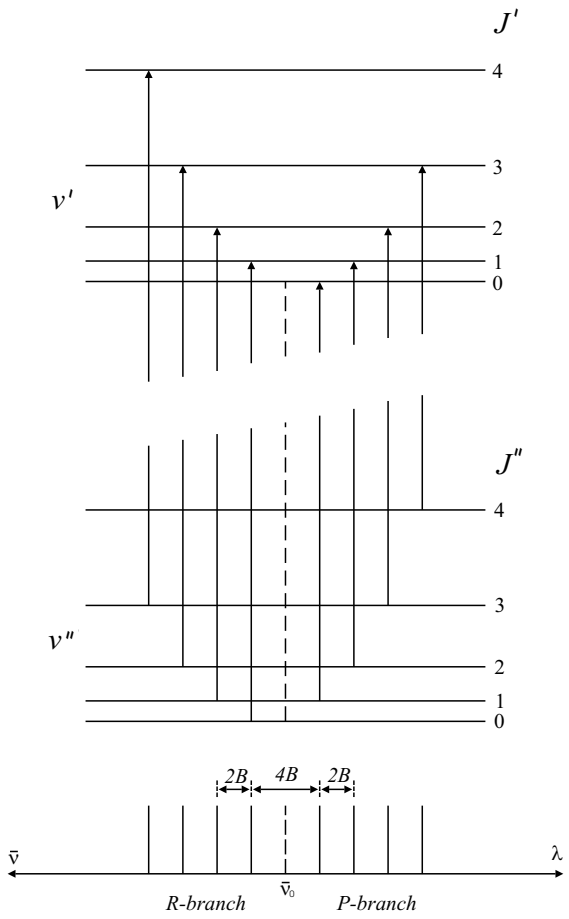

Figure 4.3: *Possible ro-vibrational levels according to the selection rules [19].*

In the case of $\Delta v = 0$ only the pure rotational transition is present. The minimum required energy for the transition between the states is then:

$$E_{field} = \hbar\omega_0 = E(v', J') - E(v'', J'') \tag{4.10}$$

and the wavenumber for such transition is

$$\bar{\nu} = [\bar{\nu_0}(v' + \frac{1}{2}) + B'J'(J'+1)] - [\bar{\nu_0}(v'' + \frac{1}{2}) + B''J''(J''+1)] \tag{4.11}$$

where $\bar{\nu_0}$ is the band origin corresponding to the forbidden transition $J' = 0 \rightarrow J'' = 0$.

Assuming that molecules are in their ground states ($v'' = 0$) at room temperature then the energy of the fundamental transitions can be obtained by using $\Delta v = 1$ as

$$\bar{\nu} = \bar{\nu_0} + B'J'(J'+1) - B''J''(J''+1)$$

where the higher order anharmonic term is ignored. Therefore, transitions between two vibrational levels are governed by the rotational selection rule, which results in an absorption spectrum consisting of two branches :

$$\begin{aligned} \Delta J &= +1 \qquad R - \text{branch} \\ \Delta J &= -1 \qquad P - \text{branch} \end{aligned}$$

as can be seen in Figure 4.3. In the transitions where the change of the vibrational number v is small (such as fundamental band), the rotational constants B' and B'' are approximately equal and hence the wavenumber of each band is

$$\begin{aligned} \Delta J &= +1, \qquad \bar{\nu} = \bar{\nu_0} + 2B(J''+1), \quad J'' = 0, 1, 2, ... \\ \Delta J &= -1, \qquad \bar{\nu} = \bar{\nu_0} - 2BJ'', \qquad\quad J'' = 1, 2, ... \end{aligned}$$

Therefore, the lines are equally spaced by $2B$ except for the gap of $4B$ around the origin $\bar{\nu_0}$ with the side bands at $J'' > 0$. However, in reality, what we observe in the spectra is slightly different. The intensity of the ro-vibrational lines should be scaled by the population of the lower J state since there is generally no thermal population in the final state.

4.1.4 Ro-vibrational spectrum of the CO molecule

The CO molecule is one of the most common pollutant gases in the atmosphere and therefore much scientific effort has been concentrated on the detection and the reduction of such a toxic molecule in combustions. The optical methods for measuring its amount in the atmosphere are well developed so that it is possible to determine the concentration-data *in-situ*. It is a major product of incomplete combustion of carbon and carbon-containing compounds. From six recognized isotopes for CO, the abundance of the $^{12}C^{16}O$ isotope in the nature is the greatest ($\sim 99\%$) compared to the other CO isotopes [62]. The fundamental ro-vibrational bands containing P- and R-branches of CO fall in the mid-infrared (MIR) region where the band origin $\bar{\nu_0}$ is centered at about 2143 cm^{-1}. The separation between two CO lines can be calculated by [60]:

$$B \simeq \frac{hc}{8k_BT}(\delta\bar{\nu})^2, \tag{4.12}$$

where $\delta\bar{\nu}$ is the separation between two maxima in the P- and R-branches. For the CO molecule this separation is $\delta\bar{\nu} \simeq 55$ cm^{-1} which gives a B value of about 1.8 cm^{-1} at room temperature. The separation between the rotational lines decreases as the wavenumber increases. The line separation for some typical CO rotational lines is given in Table 4.1.

		Separation			Separation
Line	$\bar{\nu}(cm^{-1})$	$\delta\bar{\nu}(cm^{-1})$	Line	$\bar{\nu}(cm^{-1})$	$\delta\bar{\nu}(cm^{-1})$
P(1)	2139.43		R(0)	2147.08	
		3.88			3.78
P(2)	2135.55		R(1)	2150.86	
		3.92			3.73
P(3)	2131.63		R(2)	2154.59	
		3.95			3.72
P(4)	2127.68		R(3)	2158.31	
		3.98			3.66
P(5)	2123.70		R(4)	2161.97	
.	.		.	.	
.	.		.	.	
P(26)	2032.35		R(26)	2205.95	
		4.70			2.77
P(27)	2027.65		R(27)	2208.72	
		4.74			2.74
P(28)	2022.91		R(28)	2211.46	
		4.76			2.69
P(29)	2018.15		R(29)	2214.15	

Table 4.1: *Some CO absorption lines in both P- and R-branches and the corresponding separations given in the HITRAN2003 database.*

4.1.5 Ro-vibrational spectrum of NO molecule

The NO molecule is an open shell molecule, which is critical to numerous biological processes including vasodilation. It can be added to the atmosphere by burning any kind of fuel. Since the abundance of nitrogen in the atmosphere is about 78%, the formation of NO molecules is probable due to the reaction of nitrogen and existing oxygen in the air under high-temperature conditions. NO participates in the ozone layer depletion, but of course, it has some industrial applications such as converting the ammonia into nitric acid as an intermediate. NO has an odd number of electrons and its two lower electronic states $^2\Pi_{\frac{1}{2}}$ and $^2\Pi_{\frac{3}{2}}$ have an energy difference of $\Delta\bar{\nu} = 123.139$ cm^{-1} in the vibrational ground state and $\Delta\bar{\nu} = 122.375$ cm^{-1} in $v = 3$ vibrational state. At room temperature the $^2\Pi_{\frac{3}{2}}$state has a relative intensity of about 0.56 with respect to the $^2\Pi_{\frac{1}{2}}$ state. Each state splits into two e and f sub-states of positive parity [63, 64]. This Λ-doubling splits

the energy transition into two lines with equal intensity. The splitting due to Λ-doubling depends strongly on the rotational quantum number J. For example the e and f splitting in the NO R(26) including 12 rotational lines centered at $\bar{\nu} = 1955.67$ cm^{-1} is shown in Table 4.2.

Line	$\bar{\nu}$(cm^{-1}) 1955.67 +	separation $\delta\bar{\nu}$ (cm^{-1})	Line intensity cm^{-1}/molecule·cm^{-2}
R(26.5e)	0.0004		1.55×10^{-22}
		2.2×10^{-5}	
R(26.5e)	0.0026		1.49×10^{-22}
		1.9×10^{-5}	
R(26.5e)	0.0045		1.44×10^{-22}
		3.96×10^{-4}	
R(26.5e)	0.0441		1.98×10^{-25}
		1.28×10^{-4}	
R(26.5e)	0.0569		1.98×10^{-25}
		4.15×10^{-4}	
R(26.5e)	0.0984		6.54×10^{-29}
		4.9×10^{-3}	
R(26.5f)	0.5898		1.98×10^{-25}
		1.2×10^{-5}	
R(26.5f)	0.5910		1.55×10^{-22}
		4×10^{-6}	
R(26.5f)	0.5914		1.49×10^{-22}
		7×10^{-6}	
R(26.5f)	0.5921		1.44×10^{-22}
		1.86×10^{-4}	
R(26.5f)	0.6107		6.54×10^{-29}
		5×10^{-3}	
R(26.5f)	0.6123		1.98×10^{-25}

Table 4.2: *The e and f sub-states for the NO molecule given in the HITRAN2003 database.*

4.2 Quantitative MIR absorption spectroscopy; *Lambert-Beer* law

The fundamental theory governing absorption spectroscopy in the absence of optical saturation is based on the well known Lambert-Beer law [65]

$$\frac{I(\bar{\nu})}{I_0(\bar{\nu})} = exp[-S_{n,m}\phi(\bar{\nu} - \bar{\nu}_0)P_t N_x L] \tag{4.13}$$

which is often used for quantitative measurements. It states that the transmission decays exponentially. In Equation (4.13), $I(\bar{\nu})$ and $I_0(\bar{\nu})$ are the through an absorbing medium at a particular frequency transmitted and initial (reference) intensities of a monochromatic laser radiation, respectively.

$S_{n,m}$ [cm^{-2} atm^{-1}] is the absorption transition linestrength of the ($|n\rangle \rightarrow |m\rangle$) transition,
$\phi(\bar{\nu} - \bar{\nu}_0)$ [cm] is the linshape function,
P_t [atm] is the total pressure in the medium,
N_x is the mole fraction of the absorbing species, and
L [cm] is the pathlength through which the radiation passes.

In practice the absorption is more frequently described in terms of the absorption coefficient $k(\nu)$, and the product $k(\nu)L$ is mostly defined as the *absorbance* or the *optical depth* $\tau(\nu)$ at frequency ν. It can be related to the Einstein probability coefficient $B_{n,m}$ as discussed in chapter 2. Therefore, one way to determine the $B_{n,m}$ coefficient is to measure the absorbance of a medium.

4.2.1 Linestrength of transition

The linestrength of the transition is a fundamental spectroscopic property of the absorption species. It depends on

1. the population in the lower quantum state which is governed by Boltzman population statistics, and
2. the probability of the transition which depends on the specific spectroscopic constants associated with the molecule's particular transition.

A given absorption line is characterized by its integrated linestrength S, in terms of the absorption cross-section $\sigma(\nu)$; $S_{n,m} = \int_0^\infty \sigma(\nu)d\nu$, which is independent on pressure, but not on temperature [66]. Consequently, the population on the lower quantum state and hence the linestrength is dependent of temperature and thus

$$S_{n,m}(T) = S_{n,m}(T_0)\frac{Q(T_0)}{Q(T)}\left(\frac{T_0}{T}\right)^{\eta}\frac{[1 - exp(-1.439\omega/T)]}{[1 - exp(-1.439\omega/T_0)]}exp\left[1.439E\left(\frac{1}{T_0} - \frac{1}{T}\right)\right] \tag{4.14}$$

where E is the lower energy level of the transition, ω is the applied laser frequency, and η is the exponent that depends on the type of molecule (generally $\eta = 0.5$ for diatomic molecules [67]). $Q(T)$ is the total *partition function* of the transition which describes how the energy is distributed throughout the medium of N molecules. It can be written as:

$$Q(T) = [1 - exp(-1.439\omega_{n,m}/T)]^{-1},$$

with $\omega_{n,m}$ acting as a transition frequency.

4.2.2 Spectral lineshape

The lineshape function $\phi(\bar{\nu} - \bar{\nu}_0)$ describes the effect of collisional and thermal processes on the broadening of the molecular transition frequency and hence the temperature- and pressure-dependent broadening mechanism of the fundamental linestrength. It reflects the relative variation in the spectral absorption coefficient with frequency. It is usually required that the integral of the lineshape function is normalized according to

$$\int_{-\infty}^{\infty} \phi(\bar{\nu} - \bar{\nu}_0) d\bar{\nu} = 1. \tag{4.15}$$

Therefore, the peak amplitude of the absorption signal decreases with increasing linewidth. Variations in linewidth are, therefore, of great importance for precise measurement of the concentration of molecular species. A typical lineshape function of an isolated line centered at $\bar{\nu}_0$ is shown in Figure 4.4. As can be seen from the figure, the spectral line is distributed around its central wavenumber $\bar{\nu}_0$ corresponding to a molecular transition. The width of the line $\Delta\bar{\nu}$ is defined by the full width at half maximum (FWHM). The spectral line does not have any arbitrary shape and it can be determined through a perfect knowledge of the transition energy. There are a variety of mechanisms that broaden the lineshape to a finite width. Some of those mechanisms contain significant information about the molecular species involved in the transition. Therefore, *broadening* of an absorption feature occurs due to the phenomena in the medium that perturb the transition energy or the way in which individual molecules interact with light.

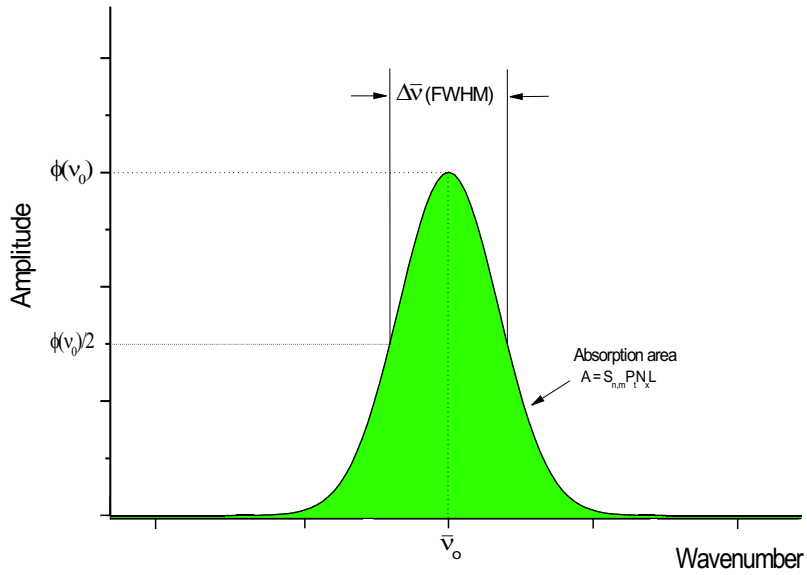

Figure 4.4: *Typical lineshape function and associated parameters.*

4.2.2.1 Natural broadening

As a consequence of the *Heisenberg* uncertainty principle

$$\Delta E \Delta t \sim \hbar$$

the energy level of an excited state of a molecule can never be determined precisely because its lifetime Δt is finite. For the ground state $\Delta t = \infty$ and hence its energy is exactly determined as $\Delta E = 0$. This uncertainty causes a broadening in the spectral lineshape and the line profile is broadened with a *natural* linewidth of

$$\Delta\bar{\nu} = \frac{1}{2\pi}\frac{c}{\Delta t}.$$

This effect leads to a Lorentzian profile function with

$$\phi(\bar{\nu} - \bar{\nu}_0) = \frac{1}{\pi}\frac{\gamma/4\pi}{(\bar{\nu} - \bar{\nu}_0)^2 + (\gamma/4\pi)^2}, \tag{4.16}$$

where the width γ is related to the spontaneous decay rates A_{kl} of the excited state $|k\rangle$ into all lower states $|l\rangle$ through $\gamma = \sum_l A_{kl}$. The decay rate constants A_{kl} result from the quantum mechanical treatment of the respective transition and can be found in standard tables and literature [68]. At the limit $A_{kl} \to 0$ the transition intensity is proportional to $\pi\delta(\bar{\nu} - \bar{\nu}_0)$, which means that the energy of the ground state is definitely determined. γ is also known as damping constant when a classical harmonic oscillator model is used for the oscillating molecule as shown in the chapter 2. However, if the lower level $|l\rangle$ of the transition $|k\rangle \to |l\rangle$ is a ground state with an infinite lifetime the lower state is also broadened and the resultant lineshape is a convolution of two Lorentzian functions due to both (1) transition and (2) the broadened ground state. The width of the resultant Lorentzian lineshape function is the sum of the single widths as [19]:

$$\Delta\bar{\nu}_{total} = \Delta\bar{\nu}_{k\to l} + \Delta\bar{\nu}_l$$

4.2.2.2 Collisional broadening

A molecule is not completely isolated and its collisions with partner molecules broaden further the linewidth of an absorption feature by shortening the lifetime of the excited states. Therefore, if the absorbing molecule responsible for an absorption line is suffering frequent collisions with other molecules, its energy levels will be distorted. This broadening mechanism is called *collisional* or *pressure* broadening. The line can broaden even further if the molecule undergoes a collision with other particles, through increasing the pressure of the medium. The mechanism of this effect depends on the frequency at which such collisions occur. If the collisions are random then the probability that the molecule will survive without collision for a time t is proportional to e^{-t/τ_c}, where τ_c is the mean-time between collisions. If the molecule is moving at speed v, the volume swept out per second is

σv, where σ is the collision cross-section. The number of collisions per second (i.e. collision rate) is then

$$R_c = n\sigma v,$$

where n is the density of molecules. The collision rate R_c can be related to some other parameters via [69]

$$R_c = 3.4 \times 10^{10} \frac{D^2 P}{\sqrt{MT}},$$

where P is the pressure of the medium, D is the diameter of the molecule, M is the molecular mass, and T is the absolute temperature of the medium. As could be expected, R_c can be reduced by reduction of the pressure. The effect of collisions is therefore to broaden, homogeneously, the absorption line to a Lorentzian profile as

$$\phi_C(\bar{\nu} - \bar{\nu}_0) = \frac{1}{\pi} \frac{\Gamma/4\pi}{(\bar{\nu} - \bar{\nu}_0)^2 + (\Gamma/4\pi)^2}. \tag{4.17}$$

Γ is the effective width and is given by

$$\Gamma = \gamma + 2\nu_{col.}$$

where $\nu_{col.}$ is the collision frequency related to the collision rate by $\nu_{col.} = R_c^{-1}$. The quantity $\frac{\Gamma}{4\pi}$ is the Lorentzian FWHM denoted by $\Delta\bar{\nu}_c$. Therefore, Equation (4.17) can be written as

$$\phi_C(\bar{\nu} - \bar{\nu}_0) = \frac{1}{\pi} \frac{\Delta\bar{\nu}_C}{(\bar{\nu} - \bar{\nu}_0)^2 + (\Delta\bar{\nu}_C)^2}. \tag{4.18}$$

A typical Lorentzian lineshape of CO and NO molecules is given in Figure 4.5. The collisional width $\Delta\bar{\nu}_C$ of an absorption line is directly proportional to the pressure of the medium containing the molecular species i whose lineshape is being studied. Thus

$$\Delta\bar{\nu}_C = P_t \sum_j c_j \gamma_{ij} \tag{4.19}$$

where γ_{ij} [cm^{-1}/atm] is the process-dependent broadening coefficient, and c_j is the density of perturber molecules that interact with the molecule i. For instance, γ_{CO-CO} is the broadening coefficient for CO-CO collisions (*self-broadening*), and γ_{CO-Air} is the broadening of CO species due to their interaction with air (*air-broadening*). Values of γ_{ij} may be determined experimentally and are investigated for specific collision partners. The broadening coefficient γ_{ij} is a function of temperature and thus can be written as [70]

$$\gamma(T) = \gamma(T_0) \left(\frac{T_0}{T}\right)^{\beta},$$

where T_0 is the reference temperature, $\gamma(T_0)$ is the broadening coefficient at the reference temperature, and β is the temperature exponent which ranges typically between 0.5 (according to the impact theory) and 0.75 (according to the Anderson-Tsao-Curnutte theory) [71].

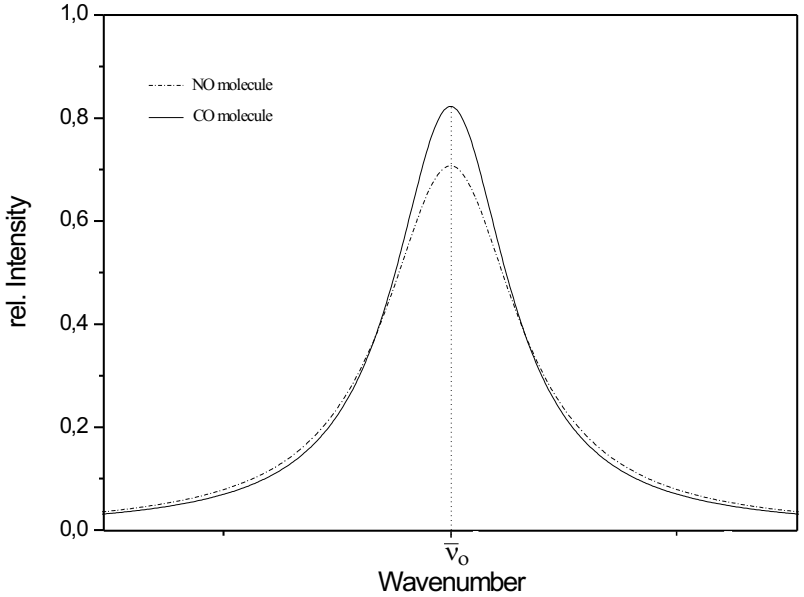

Figure 4.5: *Typical collisional broadening of CO and NO molecules assuming appropriate air-broadening coefficients for both molecules.*

4.2.2.3 Doppler broadening

The thermal motion of absorbing molecules leads to small variations in the absorption frequency. In principle, when a molecule has a velocity component in some direction as the propagation of a light beam, there will be a shift in the frequency at which it will absorb a photon. This shift is called *Doppler shift*. At thermal equilibrium, the molecules of a gas follow a Maxwellian velocity distribution. All molecules in the medium can be classified to separate groups with their own velocity and their own Doppler shift. This distributed velocity leads directly to a lineshape function with a Gaussian form as

$$\phi_D(\bar{\nu} - \bar{\nu}_0) = \frac{1}{\Delta\bar{\nu}_D}\left[\frac{ln2}{\pi}\right]^{1/2} exp\left[-ln2\left(\frac{\bar{\nu} - \bar{\nu}_0}{\Delta\bar{\nu}_D}\right)^2\right] \tag{4.20}$$

where $\Delta\bar{\nu}_D$ is the Doppler width at HWHM and is given by

$$\Delta\bar{\nu}_D = \frac{\bar{\nu}_0}{c}\sqrt{\frac{2k_BTLn2}{m}} \tag{4.21}$$

where m is the molecular mass. It is more convenient to write the Doppler width $\Delta\bar{\nu}_D$ in the form of molecular mass number M[grams/mole] as

$$\Delta\bar{\nu}_D = 7.16 \times 10^{-7}\bar{\nu}_0\sqrt{\frac{T}{M}} \quad \text{(at FWHM)} \tag{4.22}$$

Therefore, the transition line of any molecular species can be inhomogeneously broadened at high temperature conditions. This broadening mechanism is also more pronounced for

lighter molecules. Figure 4.6 shows the Doppler broadening for two typical absorption lines of CO and NO molecules. The CO molecule is more sensitive to the thermal broadening effect than the NO molecule due to the former's comparatively small molecular mass. In comparison, the Gaussian lineshape has a peak value that is about 50% higher than the Lorentzian, but it drops off much faster in the wings. Since the pressure of a gaseous medium determines the linewidth of the Lorentzian linshape, it is possible to obtain some useful information about the medium through looking at the extreme line wings, even if the Doppler width is much larger. However, at low pressure levels the Lorentzian linewidth is much smaller than the Gaussian one and can then be ignored. This can be used to measure the natural linewidth of the MIR radiation when it is absorbed through passing a low pressure medium at room temperature.

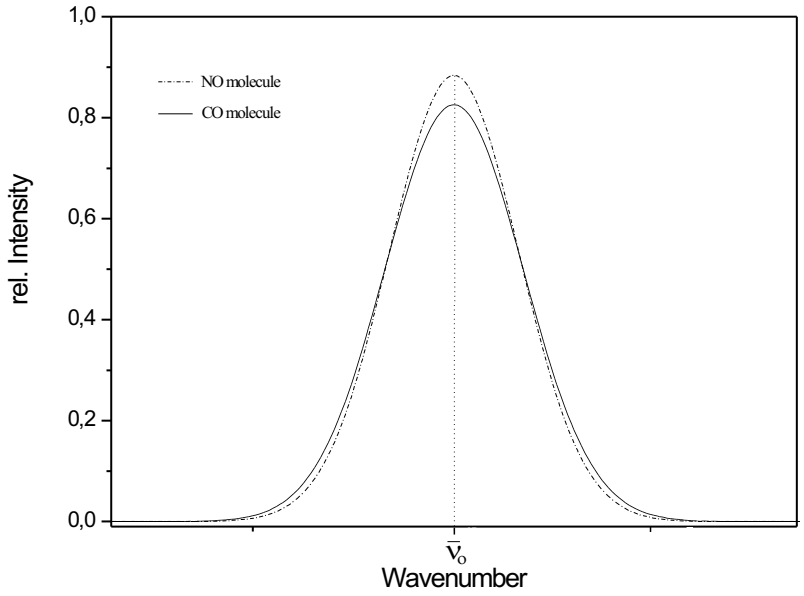

Figure 4.6: *Typical Doppler broadening of CO and NO molecules at room temperature.*

4.2.3 Voigt profile

If two types of line broadening mechanism are independent, the resultant line profile can be obtained by convoluting the two profiles. When both Doppler and collisional broadening are significant and neither can be neglected, it can be assumed that each group of molecules with their own velocity class is collisionally broadened. The convolution of Doppler and collisional broadening is called *Voigt* profile and is mathematically written as:

$$\begin{aligned} \phi_V(\bar{\nu}-\bar{\nu}_0) &= \phi_C(\bar{\nu}-\bar{\nu}_0) \star \phi_D(\bar{\nu}-\bar{\nu}_0) \\ &= \int_{-\infty}^{+\infty} \phi_C(\bar{\nu}'-\bar{\nu}_0)\phi_D(\bar{\nu}'-\bar{\nu})d\bar{\nu}'. \end{aligned} \tag{4.23}$$

The above equation can be rewritten using Equations (4.18) and (4.20) as:

$$\begin{aligned}\phi_V(\bar{\nu}-\bar{\nu}_0) &= \frac{a}{\pi}\sqrt{\frac{Ln2}{\pi}}\frac{1}{\Delta\bar{\nu}_D}\int_{-\infty}^{+\infty}\frac{exp(-y^2)dy}{a^2+(w-y)^2} \\ &= \phi_D(\bar{\nu}-\bar{\nu}_0)|_{\bar{\nu}=\bar{\nu}_0}V(a,w)\end{aligned} \tag{4.24}$$

where

$$a = \frac{\Delta\bar{\nu}_C}{\Delta\bar{\nu}_D}\sqrt{ln2}$$

is the damping constant, and

$$w = \frac{\bar{\nu}-\bar{\nu}_0}{\Delta\bar{\nu}_D}\sqrt{ln2}$$

is a measure of the distance from the line center. $V(a,w)$ is the Voigt function. At the linecenter where $w = 0$, $V(a,w)$ reduces to $V(a,0) = exp(a^2)erfc(a)$ [66]. The Voigt parameter a, indicates the relative significance of Doppler and pressure broadening. An important feature of the Voigt function is that the wings are almost determined by the Lorentzian component even at low pressures where the factor a is small. Therefore, the central part of the Voigt profile and its FWHM are determined by the Gaussian component and the wings by the Lorentzian component. The halfwidth $\Delta\bar{\nu}_V$ of the Voigt profile is more complicated to be solved analytically, instead it can be calculated using standard mathematical routines. An approximation for $\Delta\bar{\nu}_V$ can be given as [72]:

$$\Delta\bar{\nu}_V = 0.5346\Delta\bar{\nu}_C + \sqrt{0.2166\Delta\bar{\nu}_C^2 + \Delta\bar{\nu}_D^2} \quad . \tag{4.25}$$

A typical Voigt profile $\phi_V(\bar{\nu}-\bar{\nu}_0)$ for CO and NO molecules is given in Figure 4.7 which can be compared with the Lorentzain and Doppler profiles as shown previously in figures 4.5 and 4.6, respectively. Some useful information about the medium may be obtained through the Voigt linewidth $\Delta\bar{\nu}_V$.

The concentration of the species j in the medium c_j can be easily calculated through:

$$c_j = \frac{p_j}{p_t}, \tag{4.26}$$

where p_j is the partial pressure of molecule j in the medium. If the total number of molecules j in the volume V is n, then

$$\begin{aligned}p_j &= \frac{nk_BT}{V} \\ &= N_jk_BT\end{aligned}$$

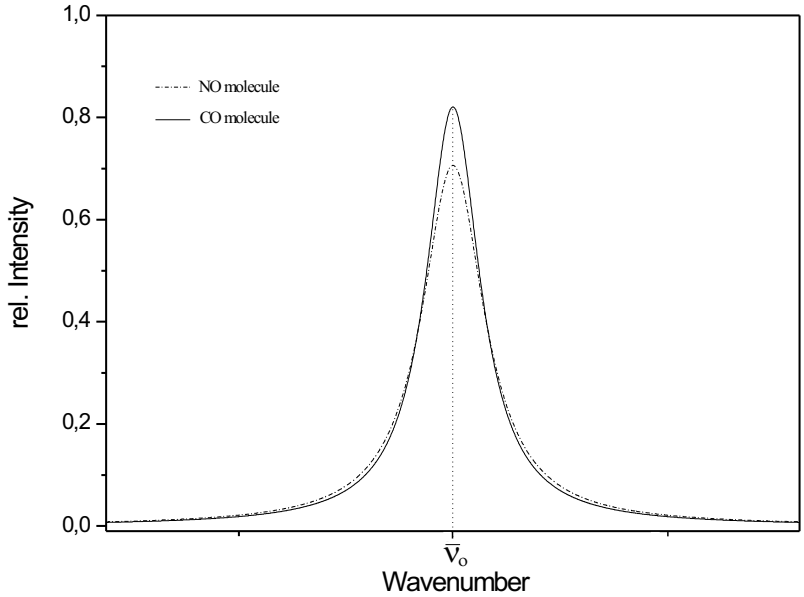

Figure 4.7: *Typical Voigt broadening of CO and NO molecules at room-temperature and assuming appropriate air-broadening coefficient for both molecules.*

and therefore, the partial pressure p_j can be calculated indirectly through the parameters given by Equation (4.13) as

$$p_j = \frac{\tau(\bar{\nu})|_{\bar{\nu}=\bar{\nu}_0} k_B T}{S_{n,m}(T)\phi_V(\bar{\nu}-\bar{\nu}_0)|_{\bar{\nu}=\bar{\nu}_0} L} \tag{4.27}$$

where $\tau(\bar{\nu})$ is the absorbance at the linecenter.

5 Efficient MIR-DFG laser source for quantitative spectroscopy

5.1 Laser source for DFG conversion

Numerous DFG based MIR laser sources have been designed and used for different applications. Pine in 1974 combined an Ar^+ laser and a dye-laser and a bulk $LiNbO_3$ crystal as a first demonstration of DFG down-conversion to obtain cw MIR-DFG radiation tunable from 2.2 to ~ 4 μm. The output power of such DFG laser was about $P_{out} = 0.5\mu$W. In 1973 Bethea demonstrated pulsed DFG at 5.2 μm by mixing of two wavelengths emitted simultaneously from a pulsed Nd:YAG laser in an $AgGaS_2$ nonlinear crystal. The generated output power is not reported. Soon after nearly all kind of laser sources from diode-lasers and semiconductor lasers to most recently fiber lasers have been used to produce a wide range of MIR radiation wavelengths through the DFG mixing process. Specially, during the last decade, F. K. Tittel's group at the Rice University has demonstrated a wide application range of absorption spectroscopy based on DFG laser sources in the MIR spectral range. They have also reported the first cw application of MIR DFG radiation in $AgGaS_2$ in 1992 [48]. In Table 5.1 some recent data of the sources involved in a DFG interaction, corresponding crystals, and some available output parameters in both cw and pulsed regime are listed. Due to the excellent spatial characteristics of diode-lasers and their narrow linewidth, which is sufficient for high resolution absorption spectroscopy, and their room temperature operation new development of narrow and compact DFG laser sources for various application are in progress.

5.1.1 Diode-lasers as efficient DFG pump sorces

The distinct feature of the diode-lasers is their extremely small size compared to other lasers. The active area is a p-n junction that is made of doped p-type and n-type regions in a single crystal of a semiconductor[1]. The p-n junction of the early semiconductor lasers was made from a single material and was known as *homojunction*. Contrary the recent ones are made from two different kinds of semiconductors and are called *heterojunctions*. When a material with low bandgap energy and smaller refractive index such as AlGaAs surrounds another material with higher bandgap energy and bigger refractive index such as GaAs, the light and carriers are mostly concentrated in the GaAs. Thus if the hetrojunction is made of those materials, a strong interaction between the light and carriers can be obtained and consequently the threshold of laser oscillation is appreciably reduced. Such a p-n junction is called *double* hetrojunction, abbreviated to DH structure. The typical thickness of the

[1] In forward bias (p-side is positive) electrons are injected across the p-n junction into the semiconductor.

active layer is 0.1 to 2 μm and the spatial mode behavior of the laser radiation is similar to that of microwaves in a waveguide of rectangular cross-section. When an electron meets a positive hole, they combine together, emitting a photon of energy nearly equal to the bandgap energy. The recombination of an electron and a hole with the emission of a photon is called a *direct transition*. The structure of a simple semiconductor diode-laser is shown in Figure 5.1. The two parallel facets of a direct transition semiconductor are perpendicular to the plane of the p-n junction to form a resonator. The end facets may be optically polished and coated.

Nonlinear crystal	Generated wavelength (μm)	Sources of interacting radiation radiation
$AgGaS_2$	from 4.6 to 12 and	
	from 5 to 11	dye-laser and Q-switched ruby laser [49, 55]
	from 4 to 9 and	
	from 6.5 to 8.5	two single frequency dye/Ti:Sapphire laser [73, 74]
	from 9 to 11	two external-cavity diode-lasers [75]
	from 4.8 to 6.5	dye laser and Ti:Sapphire laser [76]
	near 4.3	diode-laser and Ti:Sapphire laser [77, 78]
	from 5.5 to 18.3	two dye lasers [79]
	from 5 to 12	signal and idler output of OPO lasers [80, 81]
	centered at 5	dye laser and NIR diode-lasers [82]
	from 6.8 to 12.5	two SDL diode-lasers [83, 84]
	around 5	two diode-lasers [85, 86]
$LiNbO_3$		
and PPLN	from 3.3 to 3.5	Er-amplified diode-laser and α-DFB diode-laser [87]
	about 3	Yb fiber laser and DFB diode-laser [88]
	from 4 to 4.5	Nd:YAG laser and tapered amplified diode laser [89]
	from 3.16 to 3.67	Nd:YAG ring laser and external-cavity diode-laser(ECDL) [90]
	at 3.3	Yb amplified Nd:YAG laser and Er/Yb amplified diode-laser [91]
$AgGaSe_2$		
	at 8.7	Er/Yb fiber amplifier and Nd:YAG laser [92]
	from 5 to 18	signal and idler output of OPO laser [93]
GaSe		
	9 to 18	broad spectrum and mode-locked Ti:Sapphire laser [94]
	8 to 19	two Ar^+ laser-pumped Ti:Sapphire lasers [95]

Table 5.1: *List of data on the DFG radiation parameters.*

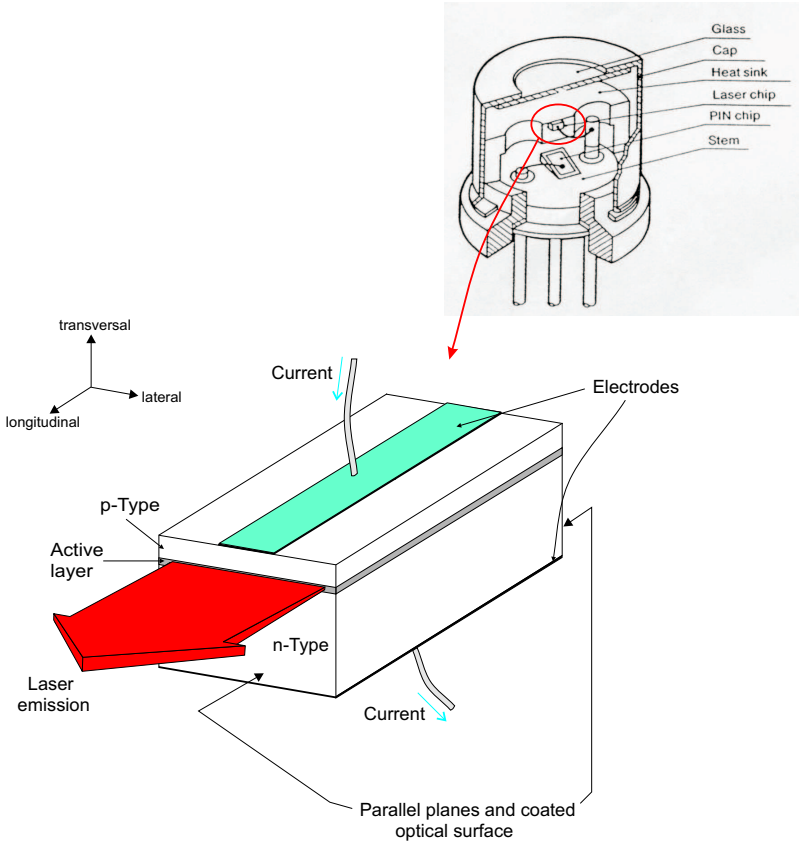

Figure 5.1: *A schematic of a typical diode-laser.*

The output wavelength of a diode-laser depends on the used material. For example, if a p-n junction is made of a mixed crystal, such as $In_xGa_{1-x}As$ or from different materials such as InAs and GaAs, the diode-laser will lase at a wavelength tunable between 0.9 and 3.1 μm depending on the mixing ratio x. The tuning range of various tertiary semiconductors is given in Figure 5.2.

5.1.1.1 Spatial characteristics of a semiconductor diode-laser

Unlike to gas lasers the directivity of the output from a diode-laser is not collimated, separating out typically with angles of 5° to 30°; this is because the ligth is emitted from a small area whose sides have dimensions of about 2 to 20 μm. Figure 5.3 shows the beam divergence of a typical GaAs diode-laser. The emission from a diode-laser tends to be an elliptical beam with a full angle divergence in the directions perpendicular and parallel to the junction, denoted by $\theta_\perp$ and $\theta_\parallel$, respectively. This asymmetry in those directions leads to the non-Gaussian beam profile and hence a nonuniform energy distribution of the laser beam cross section is formed. Almost all applications require a uniform spatial distribution

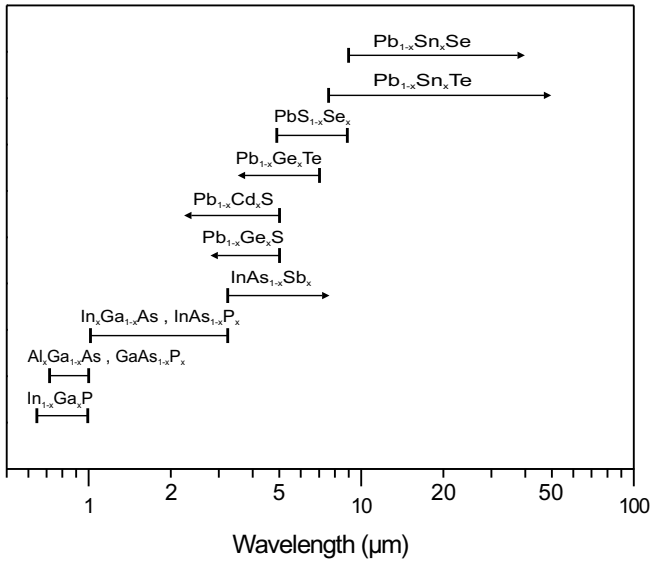

Figure 5.2: *Wavelength range of the output of various semiconductor lasers [96].*

of laser irradiance produced by a Gaussian or TEM_{00} mode[2]. For the DFG-process, where beams with perpendicular polarization have to spatially overlap, the conversion of the elliptical beam profile is essential to maximize the conversion efficiency.

5.1.1.2 Diode-laser performance characteristics

Several key characteristics of lasers determine their usefulness in a given application such as:

- center wavelength,
- spectral width,
- emission pattern,
- output power,
- speed to meet the bandwidth limits of the system [3], and
- linearity.

[2] TEM_{00} is termed the uniphase or pure Gaussian mode, because it is the only transverse mode in which all light is in one phase at any given time.

[3] The speed is given according to a source's rise or fall time, the time required to go from 10% to 90% of the peak power.

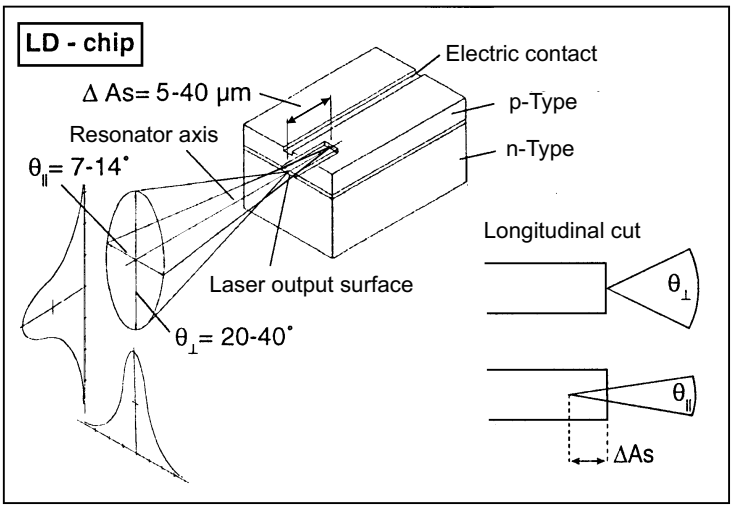

Figure 5.3: *A typical beam divergence of a GaAs diode-laser [97].*

The linearity represents the degree to which the optical output is directly proportional to the electrical current input. Diode-lasers are temperature sensitive; the lasing threshold changes the temperature. As the operating temperature changes, several effects can occur. First, the threshold current changes according to [98]

$$I_{threshold} = I_0 e^{T/T_0}. \tag{5.1}$$

Second, the *slope efficiency* which is the ratio of output power and drive current changes. Most lasers show a drop in slope efficiency as the temperature increases. Thus the lasers require a method of stabilizing the threshold to achieve maximum performance. Often a photodiode is used to monitor the light output on the rare facet of the laser. The current from the photodiode changes with variations in light output and provides a feedback to adjust the laser drive current.

In absorption spectroscopy the linewidth of the laser source plays an important role. A typical spectral linewidth of a diode-laser is below 10 MHz. For in-situ measurements near atmospheric pressure, the FWHM of spectral lines of molecular species are generally in the order of 0.15 cm^{-1} (4.5 GHz) [99]. Therefore, diode-lasers can generally be considered monochromatic with respect to the absorption lineshape.

5.1.2 Experimental setup for MIR DFG laser spectrometer

A schematic experimental setup of the MIR DFG laser system is shown in Figure 5.4.

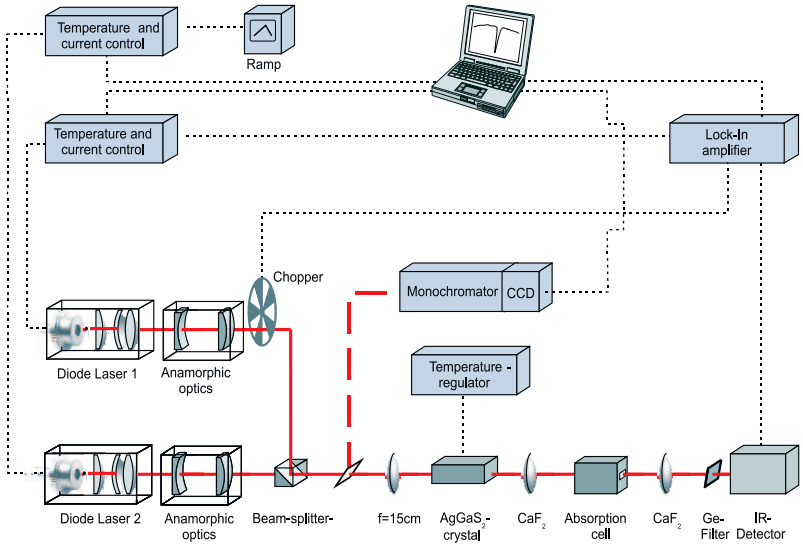

Figure 5.4: *Experimental setup for the MIR DFG spectrometer.*

The signal and pump sources are generated by two cw single mode diode-lasers. The significance of the above MIR DFG laser elements are characterized as follow:

Laser 1 :	cw single mode diode-laser Toshiba TOLD9150
specifications :	$\lambda_p = 680.9nm$, $P_{max.} = 30mW$, $I_o = 95mA$,
	$\theta_{\parallel} = 8.5°$, $\theta_{\perp} = 18°$, tuning range : $\sim$ 3 nm,
	measured slop efficiency : 0.31 $\frac{mW}{mA}$,
	measured maximum mode hop free tuning range : 0.075 nm.
Laser 2 :	cw single mode diode-laser Sharp LT024MDO
specifications :	$\lambda_p = 790nm$, $P_{max.} = 20mW$, $I_o = 73.5mA$,
	$\theta_{\parallel} = 8.6°$, $\theta_{\perp} = 26.5°$, tuning range : $\sim$ 3 nm,
	measured slop efficiency : 0.11 $\frac{mW}{mA}$,
	measured maximum mode hop free tuning range : 0.33 nm.

Collimation optics (SK 9650, Schäfter & Kirchhoff) and anamorphic optics (5AN-3-A-05,Schäfter & Kirchhoff) [100] are applied to transform the elliptical beam profiles of the two diode-lasers into nearly Gaussian beam shapes. Furthermore, the temperature of both lasers is controlled and stabilized by a Peltier element and the current is driven and stabilized by a diode-laser driver electronics constructed in our research group. The typical mode behavior of both diode-lasers is shown in Figure 5.5. As can be seen mode jumping

is observed in some regions which is quite normal for diode-lasers.

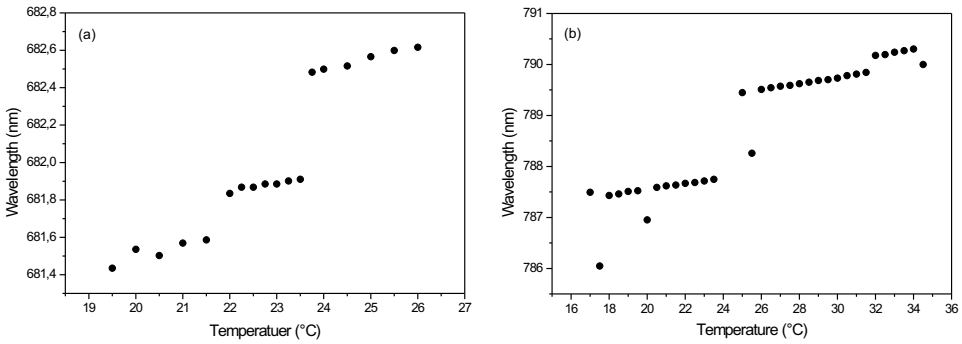

Figure 5.5: *A Typical mode behavior of both diode-laser (a) laser 1 and (b) laser 2 used as pump and signal sources in the MIR DFG spectrometer.*

Nonlinear crystal :	Silver Thiogallate $AgGaS_2$ nonlinear optical crystal,
specifications :	length : 30 mm, aperture area : 4×4 mm^2, cut for 90 type I phase-matching ($\theta = 90°, \phi = 45°$),

The antireflection coating of the crystal is specified in Table 5.2. It is chosen with regard to the pump, signal and idler beams. In order to precisely change and stabilize the tem-

AR-coating	face 1: 650-1000 nm
	face 2: 4000-6000 nm

Table 5.2: *Antireflection coating of the applied $AgGaS_2$ crystal.*

perature of the crystal necessary for type I phase-matching, the crystal is placed into a temperature controlled device as shown in Figure 5.6. Thus the temperature regulation and stabilization of the crystal within an accuracy of ±0.1°C is possible. At given pump and signal wavelengths the temperature of the crystal is changed to obtain the phase-matching temperature. Figure 5.7 indicates the dependency of the DFG intensity on the temperature of the crystal which can be compared with Figure 3.5. As expected, the intensity of the DFG radiation strongly depends on the coherence factor given by Equation (3.20). The slight asymmetry observed in Figure 5.7 is due to temperature gradients at both ends of the crystal and/or due to the interaction effect of focused Gaussian beams. Applying Equation (3.28) a temperature bandwidth of $\Delta T_{HWHM} = 2.55$°C is obtained. This small temperature bandwidth of the crystal would limit the useful DFG bandwidth to about 3.6 cm^{-1} as measured by a Fabry-Perot etalon.

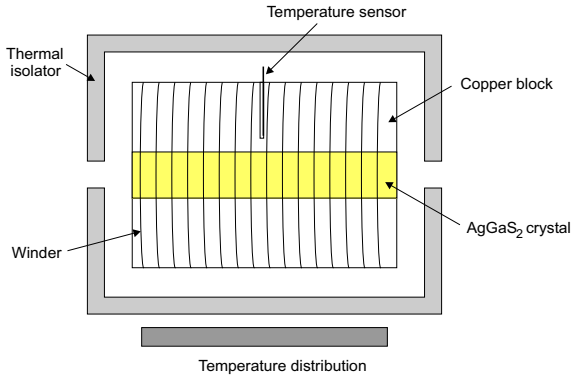

Figure 5.6: *The illustration of crystal's temperature controller.*

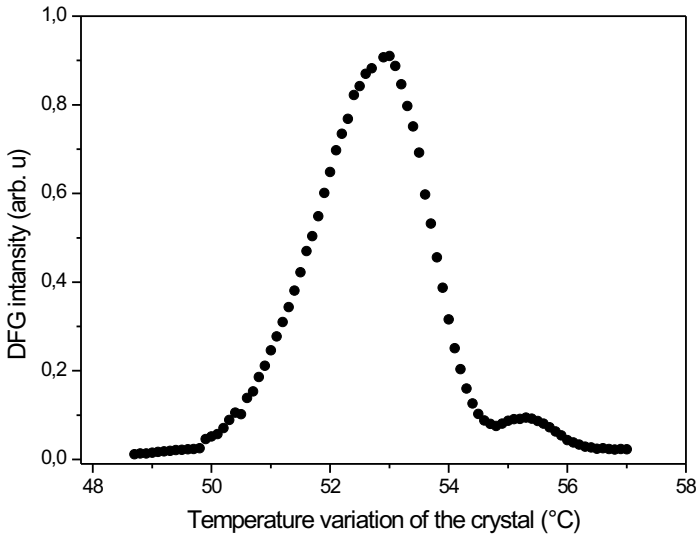

Figure 5.7: *Dependency of the DFG intensity on the variation of the crystal temperature.*

IR-detector :	Thermoelectrically cooled detector DoroTEK PCI-2TE,
specifications :	$D^* = 2.5 \times 10^{10} cmHz^{1/2}W$, $\lambda_{opt} = 5\mu m$
	active area = 1 mm^2, window : BaF_2
	or
	N_2-cooled InSb-detector, Polytec R-1703-IS, $D^* = 3.45 \times 10^{11} cmHz^{1/2}W$,
	$\lambda_{opt} = 5\mu m$, window : CaF_2

The spectral detectivity D^* is independent of the detection area of the detector and is hence sometimes known as a normalized detectivity. Generally, detectors are divided into [101, 102]

1. thermal detectors and
2. photodetectors.

Thermal detectors such as thermopiles and bolometers are non-selective in wavelength respond and the radiant energy is measured by the heating effect of light which raises the temperature of the irradiated material. The maximum time response of the thermal detectors depends on both the thermal conductance and the heat capacity of the sensitive element. However, the materials with either high thermal conductance or low heat capacity are very fragile and any contact to liquids must be avoided.

Contrary, photodetectors such as photodiodes and photoconductors are selective in wavelength response and the radiant energy is measured by the induced voltage (photovoltaic mode) or current (photoconductive mode) due to the excitation which is caused by the incident light by creating electron-hole pairs in the photosensitive area. The time response of the photoconductive detectors is faster than that of the photovoltaic ones because of the low transit time of the charge carriers to their respective electrodes. However, the main drawback of the photodetectors is the cryogenic or even liquid-nitrogen cooling which makes them expensive and limit their applicability for room temperature applications.

The performance parameters of photoconductor detectors are

- **spectral response** (the peak wavelength response of the detector),
- **Quantum efficiency** (a measure of how many photoelectrons are produced for every photon on the photosensitive surface),
- **responsivity** (the magnitude of the electrical signal output from a photodetector in response to a particular light power),
- **noise equivalent power** (NEP) (the minimum detectable signal by the detector), and

- **response time** (a measure of how long it takes a detector to respond to a change in light power).

The spectral response of the InSb-detector is shown in Figure 5.8. The InSb-detector is classified in the quantum detector (photon in, electron out) group as a photovoltaic detector.

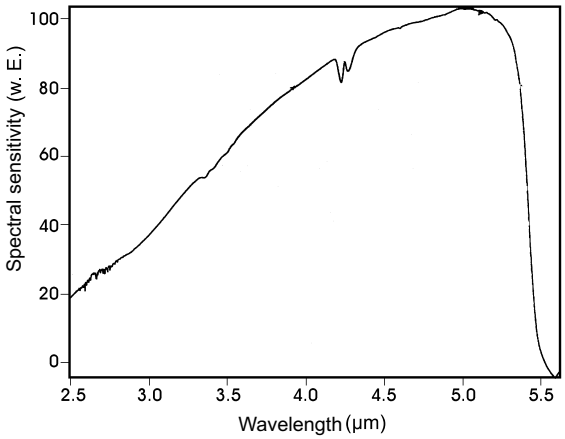

Figure 5.8: *The spectral response of InSb-detector Polytec R-1703-IS [103].*

Some typical specifications of this detector are given in Table 5.3.

	Polytec R-1703-IS
semiconductor material	InSb
working temperature	77 K
response time	$< 10ns$
active area (mm^2)	1
window material	CaF_2
opening angle	60°
SNR at 1 KHz	8545
sensitivity	5.277 $\frac{nW}{V}$

Table 5.3: *Some specifications of InSb photovoltaic detector [45]*

In principle, the voltage variation across the junction of a photodiode can be used as a measure of the incident light. Therefore, one can assume that the detector behaves as a capacitor that is discharged by the infrared photons. Generally, detectors cannot respond to the rapidly varying optical frequency. The quantity measured experimentally is the time-averaged field flux, where the average is over several optical cycles. The quantity of interest is then the optical intensity, which is related to the field amplitude. In the

case of the InSb-detector, the sensitive element is the voltage caused by the charge carriers.

The SNR is an important characteristic of any spectroscopic system. In the infrared region both the detector and background noise are important. The detector noise comes from the fluctuations in the dark current and it has a thermal origin. This thermal noise can be reduced by cooling the detector. The background radiation noise can be reduced by shifting the wavelength of the radiation under investigation below 1 μm. However, in the MIR spectral region centered at 5 μm where the detection of CO and NO molecules are of great interest the background noise cannot be ignored.

Collimation lens : After the $AgGaS_2$ nonlinear crystal the MIR DFG laser radiation is collimated by a calcium fluoride (CaF_2) lens with a focal length of $f = 5$cm. CaF_2 is a chemically and physically stable crystal with excellent water resistance, chemical resistance, and heat resistance characteristics, and possesses a wide transparency range from the UV to the FIR region of the spectrum. An alternative transparent material for the infrared region is Zinc Selenide (ZnSe). Having a very low absorption of energy ZnSe is useful for optical components for high power windows and multispectral applications. However, in terms of a low loss for the MIR DFG laser CaF_2 is preferable. The spectral transmission of both CaF_2 and ZnSe are shown in Figure 5.9.

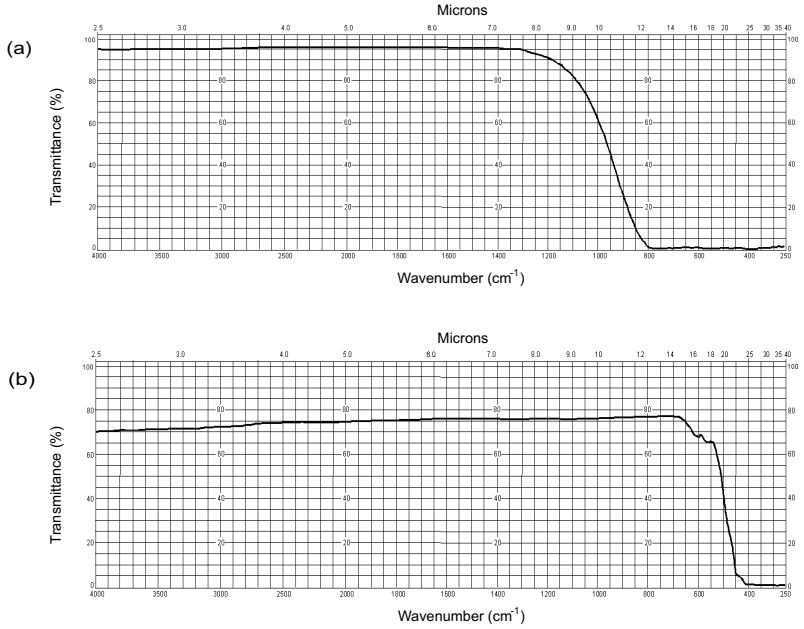

Figure 5.9: *The spectral transmission of (a) CaF_2 and (b) ZnSe [104].*

Germanium filter : A germanium (Ge) plate ($d = 1$ mm and 60% transmission) in front of the IR-detector is used as a cut-off filter for wavelengths $\lambda < 2$ μm. The spectral response of the Ge cut-off filter is shown in Figure 5.10.

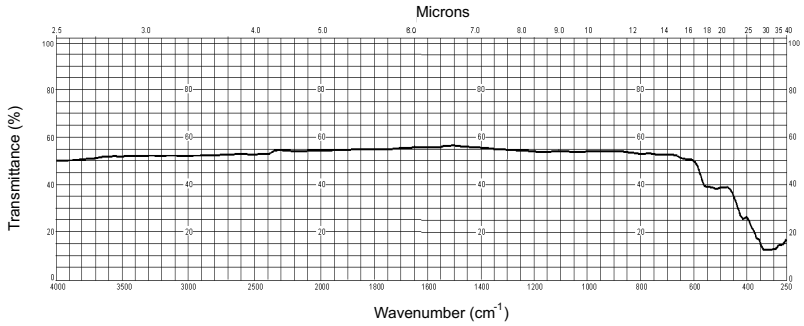

Figure 5.10: *The spectral transmission of a germanium plate used as a cut-off filter in the front of the detector [104].*

Lock-in amplifier : The low-power output DFG signal is directly recorded by a lock-in amplifier (EG&G 5210) while one of the diode-laser beams is chopped. To reduce the noise and make AC amplification possible, it is general practice to chop the light signal at some frequency and use a phase-sensitive amplifier of restricted bandwidth Δf. A lock-in amplifier, provides a DC output directly proportional to the input AC signal under investigation. The central part of a typical lock-in amplifier is a phase sensitive detector (PSD) which is known as *demodulator*. It converts the AC input to a DC component. The DC component in turn is passed through a low pass filter in order to be isolated from the noise components. Obtaining such conversion requires that the analytical signal is modulated at some *reference frequency*. This reference signal ensures that the instrument will trace any changes in the frequency of the input signal since the reference circuit is locked to the input. This tracing ability allows extremely small bandwidths to be defined for the purpose of SNR improvement and can provide an effective Q value for the lock-in amplifier. Therefore, only the components of the input signal at the reference frequency is amplified and all other frequencies will be blocked[4]. However, the noise at the input of the lock-in amplifier appears at the output as random AC fluctuation and can only be separated from a DC signal in the input when :

1. the reference signal amplitude is fixed at a certain value, and
2. the reference phase is adjusted with respect to the phase of the input signal.

A schematic diagram of a lock-in amplifier in given in Figure 5.11.

Analytically, at the PSD, an input signal $V_s \sin(\omega_s t + \theta_s)$ and the lock-in reference signal $V_r \sin(\omega_r t + \theta_r)$ are multiplied together to form a PSD signal at V_{PSD} as [105]

$$V_{PSD} = \frac{1}{2} V_s V_r \cos[(\omega_s - \omega_r)t + (\theta_r - \theta_s)] - \frac{1}{2} V_s V_r \cos[(\omega_s + \omega_r)t + (\theta_r + \theta_s)] \qquad (5.2)$$

[4]Conventional electronics such as AC voltmeter can not recognize the signal and the noise and thus produce errors.

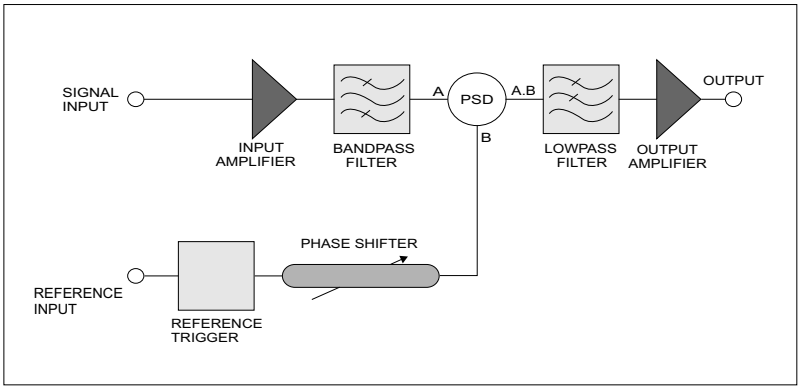

Figure 5.11: *A schematic diagram of a typical lock-in amplifier.*

The PSD output consist then of two AC signals, one at the difference frequency $\omega_s - \omega_r$ and the other at sum frequency $\omega_s + \omega_r$. When PSD is coupled with a low pass filter only the signals whose frequencies are very close to the reference frequency, i. e. $\omega_s \simeq \omega_r$ are passed and hence the difference frequency component of the PSD output is a DC signal as

$$V_{PSD} = \frac{1}{2} V_s V_r \cos(\theta_r - \theta_s). \tag{5.3}$$

As can be seen from the last expression the phase between input and reference signals should not be changed with time. Otherwise V_{PSD} will not be a DC signal. On the other hand, the lock-in reference signal needs to be synchronized with the input signal reference provided through the *chopping*[5] of the input signal, otherwise the average DC level of the PSD output is zero. This synchronization is done by a phase-locked-loop (PLL) circuit. The choice of the chopping frequency f is limited and it is determined by the response time of the detector τ_d so that [19]

$$\frac{1}{f} > \tau_d.$$

5.1.3 DFG output power scaling and conversion efficiency

The DFG output power can be measured using the lock-in amplifier output. With regard to the sensitivity of the InSb-detector given in Table 5.3 and including the reflection loss of the germanium plate in front of the detector which is about 45%, the measured DFG power is then

$$P_{DFG} = 3V \times 5.277 \frac{nW}{V} \times 0.55^{-1} = 28.78nW$$

and the corresponding conversion efficiency is

$$\eta = \frac{P_{DFG}}{P_p P_s L} \cong 0.06 \ \ mWW^{-2}cm^{-1}.$$

[5]The principle of chopping is to modulate the incident radiation at a fixed frequency and fed it into the lock-in amplifier at the output of the detector.

For the calculation of the conversion efficiency, the power incident as pump and signal laser beams is measured to be $P_p = 16$ mW and $P_s = 10$ mW, respectively.

5.2 Spectroscopic results

The performance of the described MIR DFG spectrometer is shown as single rotational lines of the CO molecule are probed by absorption spectroscopy. MIR DFG laser radiation scans are obtained by fixing the pump wavelength at $\lambda_p = 680.24$ nm and scanning the signal diode-laser around its center wavelength $\lambda_s = 790.80$ nm at $T_c = (27.9 \pm 0.1)°C$ at the crystal phase-matching temperature. Figure 5.12 shows the Voigt profile of the (1-0) CO P(21) rotational line at $\bar{\nu}_0 = 2055.4$ cm^{-1} with the linestrength of 2.5×10^{-20} cm^{-1}/(molecule $\cdot$ cm^{-2}) according to the HITRAN 2003 database [106].

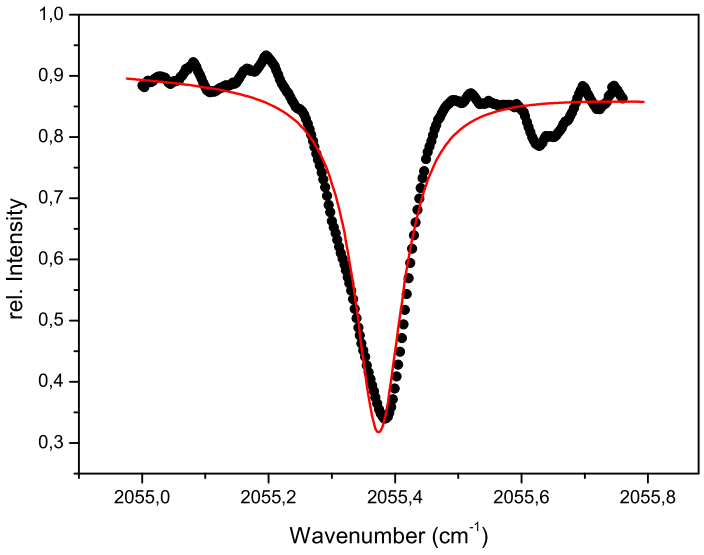

Figure 5.12: *Absorption spectra of the P(21) rotational line of the CO molecule at 2055.4 cm^{-1} for p_{CO} = 540 mbar in a 10 cm absorption cell.*

In order to measure the self-broadening coefficient, γ_{CO-CO}, the CO P(21) absorption line is recorded for different pressures in a 10 cm-long absorption cell. A Voigt profile is then fitted to the experimental data and the values for the Lorentzian linewidths of the CO absorption line is measured at different pressures. Plotting the Lorentzian linewidths versus pressure as shown in Figure 5.13 gives a self-broadening coefficient $\gamma_{CO-CO} = 0.057 \frac{cm^{-1}}{atm}$ at room temperature. This measured value for γ_{CO-CO} is compared with the corresponding value given by the HITRAN 2003 database which is $\gamma_{CO-CO} = 0.054 \frac{cm^{-1}}{atm}$.

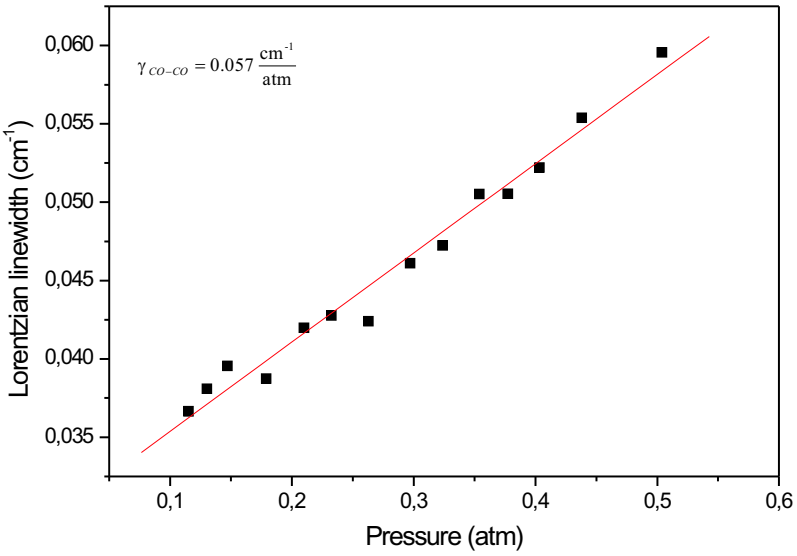

Figure 5.13: *Self-broadening coefficient measurement of the CO P(21) absorption line.*

This comparison leads to a relative deviation of about $\frac{\Delta\gamma}{\gamma} = 6.3\%$ and shows a good agreement between the HITRAN 2003 value and our measured one. The same data analysis is done to measure the collisional-broadening coefficient of the CO molecule with the CO_2 molecule by mixing with different CO_2 pressures while the CO pressure is fixed. As shown in Figure 5.14 the collisional-broadening coefficient of the CO molecule with the CO_2 molecule is measured to be $\gamma_{CO-CO_2} = 0.02 \frac{cm^{-1}}{atm}$.

5.2.1 CO measurement in combustions

Conventional techniques of combustion monitoring such as gas sampling probes, bypass analysis, and condensation or mass spectroscopy are useful for certain applications, but they are limited by their intrusiveness when used in flame measurements. In addition, conventional techniques require high maintenance because of the probe degradation from plugging or corrosion and frequent calibration. For example gas sampling probes cannot be used to measure highly reactive combustion intermediates such as OH radicals, and rather introduce errors to the measurements [107]. MIR laser absorption spectroscopy as a nonintrusive technique offers a lot of advantages for combustion diagnostics such as on-line and in-situ monitoring. The application of the present MIR DFG spectrometer to combustion measurements is shown as absorption lines of CO in the flame of a methane-air mixture flat flame *McKenna* burner are detected [108]. Well-characterized standard flames are a valuable tool for the calibration and verification of temperature and concentration measurement techniques. Flat flames stabilized on porous plug burners usually have an exhaust gas region that is spatially and temporally uniform. Figure 5.15

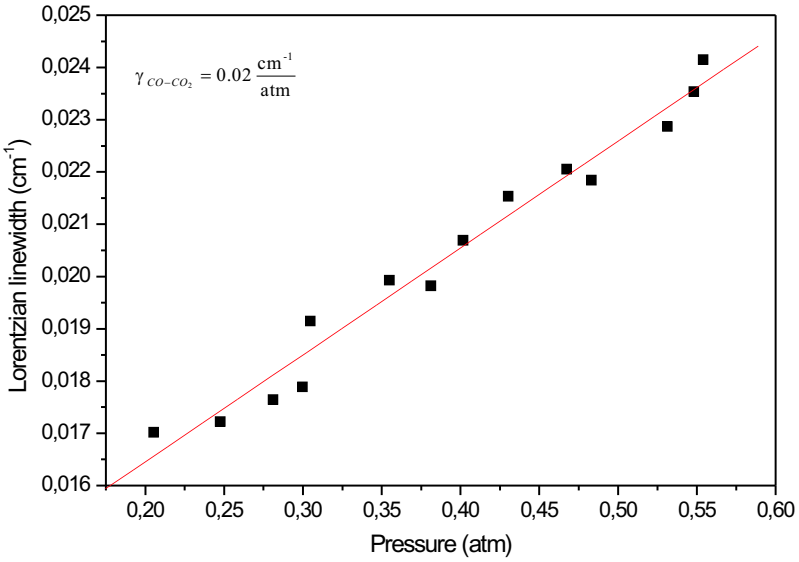

Figure 5.14: *Collisional-broadening coefficient measurement of the CO P(21) absorption line with CO_2 molecule.*

indicates a sectional view of a typical flat flame McKenna burner used in this investigation.

The body of the flat flame matrix burner (McKenna Product, Inc., Pittsburg, CA 94565) is made of stainless steel, with dimensions as shown in Figure 5.15. From two available models of McKenna burner, one with a bronze disk (95% copper and 5% tin) is used in our investigation. The porous plate for flame stabilization is cooled with a cooling coil sintered into the plate.

5.2.1.1 Interest in CO measurement in combustions

In addition to the interest in CO as primary combustion species, increasing concerns of CO as a pollutant have also been voiced due to the increasing demand for low NO_x emitting combustions. Low concentration of NO_x in combustions is often accompanied by the reduction of the combustion temperature in order to avoid the formation of *thermal* NO_x. This leads to an increase of the CO concentration in the combustion. Therefore, the ability to measure the distribution of CO generated by low NO_x combustion is of particular interest [109]. Furthermore, CO has the lowest boiling point of all infrared active gases and therefore it can be used to investigate the temperature dependence of line parameters.

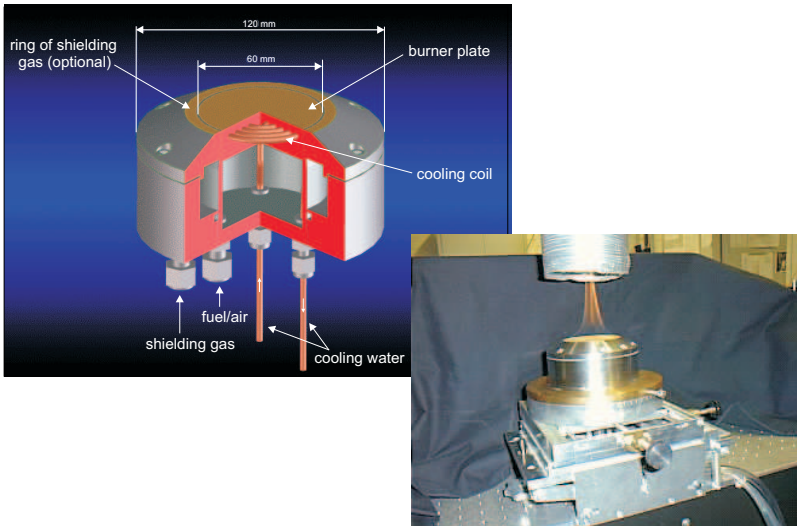

Figure 5.15: *A view of a flat flame McKenna burner as calibration tool.*

5.2.1.2 Detection of the CO P(21) line in a methane-air flat flame McKenna burner and relative CO concentration measurements

Figure 5.16 shows the experimental setup for the measurements of relative CO concentration in the combustion region of the flame of a McKenna burner.

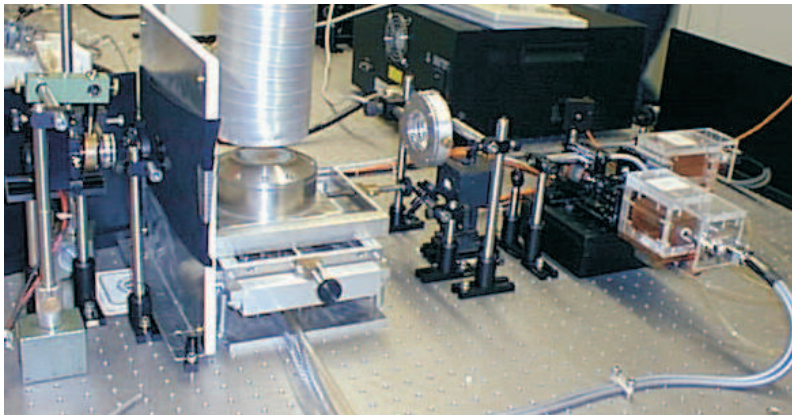

Figure 5.16: *Experimental setup for CO concentration in the flame of a McKenna Burner.*

Disturbing background radiation noise from the flame is blocked using a band pass filter [110] in front of the detector. The center wavelength of the band pass filter is λ = 4.9 μm and its bandwidth is 0.216 μm. Figure 5.17 indicates the transmittance of the applied band pass filter [111]. A paralleled MIR DFG laser beam is provided and transmitted through the flame. Then the flame is scanned by the MIR DFG laser beam with respect to the center of the burner for two different heights of 5 and 10 mm above

the burner surface. This is done while the flow rate of the methane was 1.5 $\frac{l}{min}$ without doping any CO to the flame. An example of a measured absorption CO P(21) line profile in the flame is shown in Figure 5.18.

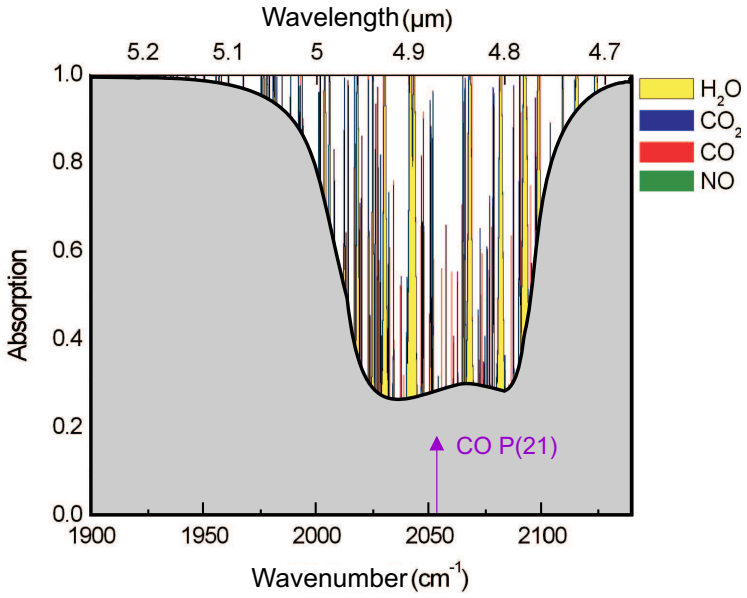

Figure 5.17: *The transmittance of the applied band pass filter in order to block the background radiation from the flame.*

The Lorentzian widths are measured by analyzing the CO absorption profiles in order to estimate the relative CO concentration in the flame. These measurements are done for different profiles through the flame with respect to the center line on the surface of the burner. The results are shown in Figure 5.19. The observed asymmetryic behavior of the flame is partly due to the disturbing external air flow which induces inhomogeneities of the CO concentration (refer to the positions 1, 2, and 8 in the Figure 5.19). As a result the application of the MIR absorption spectrometer based on the DFG process to combustion systems such as a McKenna burner shows the significant potential of the MIR DFG spectrometer to the in-situ combustion monitoring even in industrial applications. Therefore much benefits can be provided by using such compact and portable CO sensor for combustion diagnostics on-line and in-situ in industrial field measurements. In the next stage the described MIR DFG spectrometer is applied to image the CO concentration distribution in the flame of the McKenna burner through computerized tomography (CT) technique.

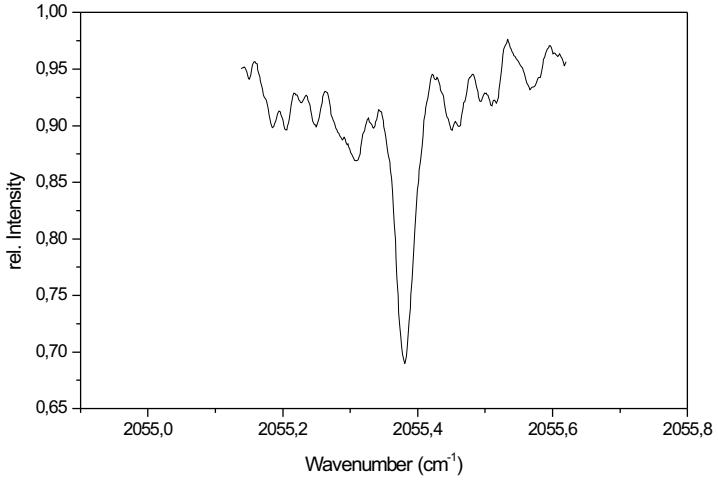

Figure 5.18: *An example of the detected CO P(21) absorption line 5 mm above the surface of the methane-air flat flame McKenna burner with a flow rate of 1.5* $\frac{l}{min}$.

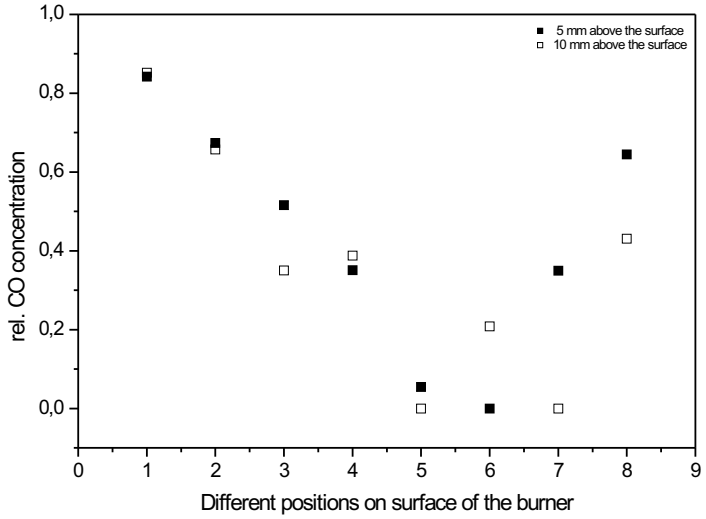

Figure 5.19: *CO concentration at different positions in the flame.*

6 Tomographic reconstruction of CO using MIR-DFG laser radiation

6.1 Tomographic reconstruction technique

The progress in combustion science has been associated with the availability of relevant experimental data, including the distribution of scalar properties in the flames. In the past, probe techniques were used for time resolved point measurements and during the last decade different nonintrusive laser diagnostic techniques have progressively been used for the same purposes. Some of those, for example optical sensors, have been used to characterize some typical flames and other techniques have been used to provide the basis for expanding combustion diagnostics, e. g. 3-dimensional scalar field measurements. The latter is a simple, commonly used and fully developed method for the monitoring and control of species formation in the combustions which can be provided by a modern technique of *tomographic* data acquisition [112, 113]. This technique has opened quite new possibilities of the high resolution imaging of various density distributions in multiple applications, including combustions. Tomographic reconstruction methods can be based on either absorption or emission techniques.

In laminar combustion flows, tomography has been used in combination with

- absorption spectroscopy (Chen and Goulard 1976, and Santoro et al. 1981),
- emission spectroscopy (Tourin 1983, Uchimaya et al. 1985), and
- simultaneous absorption/emission spectroscopy (Best et al. 1991)

as reviewed by Ferrăo and Pires [114] and by Sivathanu et al. [115] to retrieve local properties in both axisymmetric and non-axisymmetric laminar flames .

Absorption tomography is mainly used in the NIR spectral region from 1 to 2.8 μm using He-Ne and color-center lasers to perform a tomographic examination of the combustion at laboratory conditions. Most recently Hanson et al. [116, 117] have used NIR diode-lasers for the characterization of laboratory flames. Available powerful diode-laser sources in the NIR region enable the use of tomographic techniques in array arrangements which improves the speed of the data acquisitions.

Emission tomography can be used in a wider range of applications since it avoids the need for a background radiation source. From a review presented by Sivathanu et al. [115]

it is evident that the monitoring of the emission tomographic techniques have been applied on the measurement of local flame temperatures as it is done by Hertz and Faris (1988), Fischer (1992) or Sivathanu et al. (1995) in the laboratory scale. Leipertz et al. (1998) extended the use of emission tomographic technique to combustion chamber measurements in order to measure UV radicals (CN, CH, NH, OH) quantitatively for NO_x emission control in industrial combustion chambers. However, this technique is limited since the tomographic reconstruction did not involve any compensation of radiation extinction inside of the flame. The reader is referred to Reference [114] for more details.

For temperature and concentration measurements the absorption/emission (A/E) technique has been used by Yousefian et al. (1999) for axisymmetric propane/air flames. A/E was also used by Solomon et al. (1988) to study coal combustion phenomena and by Best et al. (1991) for the tomography of a laminar diffusion flame. Basically, in A/E technique the temperature is generally determined from the combination of absorption and emission spectra and then the absorption spectra is used to determine the concentration. The absorption spectra have been used by Mallery and Thynell (1997) and Ottese and Stephenson (1982) to determine the temperature in propellant flames. The major drawback of the A/E technique is its limitation regarding in-situ measurements. More details can be found in a review presented by Soufiani et al. [118].

In principle, CT reconstruction requires the measurement of M equally spaced beams on the lateral distance of the detection path along N different angles [119]. From this $M \times N$ data, the original image can then be reconstructed. In the case of axisymmetry, only an $M \times 1$ data set is required. The application of the CT technique to optimize industrial processes such as imaging of concentration and temperature distributions in gas-mixture flames and furnaces is advantageous because the monitoring of the emission is possible inside industrial combustion chambers. Previous work on the CT technique was focused on the numerical algorithm aspects of the tomography or on the proof of the principle measurements of non-combustion related species. An alternative to the CT imaging of combustions is known as planar laser induced fluorescence (PLIF) which is well-established as a diagnostic technique using UV or visible photons to excite the electronic transitions [120]. This excitation is done in the vacuum UV and therefore cannot be used as an efficient imaging in-situ technique for combustion products such as CO. Recently this method was coupled with IR cameras to introduce a new field of application known as IR-PLIF [121]. A new range of diagnostic techniques has been developed by making PLIF of vibrational transitions of molecular species. However, the major limitation of IR-PLIF is the low emission rate of vibrational transitions compared to electronic transitions.

When the CT method is applied to the quantitative evaluation, the correlation between the temperature and the concentration requires to either measure both simultaneously or

to find a sufficient estimation by separately measuring temperature and concentration. Currently the emission spectroscopy offers an accurate method for temperature determination (Zhu et al. 1997 [115]) in different lean premixed laminar flames (Ji and Gero, 2001 [122]) specially in the UV and visible spectral region. Recently, the determination of temperatures in the flames has been performed by using coherent anti-stokes Raman scattering (CARS) in high N_2 flames [123]. However, operation is not simple and intense laser radiation is needed which may cause perturbations in the flame. In the case of absorption spectroscopy the temperature can be determined by either the Boltzman distribution function [124] or intracavity laser absorption spectroscopy (ICLAS) [125]. While ICLAS provides a large spectral bandwidth (on the order of 100 cm^{-1}) its setup is complex and not applicable to high pressure measurements since the optical path length is too long (e. g. 30 Km) and the laser transition may be saturated. Furthermore, the quality of the mirrors of the laser cavity may be degraded when a sticky gas such as HCl is involved in the measurement.

In the present section the performance of the MIR DFG laser radiation is shown as CO concentration distribution measurements are conducted in the flame of a methane/air flat flame McKenna burner using the *computerized tomographic* (CT) reconstruction technique.

6.1.1 Projection detail and the Radon transform

For the CT method the imaged property is provided by the linear absorption coefficient so that

$$\ln\left[\frac{I_0(\nu,r,\theta)}{I(\nu,r,\theta)}\right] = \int_{path} F(x,y)ds \tag{6.1}$$

where $\frac{I_0(\nu,r,\theta)}{I(\nu,r,\theta)}$ is the normalized transmission of the absorbing species at frequency ν, radius r and angle θ, ds is some differential path length and $F(x,y)$ is the function describing the 2-dimensional distribution of the absorption coefficient of the imaged object. A new coordinate system can be defined by rotating (x,y) counterclockwise over the angle θ as shown in Figure 6.1. This gives a simple transformation as

$$\begin{aligned} r &= x\cos\theta + y\sin\theta \\ s &= -x\sin\theta + y\cos\theta. \end{aligned}$$

For a fixed angle θ the measured intensity profile as a function of r is given by

$$P(r,\theta) = \int_{path} F(r\cos\theta - s\sin\theta, r\sin\theta - s\cos\theta)ds \tag{6.2}$$

where $P(r,\theta)$ is defined as the *projection* profile of the function $F(x,y)$ along the angle θ. Normally, the projection profile is measured for θ ranging from 0 to π. In general, we have data for the projection profile for many different angles that can be placed into a big matrix

that is called a *sinogram* which results in a 2-dimensional set for $P(r, \theta)$. In the sinogram, the maximum deviation describes an object's distance from the origin and the point of peak deviation describes the angular location of the object. The transformation of a function $F(x, y)$ into the sinogram $P(r, \theta)$ is called the *Radon transform* $\Re\{F(x, y)\}$, named after Johann Radon, the founder of tomographic reconstruction in 1917. The radon transform is a projective transformation of a 2-dimensional function onto a polar coordinate space (r, θ).

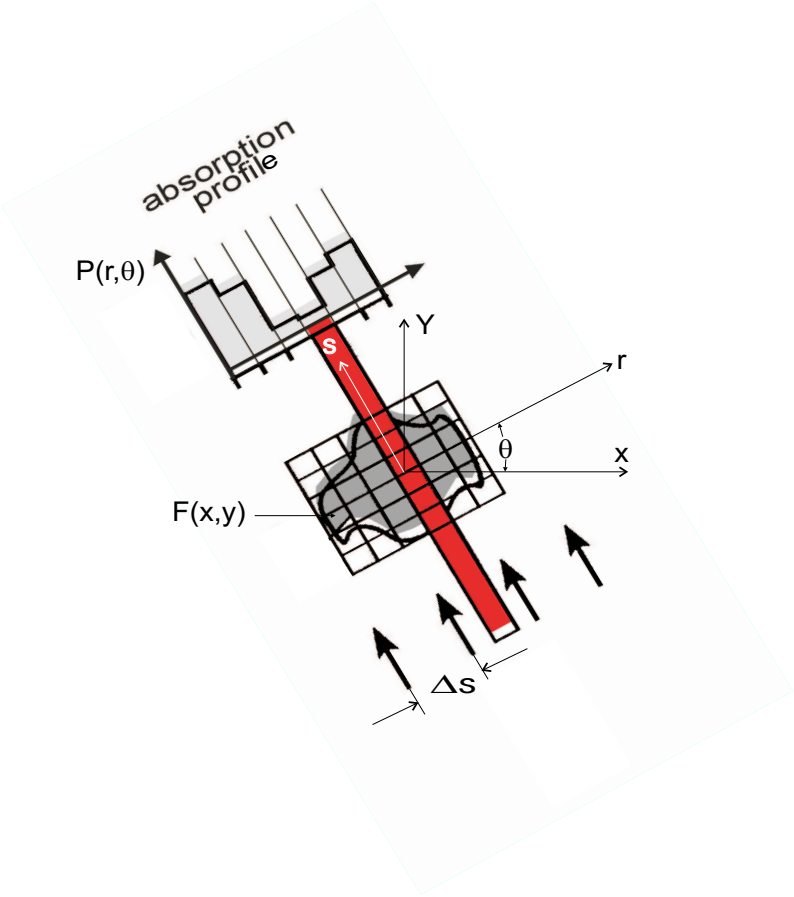

Figure 6.1: *The projection of $P(r, \theta)$ of the property field $F(x, y)$ along ds at angle θ.*

6.1.2 Image reconstruction

The main reconstruction setup involves a process that is known as *backprojection*. Backprojection means that we smear the projection data back across the object space, and the measurements obtained at each projection is projected back along the same line (and the same angle). This is done by Radon transformation. The procedure of obtaining a reconstruction of an image using the Radon transform is shown in Figure 6.2. The image reconstruction is the process of estimating an image $F(x, y)$ from a set of projections $P(r, \theta)$. Many different approaches can be used for the image to be reconstructed. One

way which is followed in this investigation is to use the filtered-backprojection technique (FBP) which is applied frequently for modern image processing. Clearly the original image $F(x, y)$ is not produced by the sinogram $P(r, \theta)$ and hence the Radon transform should be inverted to gives the original image by

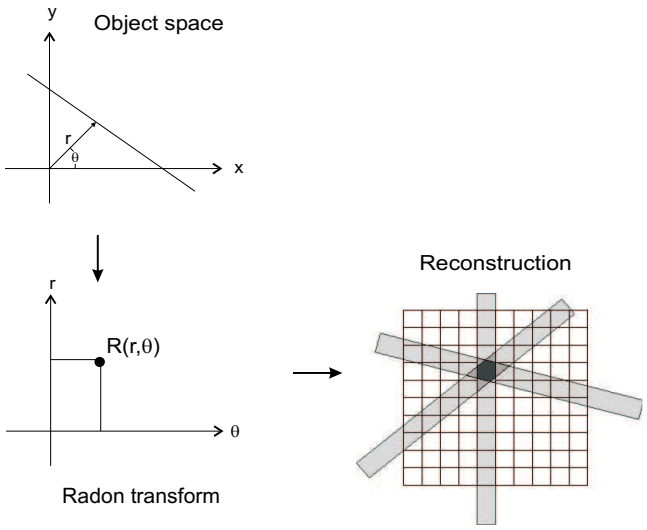

Figure 6.2: *Reconstruction procedure using the Radon transform.*

$$F(x, y) = \Re^{-1}\{P(r, \theta)\}. \tag{6.3}$$

In principle, if $F(k_x, k_y)$ is a 2-dimensional Fourier transform of the image $F(x, y)$ and $P(k, \theta)$ is the Fourier transform of the projection then it can be shown that

$$F(k_x, k_y) = P(k, \theta) \quad \text{for} \quad k_x = k\cos\theta, k_y = k\sin\theta \tag{6.4}$$

forms the projection theorem to calculate the value of the function $F(x, y)$ for each point in the xy plane by calculating the inverse Fourier transform of $P(k, \theta)$.

6.1.2.1 Filtered-backprojection technique

Mathematically, the backprojection operator for a single projection is

$$B(x, y) = \int_{-\infty}^{\infty} P(r, \theta)\delta(x\cos\theta + y\sin\theta - r)dr, \tag{6.5}$$

where $B(x, y)$ is the back-projected density due to the projection profile $P(r, \theta)$. The δ-function resembles the fact that the projection takes place along a line in the 2-dimensional

reconstruction volume. The total backprojected image over all single projections leads to a *laminogram* for N projection angles and M sampling positions along r as

$$f(x,y) = \frac{\Delta s}{2N} \sum_{j=1}^{N} \sum_{k=1}^{M} P(r_k, \theta_j) \delta(x \cos\theta_j + y \sin\theta_j - r_k) \tag{6.6}$$

where $\theta_j = \frac{(j-1)\pi}{N}$, $r_k = k\Delta s$, and Δs is the spacing between uniform samples. A filter has to be applied to the projection data since the laminogram represents a distorted image due to the spatial overlapping of all $M \times N$ lines in the reconstructed image [126]. All properties of the object in the real space can be performed by filtered backprojection technique. This means that the actual image is blurred by the $1/r$-term[1] in the real space. The δ-function now acts as a filter function and it has to be chosen so that its bandwidth retains all the essential features of the data. The smoothing Shepp-Logan low pass filter is used in this investigation to overcome the blurring effect. The Shepp-Logan filter originally was used for X-ray CT reconstructions for the human head (Shepp and Logan, 1974). It is given by [107]:

$$\delta(r_k) = -\frac{4}{\pi \Delta s^2 (4k^2 - 1)}. \tag{6.7}$$

In addition to the use of filtering functions the number of angles for summation N has to be sufficiently large to minimize and to prevent the distortion.

6.2 2D tomographic imaging of CO in a flat flame McKenna burner

2-dimensional images can be mathematically reconstructed from line-of-sight measurements across the sample. The CT technique does not generate 3-dimensional images of an object directly, thus 3-dimensional images can be generated by stacking up of 2-dimensional slices of the image. In this section the performance of the MIR DFG laser as a light source is demonstrated as tomographic imaging of the CO P(26) absorption line in the flame of a premixed methane-air McKenna burner as a probe is performed. The experimental setup is the same as discussed in detail in the proceeding chapter and shown in Figure 5.16. A laminar methane/air flame is provided on a flat flame matrix McKenna burner as shown in Figure 5.15. The burner is operated at a methane flow rate of 1.2 $\frac{l}{min}$ which is equal to the equivalent ratio of $\phi = 1.1$. 2-dimensional tomographic measurements are performed by clockwise rotating the burner in steps of 10° and perpendicular scanning of the flame by the MIR DFG laser in 5 mm steps as shown in Figure 6.3. That yields 285 data points for an area of about 40 cm^2. A lateral image resolution of approximately 2 mm is obtained. The limiting factors are the laser

[1]The density of projection lines is decreased by $1/r$. r is a weighting factor of the Fourier transformed data in the real space. The density of the projection lines decreased as $1/k$ in Fourier space and as $1/r$ in the real space.

beam width, the reconstruction algorithm, and the measuring speed. According to Figure 6.3 the recorded data in dependence on r and θ correspond to a sinogram of the intensity profile in the observed level above the surface of the burner. The sinogram is then filtered and backprojected to the main image as shown in Figure 6.4 for the CO P(26) absorption line for a typical height above the surface of the burner.

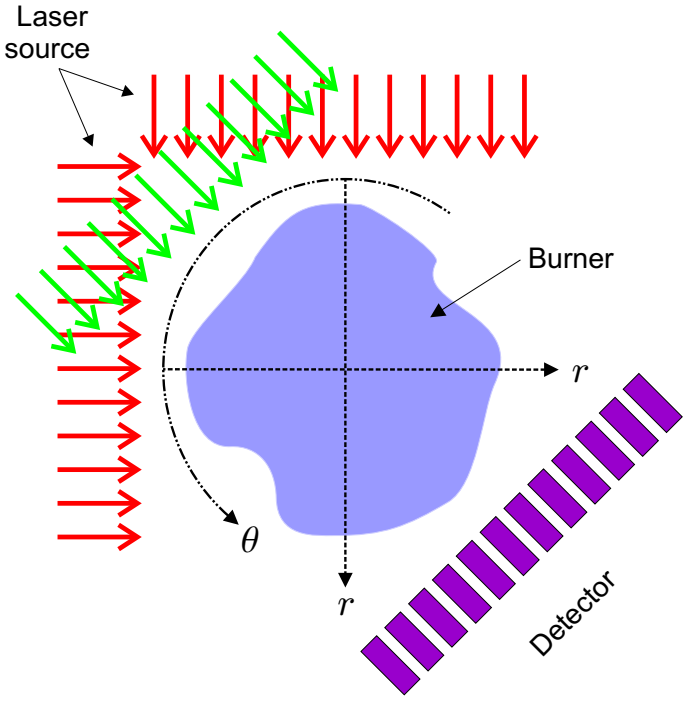

Figure 6.3: *A schematic of the tomographic procedure. The tomography is performed by rotating and lateral adjustment of the burner .*

To perform an accurate quantification of the reconstructed data, the temperature distribution in the flame was considered, since the CO concentration is correlated to the temperature through Gaussian widths of the CO profiles. A coarse temperature determination can be performed simultaneously to the absorption tomography using the Boltzman distribution of a transition linestrength of a certain species. The temperature-dependent linestrength of a molecular species can be written as [127]:

$$S_{n,m}(T) = (v+1)\frac{G(J)}{2J+1}\frac{N_{v,J}}{N}, \tag{6.8}$$

where v and J are the lower states quantum numbers respectively and $G(J)$ is the rotational transition factor. $G(J) = J+1$ for the R-branch and $G(J) = J$ for the P-branch. In the Equation (6.8), $\frac{N_{v,J}}{N}$ is the Boltzman distribution function of the populated vibrational levels and can be written as:

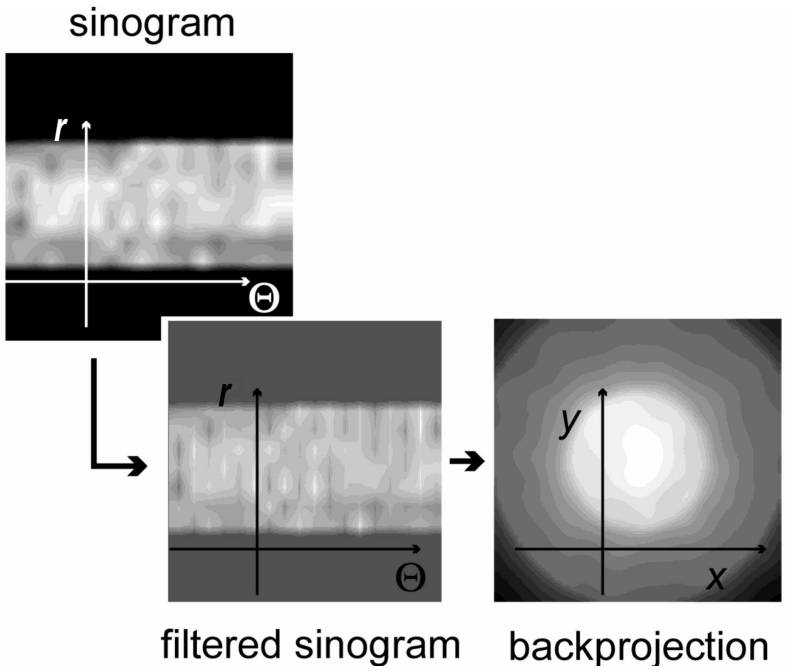

Figure 6.4: *Filtered and backprojected sinogram. This is done by using the Radon transform.*

$$\frac{N_{v,J}}{N} = \frac{2J+1}{Q(T)} e^{-\Delta E_{n,m}/k_B T}$$

$Q(T)$ is the *partition function* for vibration and rotation. Regarding Equation (4.13) and taking the ratio of absorption at the linecenter of two CO lines yields

$$\frac{[\ln(I/I_0)_{\bar{\nu}=\bar{\nu}_0}]_1}{[\ln(I/I_0)_{\bar{\nu}=\bar{\nu}_0}]_2} = \frac{[S_{n,m}\phi_V(\bar{\nu}-\bar{\nu}_0)|_{\bar{\nu}=\bar{\nu}_0}]_1}{[S_{n,m}\phi_V(\bar{\nu}-\bar{\nu}_0)|_{\bar{\nu}=\bar{\nu}_0}]_2}, \tag{6.9}$$

when p_{CO} and the path length L are fixed. The ratio of the two CO line intensities for temperature measurements is also considered by Soufiani et al. (2002) [118] when they have used Fourier transform infrared (FTIR) spectroscopy in the spectral region of 1700-4300 cm^{-1} and by Miller et al. (1993) [128] for a laminar methane-air flame using NIR absorption spectroscopy and also by Chang et al. [129] for diode-laser absorption spectroscopy of shock tubes. Since the temperature dependence of $S_{n,m}\phi_V(\bar{\nu}-\bar{\nu}_0)$ is known and further the line intensity ratio is independent of the concentration, thus the temperature can be obtained from the population distribution of the corresponding molecular states specified by quantum numbers through the last equation. In practice the ratio of $\frac{[\phi_V(0)]_1}{[\phi_V(0)]_2}$ may be evaluated by simultaneous measurement of the absorption linewidths. However, in

the investigation considered by Hanson and Falcone [127] no significant difference in the linewidths of different line pairs is observed and hence

$$\frac{[\phi_V(0)]_1}{[\phi_V(0)]_2} = 1$$

is found to be a good approximation, as it is applied to the present temperature determination. In addition, the success of a particular measurement is closely related to the selected spectral line. The proper choice of line results in a more accurate determination of the desired physical parameters and less manipulation to the experimental data [130]. The ratio of the absorption at the linecenter of two CO lines, CO P(26) at 2032.352 cm^{-1} and CO P(29) at 2018.148 cm^{-1} is taken for estimating of the temperature distribution in the flame. Data of the linestrengths and the energy of the states are provided by the HITRAN 2003 database. Assuming a symmetric temperature distribution the calculated temperature profile is averaged over all viewing $N = 13$ angles. All nonsymetric information caused by the low measuring speed of the present MIR DFG spectrometer is removed by that averaging. Assuming that the McKenna burner is a symmetric one this averaging does not affect the reliability of the measurement. The final results of the temperature distribution in the flame for three different heights in the flame is shown in the Figure 6.5.

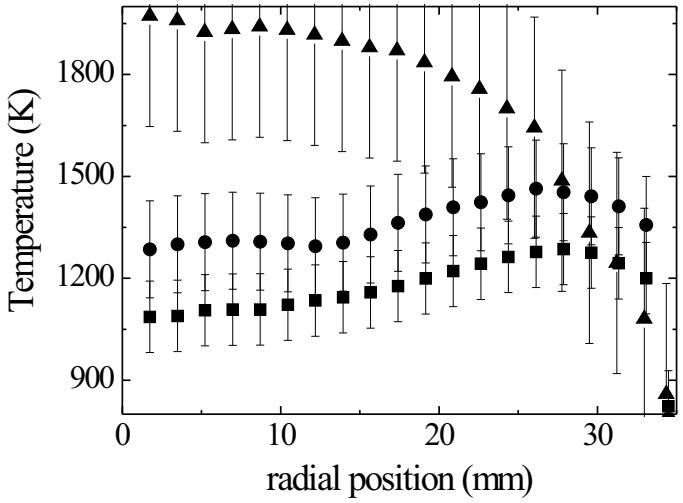

Figure 6.5: *Temperature distribution in the flame for three different heights in the flame (■ 1mm , • 6 mm, and ▲ 10 mm above the surface of the burner).*

6.3 Experimental results

Figure 6.6 shows a typical lineshape of the CO P(26) absorption line as measured in the flame.

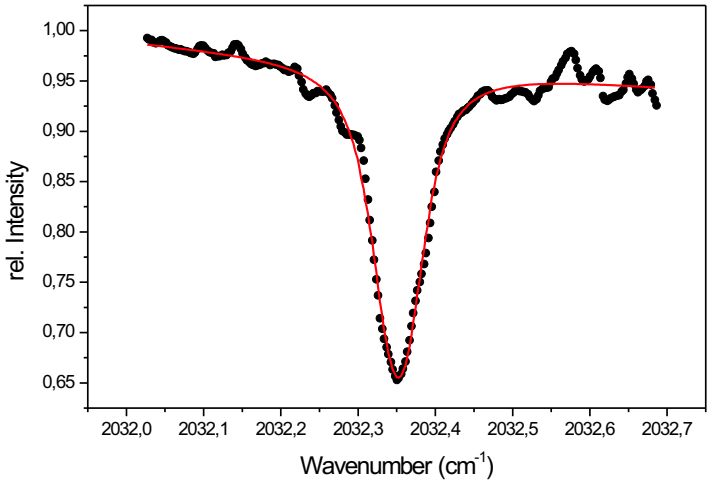

Figure 6.6: *MIR absorption spectrum of the CO P(26) absorption line at 2032.352 cm^{-1} as measured in a methane/air flame of the McKenna burner. Solid line: fitted Voigt profile, dots: measured CO profile 6 mm above the surface of the burner.*

This profile is measured while the MIR DFG laser is scanned over 1.2 $\frac{cm^{-1}}{volt}$ as determined by a Fabry-Perot etalon. Once the desired laser frequency for the CO P(26) line is achieved, a second check is made by performing the same frequency scan across pure CO in a 10 cm-long single pass absorption cell.

6.3.1 3D tomographic imaging of the CO-concentration profile in the flame

The same procedure as discussed in the previous section to reconstruct the CO profile is done for three different heights above the surface of the burner. The results is shown in Figure 6.7. The low speed of the data collection allows the assumption of a symmetric sinogram as it was done for the temperature profile, too. This enables to compare the present measurement with the prior measurements. Figure 6.8 shows the reconstruction profile before (a) and after (b) symmetrising the sinogram for the CO profile 1 mm above the surface of the burner. Quantitative results are summarized in Figure 6.9. They show a maximum CO concentration of about 2.5 Vol% (equal to 0.025 CO mole fraction) at a height of 10 mm above the surface of the burner. This measured CO concentration is in good agreement with the reported one which was measured to be about 2.6 Vol% in the post-flame of a similar methane/air McKenna flame by two-photon LIF spectroscopy [131]. The CO concentration of about 2.7 Vol% is also obtained by using chemical kinetic calculation [132] which again confirms the measured data.

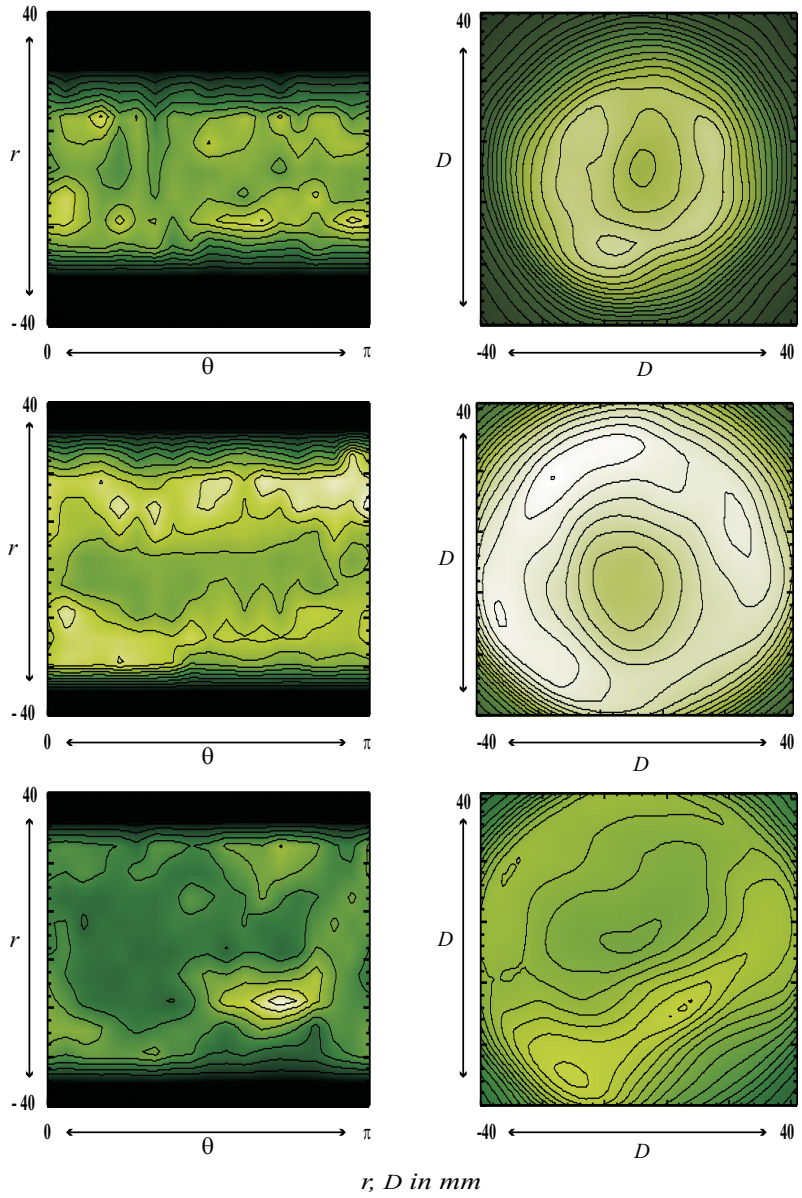

Figure 6.7: *Measurements of the CO P(26) absorption line in the flame of a McKenna flat flame burner. left: Sinogram, right: backprojection. (from the bottom to the top: 1, 6, and 10 mm above the surface of the burner).*

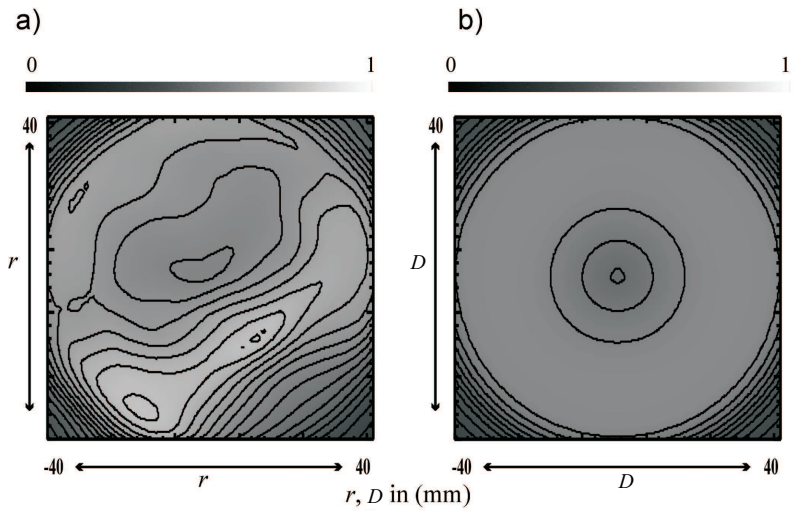

Figure 6.8: *Reconstructed CO P(26) sinogram (a) before and (b) after symmetrysing the sinogram.*

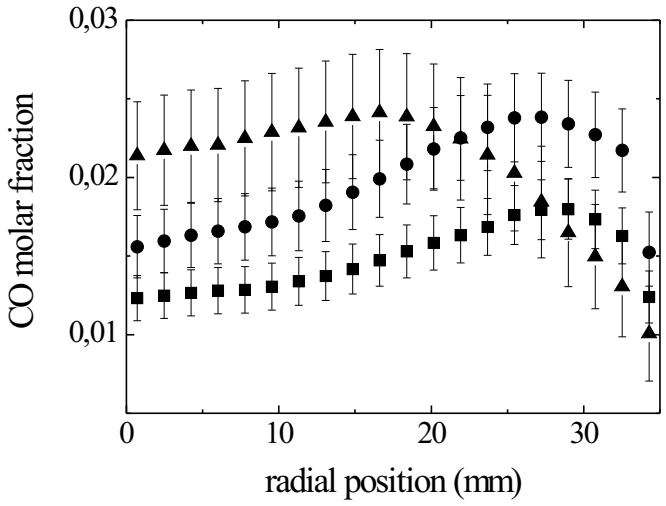

Figure 6.9: *Reconstructed CO molar fraction in the flame (■ 1mm , ● 6 mm, and ▲ 10 mm above the surface of the burner).*

3-dimensional tomographic imaging is achieved by performing tomographic measurements at different heights (1, 3, 6, and 10 mm) above the surface of the burner after scaling, backprojecting, and filtering of the data for both the symmetrical and the asymmetrical sinogram. However, the temperature distribution is assumed to be symmetrical for both cases. The results of the 3D tomographic reconstruction of the CO concentration is given in Figure 6.10.

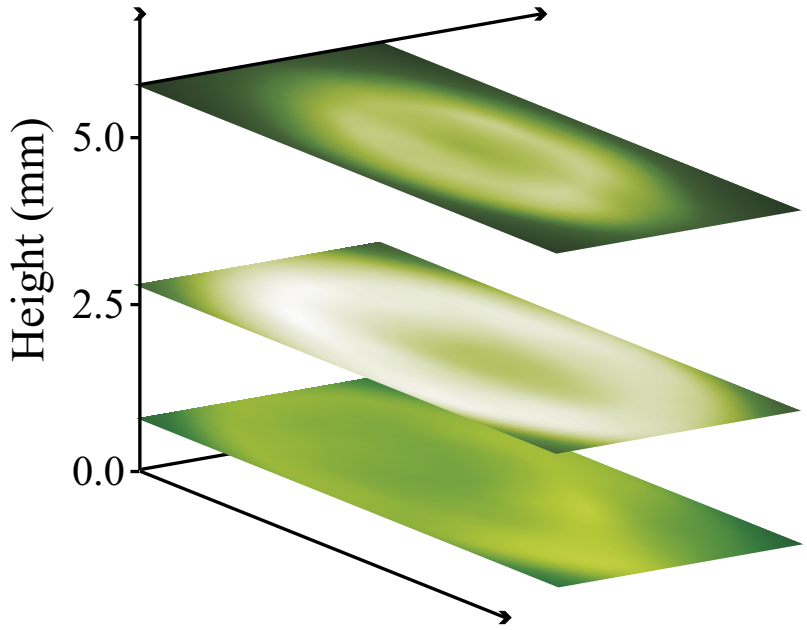

Figure 6.10: *3-dimensional representation of the reconstruction of the CO concentration in the flame assuming symmetrical sinogram.*

7 Wide tunable MIR DFG laser for simultaneous measurement of CO and NO

The discontinuous tuning range and the lack of reproducibility of the operating conditions of diode-lasers used in the MIR DFG spectrometer as pump and signal laser sources are unattractive for many sensing applications and limit the MIR DFG radiation to some specific wavelength regions. In order to overcome those problems several approaches are considered leading to an attractive field of research. In principle, all diode-lasers can be wavelength tuned in two different ways:

1. by adjusting the temperature of the diode-laser, and
2. by the injection current density into the gain medium.

In the first approach the effective optical index of the waveguide is changed, thereby adjusting the resonance condition of the laser. In this method each diode-laser can typically be tuned over 3 to 5 nm. For Fabry-Perot (FP) lasers, this tuning range is typically not continuous and exhibits hysteresis and regions of multi-mode instability. Continuous tuning ranges between mode hops may be as small as 0.1 nm to 0.3 nm for a typical diode-laser as used in the present MIR DFG spectrometer setup as signal and pump sources. This type of tuning is usually limited mainly due to the thermal mass of the diode-laser material and by the precision of the temperature controller system.

By the second approach at any given temperature, the injection current can be varied to modulate the optical index of the gain medium. Of course the output power is also modulated, but the laser wavelength may be tuned extremely rapidly. Typical FP diode-lasers can be tuned at a rate of about 0.015 $\frac{nm}{mA}$ ($\sim$ 0.25 $\frac{cm^{-1}}{mA}$). The total continuous tuning range is highly device dependent and a function of the laser gain medium and also of the fabrication technique. In principle FP lasers have many economical benefits, but they are generally noisy and slow devices. FP lasers can be divided into two groups [133]:

1. buried heterostructures (BH), and
2. multi quantum well (MQW) devices.

Compared to BH types MQW lasers are becoming very widespread. They offer

- lower threshold current,

- higher slope efficiency,
- lower noise,
- better linearity, and
- less sensitivity regarding temperature variations.

One disadvantage of MQW lasers is their tendency to be more susceptible to back reflections as it is true for nearly all diode lasers. Back reflections disturb the standing wave oscillation in the laser cavity and the net effect is an increase in the effective noise floor of the laser. Strong back reflections may cause some lasers to become widely unstable and completely unuseful in some applications. They also generate nonlinearities called *kinks* in the laser response. Higher back reflections may result in amplitude fluctuations, frequency shifts, the limitation of modulation bandwidth, or even in the worst case damage. Optical diodes based on Faraday isolators can be used to overcome the back reflection effect. One type of typical MQW lasers are vertical cavity surface emitting lasers (VCSEL) with lasing occuring in layers only 20-30 atoms thick. VCSEL posses a new laser structure that emits light vertically from its surface and has a vertical laser cavity. The small size and high efficiency mirrors of VCSELs produce a low threshold current below 1 mA. However, the performance of a VCSEL is generally limited by the extremely low roundtrip gain in the cavity and the VCSEL output polarization is difficult to predict and control [134].

The most common method for improving the wavelength control of diode-lasers is to form a spatially periodic modulation of the refractive index in the material adjacent to the gain medium. Such a device is called distributed feedback (DFB) laser which was grown at λ=760 nm by Morris et al. (1995) [135]. In a FP laser the resonator is formed by a cleaved surface or facet of the semiconductor material while in a DFB laser the resonator is distributed along the gain medium. Therefore a feedback at a particular wavelength produced by a periodic structure can be enhanced in a DFB laser. DFB lasers are very selective in wavelength and can be temperature tuned over 3 to 5 nm. Tuning of a typical DFB laser by the injection current is limited by the lasing threshold to about 0.01 $\frac{nm}{mA}$ [99]. Due to the long interaction length of a DFB laser very narrow linewidth radiation can be obtained resulting in very pure monochromatic radiation which is advantageous for high selective absorption spectroscopy. A typical linewidth is in the order of 10 MHz to a few hundred kHz [136]. A further advantage of the narrow linewidth property of a DFB laser is the small signal distortion due to chromatic dispersion in long fibers. Compared to FP lasers, DFB lasers have a higher SNR and are generally faster in response. Compared to VCSELs, DFG lasers cover a wide range of the operating wavelengths e.g. from 680 nm to 2 μm [137].

In a DFB laser the output power and the wavelength are not independent. This limits the tuning range of the laser by injection current mainly due to the threshold/damage

limitation of the gain medium. To overcome this disadvantage the wavelength selective and gain section can be separated, thereby decoupling the output power from the wavelength tuning. Such device is called distributed bragg reflector (DBR) laser where the maximum reflectivity inside the resonator occurs under the Brag condition for a given wavelength specified by λ_g. In the case of a DBR laser a wide tuning range can be achieved [138] since it is not limited by threshold/damage limits of the gain medium. The typical linewidth of DBR laser radiation is in the order of 1 MHz. Due to this extreme narrow linewidth, DBR lasers have been applied to gas sensing [99].

The most successful implementations of tunable diode-lasers with respect to both tuning range and linewidth use external cavities. In such an external-cavity configuration, tuning of the laser wavelength over most of the gain medium is possible by using a wavelength selective element such as a grating to obtain single-mode operation. Two basic arrangements of an external-cavity diode-laser (ECDL) are Littrow [139] and Littman [140] configurations. In a Littrow device an external grating is turned to tune the laser output wavelength and due to this grating movement the laser beam moves once the laser frequency is tuned [141]. Contrary, in a Littman device the grating is fixed and the wavelength tuning is done by a mobile bulky mirror which leads to the limitation of tuning speed and hence the tuning rate is limited to a few kHz [142]. However, the tuning range of a Littman ECDL device is as wide as 100 nm and it can be further enhanced by proper choice of the anti-reflection coating of the front facet of the diode-laser since a second set of cavity modes can be formed by weak reflectance from the facet with imperfect coating and hence some mode hops in the tuning range and polarization and amplitude modulation of the output with tuning may occur. As a result since both Littrow and Litman ECDL devices have a larger physical size compared to a simple current- and temperature-tuned diode-laser and require mechanical motion of either grating or mirror to operate, they are not suitable for pump and signal sources of a DFG laser for a compact gas sensor.

An alternative and easy approach for single mode operation control is to build an external short-cavity around the diode-laser. In the present chapter the tunability of the previously described MIR DFG spectrometer is enhanced by mode behavior improvement of the diode-laser pump source through constructing an external short-cavity around the diode-laser. A spectral tuning range of 71.5 cm^{-1} between 4.9 to 5.1 μm with an output power of hundred nW and a linewidth of less than 1.2×10^{-2} cm^{-1} for the MIR DFG laser is obtained in this investigation. The performance of such external short-cavity MIR DFG laser spectrometer is demonstrated monitoring fundamental rovibrational absorption spectra of CO and NO molecules in a 10 cm long single pass absorption cell at room temperature in order to estimate line broadening coefficients of both CO and NO molecules which are of general interest in combustion diagnostics.

7.1 Experimental setup

The schematic setup of the external short-cavity MIR DFG laser spectrometer is shown in Figure 7.1.

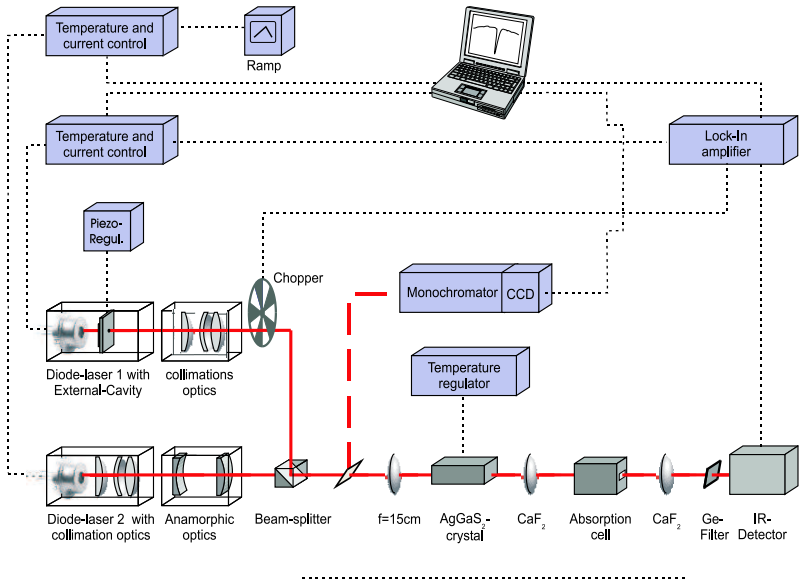

Figure 7.1: *Experimental setup of the external short-cavity MIR DFG laser spectrometer.*

The signal and pump beams are generated by two cw single-mode diode-lasers. All the optical and electronic elements used in this experimental setup are the same as explained in detail previously (refer to section 5.2.2) except for the modified pump laser source.

7.2 External short-cavity configuration for the pump diode-laser

The use of diode-lasers as signal and pump sources in the DFG system is favorable because of their small physical size and the fact that they are easy to handle but strongly limits the range of accessible MIR wavelengths in the DFG conversion. The continuous tunability of the MIR DFG radiation is limited by the typical mode jump behavior of the diode-lasers. Efficient MIR DFG radiation requires single-mode operation as well as wide tunable pump and signal diode-lasers. Single mode operation of a typical diode-laser is only possible for specific wavelength regions within its gain profile. However, the tuning characteristics of a diode-laser can be significantly improved by constructing an external short-cavity around the laser. This is done in this investigation by using an uncoated glass plate (thickness: 500 μm) mounted on a piezo stack and fixed very close ($L_c \leq 200$ μm) to the laser output facet to form an external short-cavity together with the other facet of the laser chip [72]

as shown in Figure 7.2.

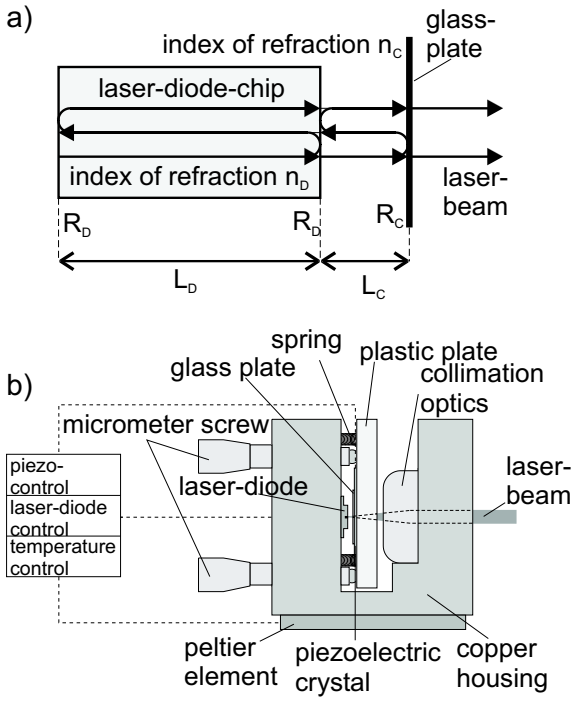

Figure 7.2: *Schematic (a) and experimental configuration (b) of the described external short-cavity [72].*

The specifications of the diode-laser used for this setup are:

laser 1 :	cw single mode diode-laser Mitsubishi ML1413R
specifications :	$\lambda_p = 682$ nm, $P_{max.} = 50$ mW, $I_o = 90$ mA,
	$\theta_{\parallel} = 10.6°$, $\theta_{\perp} = 18.3°$, tuning range : ~ 3 nm,
	measured slope efficiency : 0.096 $\frac{mW}{mA}$,
	measured maximum mode hop free tuning range : 0.083 nm

The mode structure of the mentioned diode-laser can easily be changed by varying the length L_c of the external short-cavity when the piezo voltage is slightly changed. Figure 7.3 indicates the experimental results of the application of two different piezo voltages to change the operational mode n to mode n+1. The separation of those two consecutive modes is measured to be 0.18 nm.

7.2.1 A simple physical model for the external short-cavity configuration

The experimental advantages of building such an external cavity around the diode-laser pump source has been discussed so far. In this section the benefit of the described configuration can be shown theoretically by using a simple physical model in order to calculate the transmission function of the device. The total transmission function I_t of the external

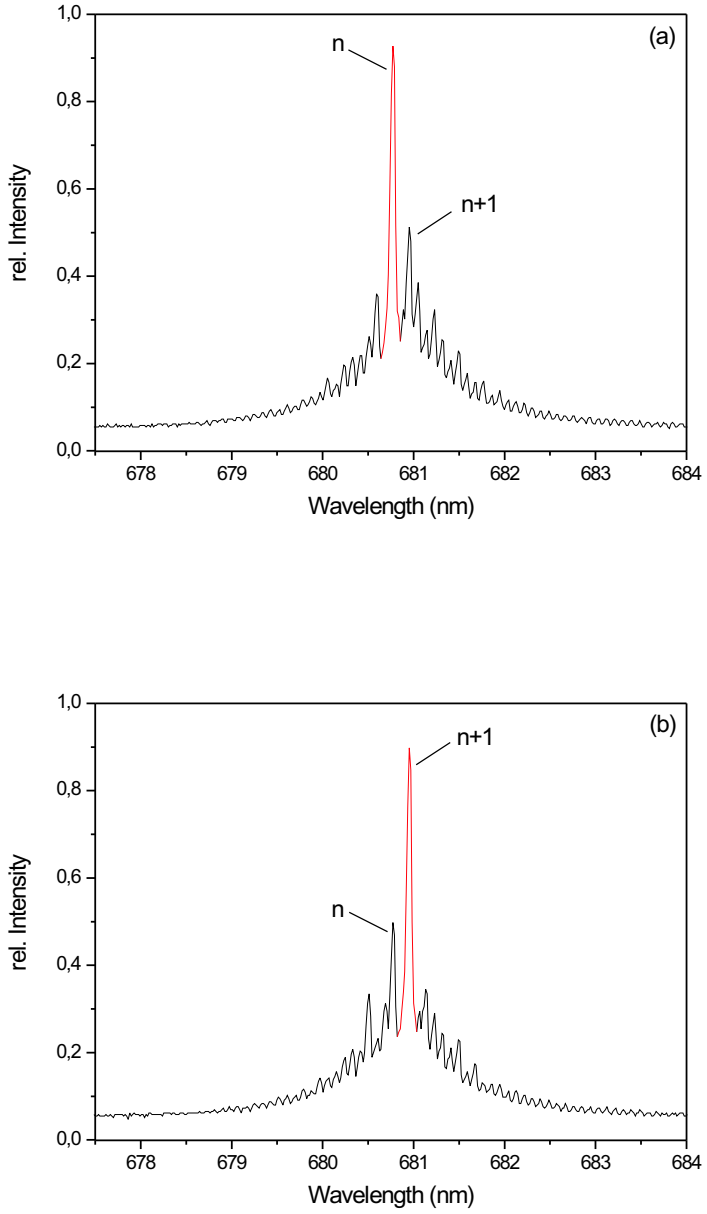

Figure 7.3: *Typical mode behavior of the external short-cavity Mitsubishi ML1413R diode-laser when applying different piezo voltages, $V_p = 12.3V$ for (a) and $V_p = 12.8V$ for (b).*

short-cavity configuration can be derived assuming a FP resonator treatment as shown in Figure 7.4.

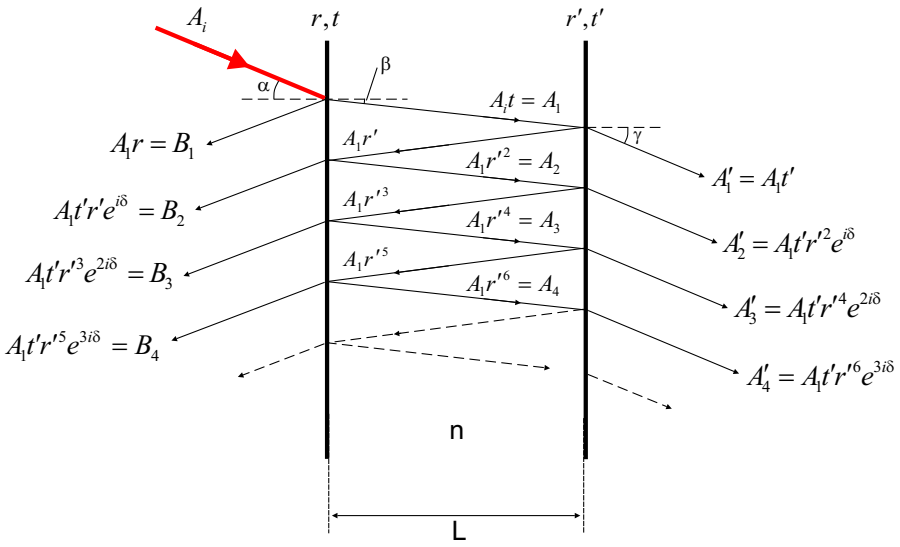

Figure 7.4: *A simple FP resonator used to derive the total transmission function of the external short-cavity configuration.*

Assuming an incident beam as $E_i = A_i e^{i(\omega t + \vec{k}\cdot\vec{r})}$ and starting with the amplitude of the incident electric field, A_i, the reflected amplitude from the first plate is given by B_1 while the partially transmitted amplitude from the second plate is given by A_1. The coefficients of reflection r and transmission t denote light travelling from the air to the medium with the refractive index n, while the coefficients r' and t' denote light travelling from the medium to the air. The multiple output rays differ in phase due to the different path lengths traversed by each ray. The optical phase acquired by the light on one round trip through the cavity is given by [143]

$$\delta = \frac{4\pi n L \cos\beta}{\lambda} \tag{7.1}$$

where λ is the wavelength of the incident laser beam and L is the length of the cavity[1]. The amplitude of each transmitted wave after penetrating the first plate can be calculated through

$$\begin{aligned} A_1 &= A_i t \\ A_2 &= A_1 r'^2 \\ &\cdot \quad\quad \cdot \\ &\cdot \quad\quad \cdot \\ A_m &= A_1 r'^{[2(m-1)]}, \quad m = 1, 2, \ldots . \end{aligned} \tag{7.2}$$

[1]There is an extra phase change due to absorption in the plate material which is equal to zero for lossless plates.

The amplitude of the beams coming out of the second plate can be obtained by

$$\begin{aligned} A_1' &= A_1 t' \\ A_2' &= A_1' r'^2 e^{i\delta} \\ . &\quad . \\ . &\quad . \\ A_m' &= A_1' r'^{[2(m-1)]} e^{i(m-1)\delta}, \;\; m = 1, 2, \ldots . \end{aligned} \tag{7.3}$$

Also the contribution of the amplitudes reflected from the first plate is

$$\begin{aligned} B_1 &= A_i r \\ B_2 &= A_1 t' r' e^{i\delta} \\ . &\quad . \\ . &\quad . \\ B_m &= A_1 t' r'^{(2m-1)} e^{im\delta}, \;\; m = 1, 2, \ldots . \end{aligned} \tag{7.4}$$

The sum of the transmitted wave amplitudes given in Equation (7.3) is then

$$\begin{aligned} A_t &= A_1' \left[1 + r'^2 e^{i\delta} + r'^4 e^{2i\delta} + \cdots + r'^{[2(m-1)]} e^{i(m-1)\delta} \right] \\ &= A_1' \sum_{m=1}^{p} r'^{[2(m-1)]} e^{i(m-1)\delta} \end{aligned} \tag{7.5}$$

for p reflections between the plates. Equation (7.5) leads for $p \to \infty$ to a geometric series by using the Stokes relations as[2]

$$A_t = \frac{A_1'}{1 - rr' e^{i\delta}} = \frac{A_i t t'}{1 - rr' e^{i\delta}}. \tag{7.6}$$

The total transmitted electric field is

$$E_t = \frac{A_i t t'}{1 - rr' e^{i\delta}} e^{i(\omega t + \vec{k}\cdot\vec{r})}. \tag{7.7}$$

Using the fact that $I = AA^*$, the last expression leads to a total output intensity from the resonator of:

$$I_t = I_0 \frac{(tt')^2}{(1 - rr')^2 + 4\sqrt{rr'}\sin^2(\frac{\delta}{2})}. \tag{7.8}$$

In a lossless system, the last equation simplifies to

$$I_t = \frac{I_0}{1 + f\sin^2(\frac{\delta}{2})}. \tag{7.9}$$

[2]Stokes relations arise by visualizing the rays running backwards in time so that tt' = 1- r^2 and r' = -r.

with $f = \frac{4\sqrt{rr'}}{(1-rr')^2}$. Equation (7.9) can be used for both the diode-laser resonator and the external cavity built around the laser. Replacing the parameters L, n, r, and r' for the external cavity as

$$L = L_C,\ n = n_C,\ r = \sqrt{R_D},\ \text{and}\ r' = \sqrt{R_C}$$

and assuming normal incidence ($\alpha = \beta = \gamma = 0$) we obtain

$$I_t = I_0 \frac{(1-R_C)(1-R_D)}{(1-\sqrt{R_C R_D})^2 + 4\sqrt{R_C R_D}\sin^2\left(\frac{2\pi n_C L_C}{\lambda}\right)}. \tag{7.10}$$

where R_C and R_D are the reflectivity of the glass plate mounted on the piezo stack and of the facet of the diode-laser chip, respectively. Assuming

$$L = L_D,\ n = n_D,\ \text{and}\ r = r' = \sqrt{R_D}$$

Equation (7.10) can be modified as:

$$I_t = I_0 \frac{(1-R_D)^2}{(1-R_D)^2 + 4R_D\sin^2(\frac{2\pi n_D L_D}{\lambda})} \tag{7.11}$$

for the diode-laser resonator. The total relative output intensity $I_{t0} = \frac{I_t}{I_0}$ of the external short-cavity diode-laser configuration as shown in Figure 7.2 can be written as

$$\begin{aligned} I_{t0}^{Ext} &= I_{t0}^{Diode} \times I_{t0}^{Cavity} \\ &= \frac{(1-R_D)^2}{(1-R_D)^2 + 4R_D\sin^2\left(\frac{2\pi n_D L_D}{\lambda}\right)} \cdot \frac{(1-R_C)(1-R_D)}{(1-\sqrt{R_C R_D})^2 + 4\sqrt{R_C R_D}\sin^2\left(\frac{2\pi n_C L_C}{\lambda}\right)}. \end{aligned} \tag{7.12}$$

This transmitted intensity can be simulated for some typical experimental parameters as shown in Figure 7.5. The typical parameters as used in this investigation are given in the figure caption.

The spacing of two consecutive modes (n and n+1) can be calculated from

$$\Delta\lambda = \frac{\lambda^2}{2n_D L_D} \quad (\text{for } \theta = 0), \tag{7.13}$$

known as free spectral range (FSR) of the diode-laser resonator. Assuming

$$L_D = 331\ \mu\text{m},\ n_D = 4,\ \text{and}\ \lambda = 681.07\ \text{nm}$$

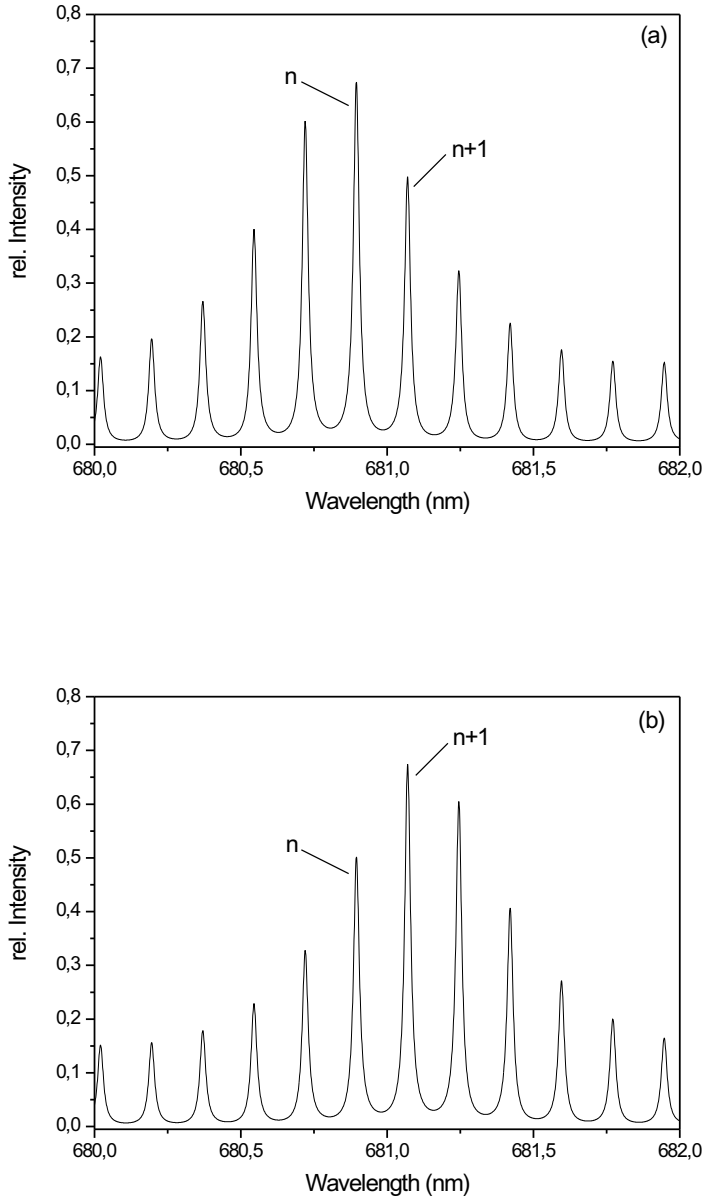

Figure 7.5: *Numerical simulation of Equation (7.12) for mode behavior of the external short-cavity diode-laser for two different resonator length (a) L_C = 112 μm and (b) L_C = 110 μm while the other parameters are fixed at R_D = 65%, n_D = 4, L_D = 331 μm, R_C = 20%, and n_C = 1.*

the separation of the two modes (refer to Figure 7.5) is then

$$\Delta\lambda_{FSR} = 0.175 \text{ nm}$$

which indicates a good agreement between measured and calculated values. While the FSR determines the peak location for a given wavelength, both the length L_C and the reflectivity R_C of the external cavity determines the maximum intensity at that wavelength. With this simple arrangement the accessible single mode operation of the diode-laser can be significantly increased as can be seen in Figure 7.6.

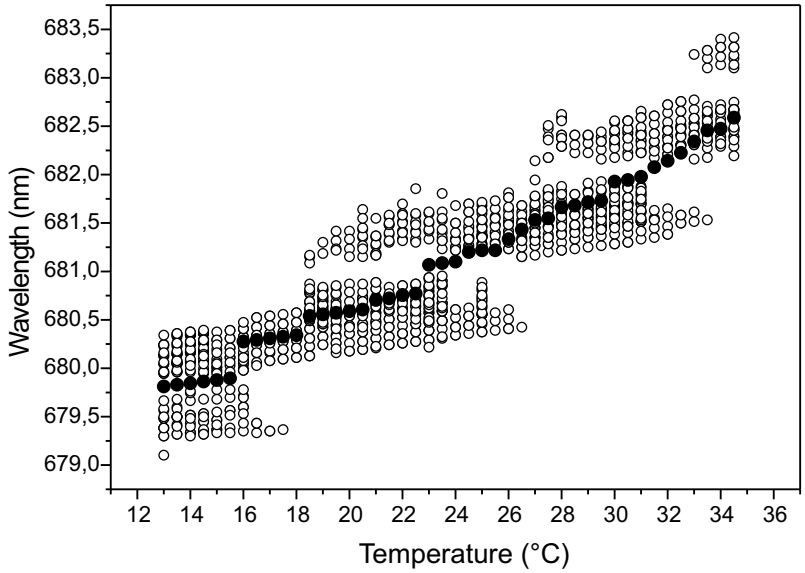

Figure 7.6: *Single mode laser operation with (○) and without (●) external short-cavity geometry for Mitsubishi ML1413R diode-laser.*

Therefore, the spectral tuning range of the MIR DFG laser can be significantly enlarged at moderate operation temperatures for the external-cavity as pump source since this geometry allows the modehop free tuning range of the diode-laser to be extended. The increased MIR DFG wavelengths obtained in this investigation are shown in Figure 7.7 and are compared with the obtained MIR DFG wavelengths using two standard chip diode-lasers. This broad and nearly continuous DFG tuning range is obtained using noncritical phase-matching by changing the crystal temperature from $T = 22.4°\text{C}$ to $T = 120.5°\text{C}$ and only applying the external short-cavity diode-laser as pump source while the signal source laser is still a standard chip diode-laser. Therefore, this tuning ability for the MIR DFG laser makes the scanning of multiple adjacent spectral features of a given molecule centered around 5 μm such as NO and CO absorption lines possible.

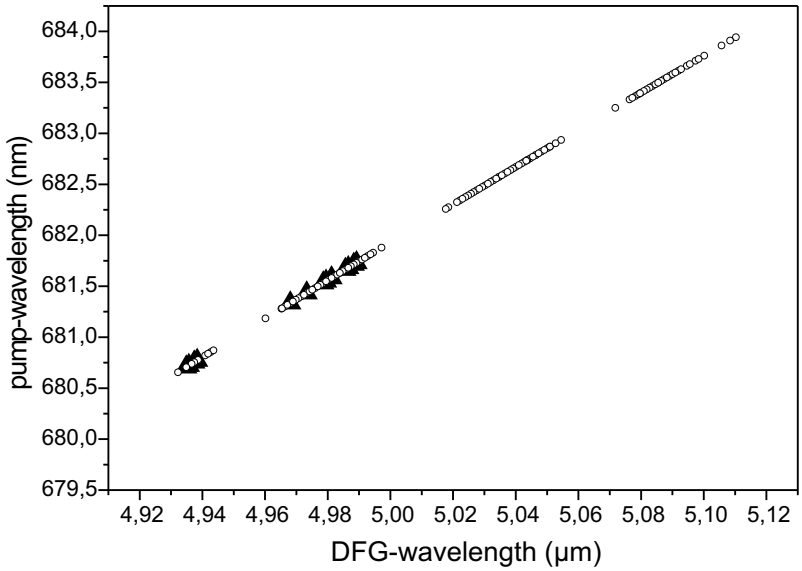

Figure 7.7: *DFG tuning curve with (○) and without (▲) using the external short-cavity geometry for the pump diode-laser. The phase-matching temperature is changed from* $22.4°C$ *to* $120.5°C$ *and the signal wavelength is fixed at 789.626 nm.*

7.3 Spectroscopic performance and results

In the present investigation the parameters of the DFG laser system are optimized for MIR operation around 5 μm to detect the rotational lines of CO and NO molecules which are important combustion-generated pollutants. The NO measurement is important for continuous optimization of the engine and/or furnace and for reduction of toxic NO_x emissions. The CO measurements provide the on-line determination of the combustion efficiency and serves as a global health monitor for combustion diagnostics [144].

7.3.1 NO molecule measurements

Figure 7.8 indicates the spectral lineshape of the NO 1-0 (R26) rotational line at 1955.67 cm^{-1} with a linestrength of $1.5{\times}10^{-22}$ $cm^{-1}/(molecule{\cdot}\ cm^{-2})$ [106] as measured in a 10 cm-long single pass absorption cell at room temperature and 90 mbar NO pressure. From the 12 NO R(26) lines reported in the HITRAN 2003 database we averaged on six lines because of our limited MIR spectral linewidth ($\sim 1.2 \times 10^{-2}$ cm^{-1}) and the low intensity [$S_{n,m} < 10^{-22}$ $cm^{-1}/(molecule \cdot cm^{-2})$] for the other six lines. Phase-matching is obtained by adjusting the temperature of the crystal at $T = (118.4 \pm 0.1)°C$.

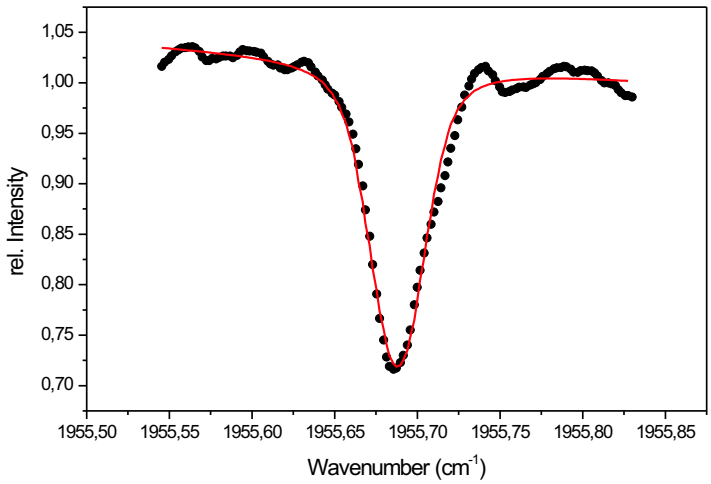

Figure 7.8: *Absorption spectra of the NO R(26) rotational line at 1955.67 cm^{-1} for p_{NO} = 90 mbar in a 10 cm-long single pass absorption cell. Solid line: fitted Voigt profile, dots: measured NO profile .*

7.3.1.1 Self-broadening coefficient (γ_{NO-NO}) measurements

The NO R(26) absorption line is recorded for different pressures in the absorption cell and the self-broadening coefficient (γ_{NO-NO}) for room temperature is obtained by fitting a Voigt profile to the experimental data and measuring the Lorentzian widths for the NO profiles at different pressures as it was done previously for the CO P(21) absorption line. The self-broadening coefficient $\gamma_{NO-NO} = (0.059 \pm 0.001)\frac{cm^{-1}}{atm}$ is obtained by plotting those Lorentzian widths for different pressures as shown in Figure 7.9. The error indicates the standard deviation of typically 12 individual measurements. The HITRAN2003 database does not contain the NO R(26) self-broadening coefficient. Only the NO broadening coefficient with air is reported: $\gamma_{NO-air} = 0.05\frac{cm^{-1}}{atm}$ which is in general agreement with the measured value in this investigation. The uncertainty of the above air-broadening coefficient is not available.

7.3.2 CO molecule measurements

The CO 1-0 P(27) rotational absorption line at 2027.649 cm^{-1} with a linestrength of 2.06×10^{-21} cm^{-1}/(molecule $\cdot$ cm^{-2}) is also detected in a 10 cm-long single pass absorption cell at room temperature and a pressure of p_{CO} = 85 mbar with the external short-cavity based MIR DFG spectrometer. The lineshape of the CO P(27) line is shown in Figure 7.10.

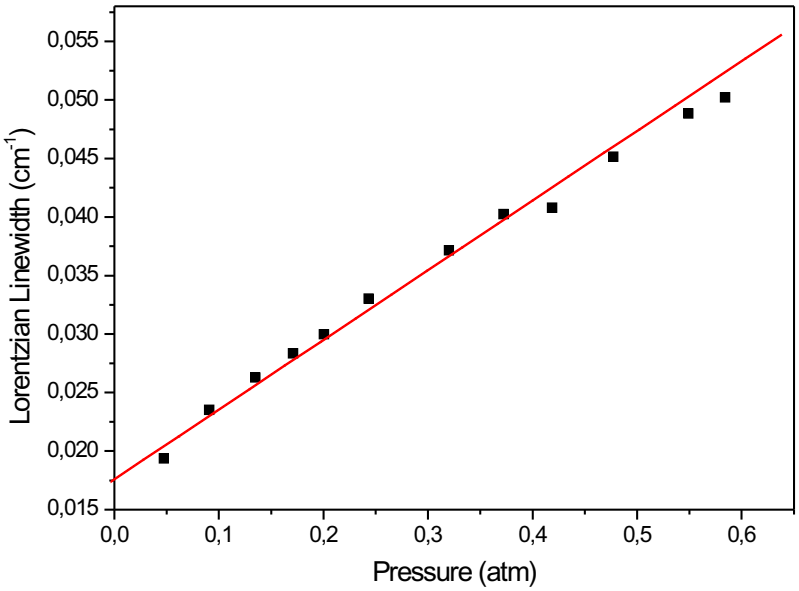

Figure 7.9: *Measurements of the self-broadening coefficient of the NO R(26) rotational line. Solid line: linear fit to the experimental data, dots: experimental data.*

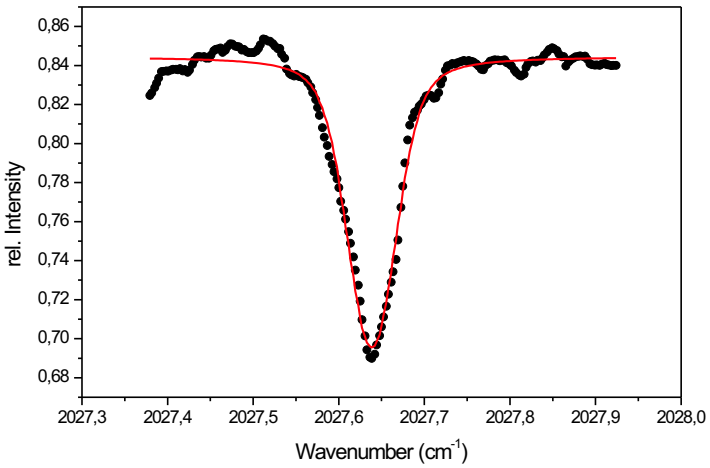

Figure 7.10: *Absorption spectra of the CO P(27) rotational line at 2027.649 cm^{-1} for $p_{CO} = 85$ mbar in a 10 cm-long single pass absorption cell. Solid line: fitted Voigt profile, dots: measured CO profile .*

7.3.2.1 Measurements of broadening coefficients for the CO P(27) absorption line

The same data analysis as described for the NO molecule is done to estimate the self-broadening coefficient of the CO absorption line. The results are shown in Figure 7.11.

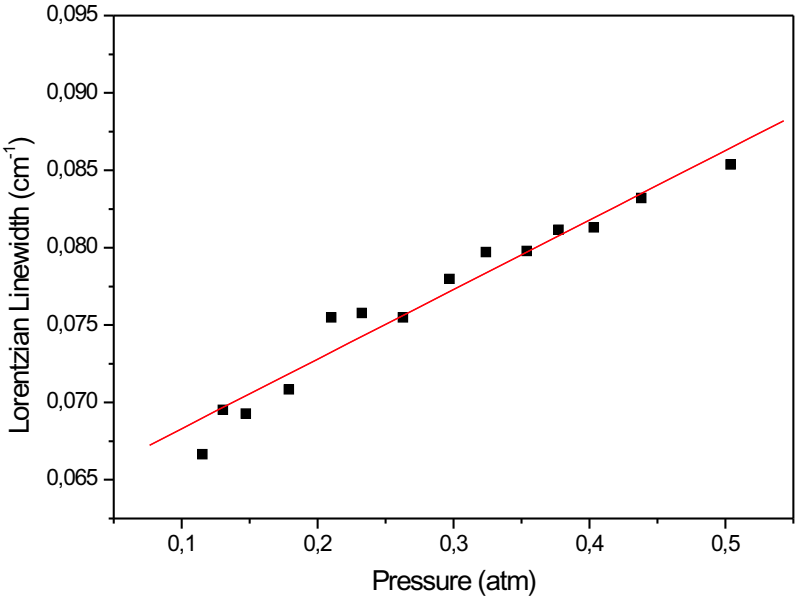

Figure 7.11: *Measurements of the self-broadening coefficient of the CO P(27) rotational line. Solid line: linear fit to the experimental data, dots: Experimental data.*

A self-broadening coefficient $\gamma_{CO-CO} = (0.045 \pm 0.003)\frac{cm^{-1}}{atm}$ is obtained. The measured value for γ_{CO-CO} in this experiment can be compared with the corresponding value given by the HITRAN2003 database: $\gamma_{CO-CO} = (0.049 \pm 0.002)\frac{cm^{-1}}{atm}$ which gives a standard deviation of $\Delta\gamma_{CO-CO} = 0.004$. In addition, the collisional-broadening coefficients of the CO molecule for P(27) absorption line are measured for different molecular species as shown in Figure 7.12. The results are summarized in Table 7.1. The collisional-broadening coefficient

Collisional-broadening coefficient γ_{CO-x}	spectral line	Measured values (cm^{-1}/atm)
γ_{CO-CO}	P(27)	0.045 ± 0.003
γ_{CO-N_2}	P(27)	0.041 ± 0.001
γ_{CO-O_2}	P(27)	0.048 ± 0.001
γ_{CO-CO_2}	P(27)	0.035 ± 0.002
γ_{CO-Ar}	P(27)	0.042 ± 0.001

Table 7.1: *Collisional-broadening coefficients measured for CO and different gases.*

for CO with air given in the HITRAN 2003 database is $\gamma_{CO-air} = (0.043 \pm 0.002)\frac{cm^{-1}}{atm}$. To compare the measured data with the HITRAN 2003 value the air-broadening coefficient

γ_{CO-air} can be calculated by using the relation [145]

$$\gamma_{CO-air} = 0.79\gamma_{CO-N_2} + 0.21\gamma_{CO-O_2}. \tag{7.14}$$

This gives $\gamma_{CO-air} = (0.042 \pm 0.001)\frac{cm^{-1}}{atm}$ for the present experiment which is in very

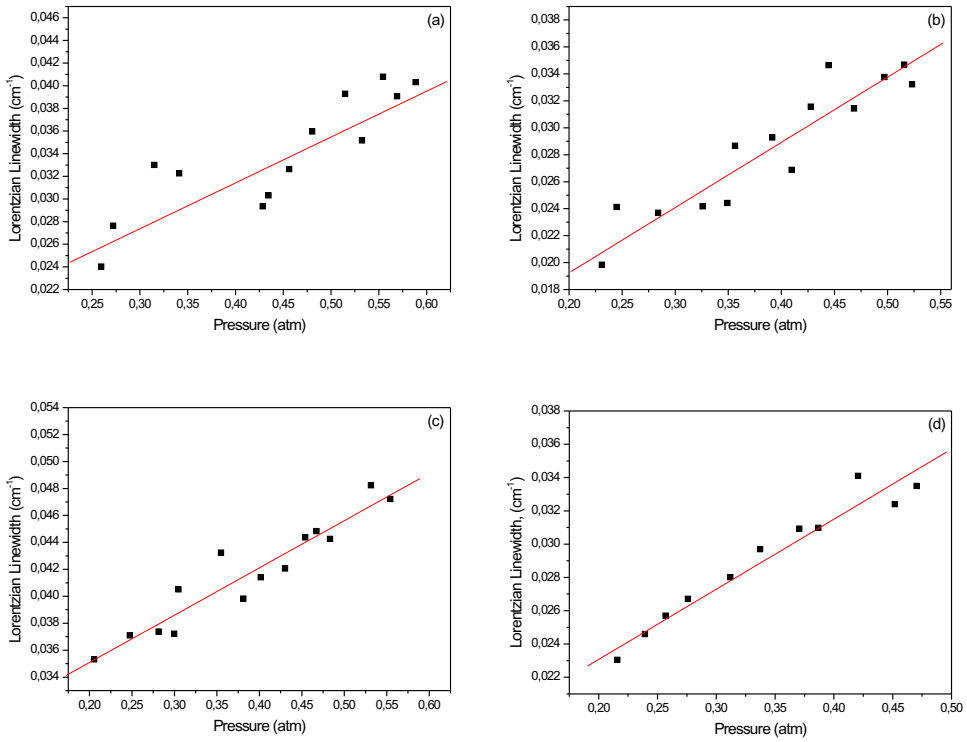

Figure 7.12: *Collisional-broadening coefficient measurements of the CO P(27) rotational line with (a) N_2, (b) O_2, (c) CO_2, and (d) Ar molecules. Solid line: linear fit to the experimental data, dots: experimental data.*

good agreement with the reported HITRAN 2003 value. These results indicate that self-broadening is the most dominant broadening process.

As a result a narrow linewidth and nearly continuous tunable MIR laser source in the spectral range from 4.93 μm (2028.397 cm^{-1}) to 5.11 μm (1956.947 cm^{-1}) is developed for the detection of CO and NO molecules. The spectral DFG tuning range is greatly enlarged (which is 71.5 cm^{-1}) compared to a MIR DFG laser based on two conventional diode-lasers as pump and signal sources. Applying such a broad MIR tuning range enables to detect the absorption lines of both CO and NO molecules. Littrow and Littman ECDL configurations are commercially available and those lasers provide a combination of extremely narrow linewidth and broad tunability. However, those configurations are complex, require dispersive elements in the cavity which extend the cavity length resulting in lower output efficiencies. Contrary, the external short-cavity geometry described in this

investigation allows wavelength tuning in a fast scheme and it offers numerous economical and experimental benefits such as a simple optical configuration, small geometrical size, and low cost.

8 MIR CO-sensor for in-situ monitoring of industrial combustions

To better understand the chemical reactions and formation of pollutants in combustion processes, and particularly for emission control, concentration and temperature measurements inside industrial combustion chambers are of great interest. This is specially true for glass melting furnaces when it comes to optimize the energy efficiency with regard to CO, NO, and SO_2 emissions. This can be done by a precise control of the combustion through sensing the physical states of e.g. the atmosphere in glass melting furnaces. Therefore, sensors for the monitoring of combustion gases are gaining importance. Most of such sensors are based on [146]

1. electrochemical,
2. mechanical, and
3. optical

measurements. In principle, an ideal gas sensor should [147]

- not be influenced by other gases or environmental disturbances such as dust,
- automatically compensate for temperature and pressure effects, and
- measure continuously with a short response time.

Additionally, a sensor for industrial applications should

- require little maintenance with few or no consumable parts,
- have high reliability and availability, and rather
- operate at room temperature.

Sensors based on fast and instant measurements give information about the process in an early stage. Therefore, each measurement applied to industrial monitoring should provide information on the formation of the combustion so that the process can be adjusted in the optimum direction. For example in a glass melting furnace a sensor should give a reliable

response related directly to the physical and chemical state of the melt in a short time. Conventional analysis applied to the combustion systems generally relies on extractive sampling techniques which have a long response time due to the long sampling lines and inherent delays from the analyzers. Contrary in-situ measurements of the combustion e. g. concentration measurements of the chemical species offer several advantages over conventional methods in terms of timeliness and less susceptibility to handling errors. The possibility of in-situ combustion diagnostics has opened a wide research area of developing spectroscopic monitoring techniques and devices in the past few years. However, intrusive in-situ techniques and devices such as solid-state sensors often disturb the local flame parameters since these types of sensors have to be placed into the combustion chambers. Thus the obtained results are always accompanied with errors. Furthermore, their performance is limited to the spatial conditions of the flame such as temperature and pressure of the species provided by the flow rate. For example the available sensors for glass melting furnaces are solid-state electro-chemical CO sensors. These sensors are only efficient at temperatures lower than 800°C and hence they can not be applied in glass melting furnaces where the temperature is set to about 1400-1500°C [148]. Therefore, harsh conditions such as high temperatures (and pressures) quickly lead to the sensor deterioration and aging.

Rapid in-situ combustion monitoring requires nonintrusive techniques and devices. The possibility of monitoring radicals such as OH, CH, CN, and C_2 in the combustion has introduced a nonintusive optical technique known as UV-flame emission spectroscopy where wavelengths $\lambda < 500$ nm are used. Since the emission spectrum of a hot glass melting furnace depends on the temperature of the melt, the emission of radiation at different wavelengths can be related to different components and the temperature at different depths in the melt. However, relevant gaseous combustion species such as CO_x and NO_x can not be monitored with this method and the determination of their concentration is limited to the uncertainty of the correlation to the appearance of the radicals [109].

Due to the unique properties of laser sources, a wide variety of nonintrusive techniques such as [67]

- Raman,
- fluorescence, and
- differential absorption techniques

have been investigated for combustion monitoring. None of these techniques is capable to continuously monitoring variations of thermodynamic properties across the medium and is universally applicable to all combustion species and all combustion environments. For instance, the Raman scattering technique is relatively insensitive and it suffers from the

interference with the fluorescence spectra of polynuclear atomic hydrocarbons, which are present in many hydrocarbon flames. LIF is also limited to the molecules with accessible electronic transitions and differential absorption spectroscopy (DAS) is limited to the molecules which have suitable absorption in the UV and visible region.

Recently, the application of NIR absorption spectroscopy to the in-situ sensing of combustion-generated pollutant emissions such as CO molecules using single mode tunable diode lasers is investigated as a new nonintrusive sensor for gas dynamics and combustion flows [149]. Due to the limitation of the application of NIR laser absorption spectroscopy in combustion monitoring as previously discussed, the applications sources in the MIR continue to appear in the scientific and engineering literatures. As reviewed by Allen [99] these include: monitoring of ammonia in coal combustion (Silver et al., 1991), NO in high-enthalpy shock tunnel flows (Mohammed et al., 1996), and aero-engine exhaust analysis (Wiesen et al., 1996). On-line measurements of the concentration of various hydrocarbons using QC-DFB lasers is investigated by Kosterev et al. [150]. A field measurements of volcanic gases based on Fourier transform infrared spectroscopy (FTIR) using a MIR DFG laser source is presented by Richter et al. [42], and NO and CO measurements in the exhaust of an engine using QC lasers is done by Wehe et al. [151] and by Manzel et al. [152].

In the present investigation the described MIR DFG laser is used as in-situ and nonintrusive gas sensor to estimate CO concentrations in the atmosphere of an industrial glass melting furnace. For a gas temperature of about 1100°C the CO concentration in the recuperator channel is measured to be 400 ppm.

8.1 MIR DFG gas sensor

A detailed description of the applied MIR DFG laser gas sensor including its experimental setup is given in section 5.2.2. The key advantages offered by the present MIR DFG gas sensor are

- narrow linewidth (less than 0.01 cm^{-1}), and
- reproduceable fast linear MIR wavelength scanning

necessary for high precision spectroscopy even at high temperature and pressure conditions. The MIR DFG laser system was calibrated via both room temperature measurements of the self- and the pressure-broadening of the CO P(21) and P(27) absorption lines and imaging of the CO P(26) in a methane/air flat flame McKenna burner by means of CT reconstruction technique. For the application of the MIR DFG gas sensor in the industrial environment the Dr. Genthe GmbH&CO. KG, Goslar, Germany, a producer of glasses for

automotive and lighting applications was chosen. The MIR DFG absorption experiments were performed at a natural gas/air fired furnace with a capacity of 12 t/d (FlexMelter). Batch temperatures are around 1500°C. The furnace operated with an oxygen excess of about 1%, corresponding to an air excess of 5%. The glass melt furnace under investigation is shown in Figure 8.1.

Figure 8.1: *A gas fired glass melt furnace of Dr. Genthe GmbH&CO. KG, Goslar, Germany at about* $T = 1400°C$.

Since the quality of the produced glass depends on the quality of the combustion, the radiative heat transfer from the combustion chamber to the glass melt and thus the energy efficiency of e. g. a methane gas fired glass furnace must be optimized.

Therefore, CO concentration in the atmosphere of a glass melting furnace is an effective and sensitive measure for optimizing the combustion process to avoid the formation of toxic gases such as NO_x emissions and to promote enough oxidant in the flame required for complete combustion. Therefore, the ability of the in-situ and on-line measurements of CO concentrations in the atmosphere of a glass melting furnace is of interest.

8.2 Results and discussion

During the measurement the MIR DFG laser system was placed into a water-cooled aluminum box (71 × 76 × 31 cm) as shown in Figure 8.2, to protect the system from the hot surrounding atmosphere ($T \sim 40°C$) on the factory floor near the furnace and from the dust.

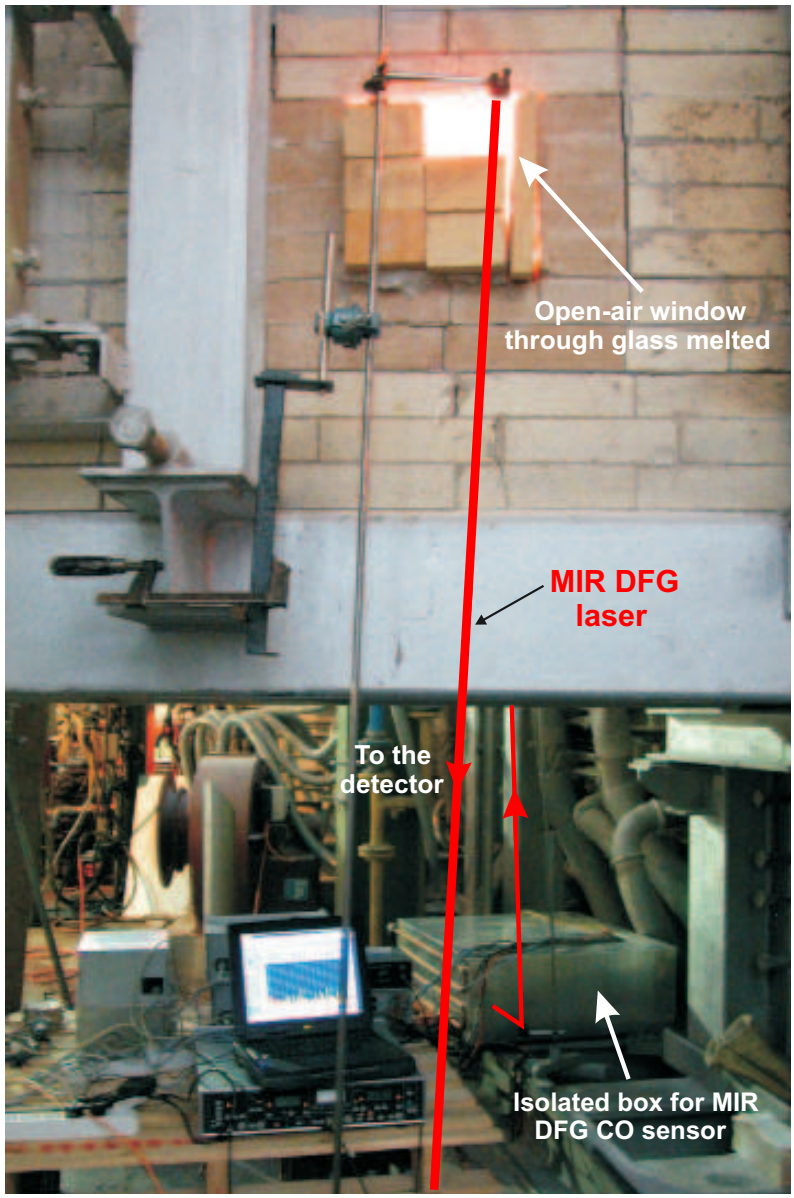

Figure 8.2: *An overall schematic of the compact isolated MIR DFG sensor, associated electronics and the measurement region within the glass melting furnace.*

A flow rate of dry air is also used to maintain a stable operating temperature. Thus the temperature inside the box was stabilized at about $T \sim 27°C$ which enabled the crystal temperature to be set at $T \sim (30.6 \pm 0.1)°C$ necessary for phase-matching. Hence, tuning the MIR DFG radiation was possible around 4.94 μm close to the single rotational line P(28) of the CO molecule at $\bar{\nu}_0 = 2022.914$ cm^{-1} with a linestrength of 7.47×10^{-20} cm^{-1}/(molecule $\cdot$ cm^{-2}) at $T = 1100°C$ according to the HITRAN 2003 database. The net absorption path length was about 1 m crossing the entry of the recuperator channel of the furnace at a gas temperature of about 1100°C. The MIR DFG laser was guided through the closer path using flat mirrors as can be seen in Figure 8.2. The extreme heat of the glass melt furnace as flame strike out of the window (as can be seen in Figure 8.3) created a strong background radiation resulting in additional noise that must be removed from the MIR DFG signal.

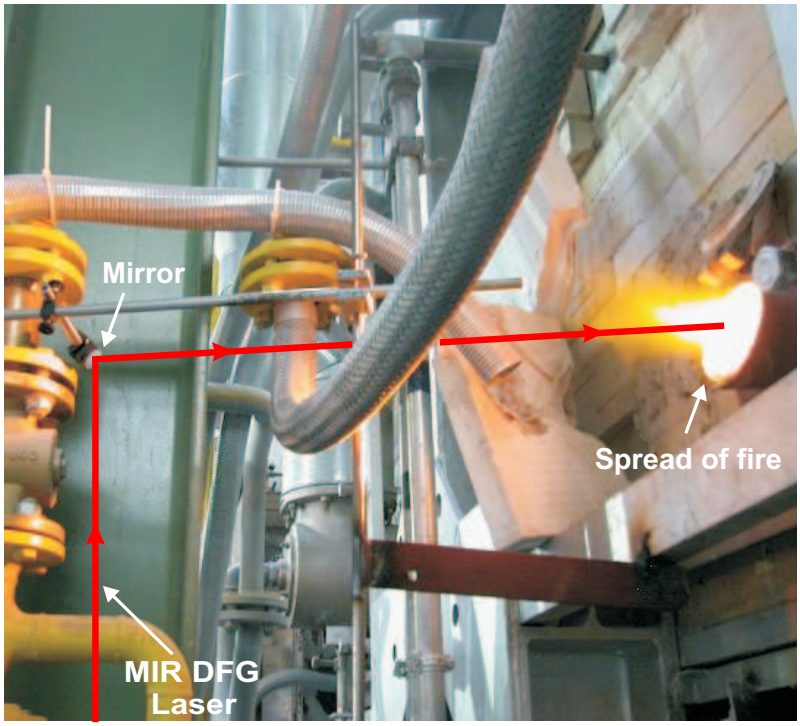

Figure 8.3: *The flame strikes out of the glass melt furnace. This causes a strong background radiation noise.*

To block the strong background radiation from the furnace and hence to improve the SNR of the detector, a MIR bandpass filter specified in Figure 5.17 was placed in front of the detector. Due to the local vibrations close to the furnace and the temperature gradient and temperature fluctuations resulting in variations of the refractive index within the furnace, spatial fluctuations of the laser beam will reduce the SNR significantly. This is noticed by fluctuations of the intensity and the spot size of the visible pump laser beam. The temporal variation of the beam shape and the position was determined by analyzing 21

measurements of the visible pump laser beam taken with a beam profiler for about 1.4 seconds. This is done for the laser beam before and after crossing the furnace. Results of the measurements are shown in Figure 8.4.

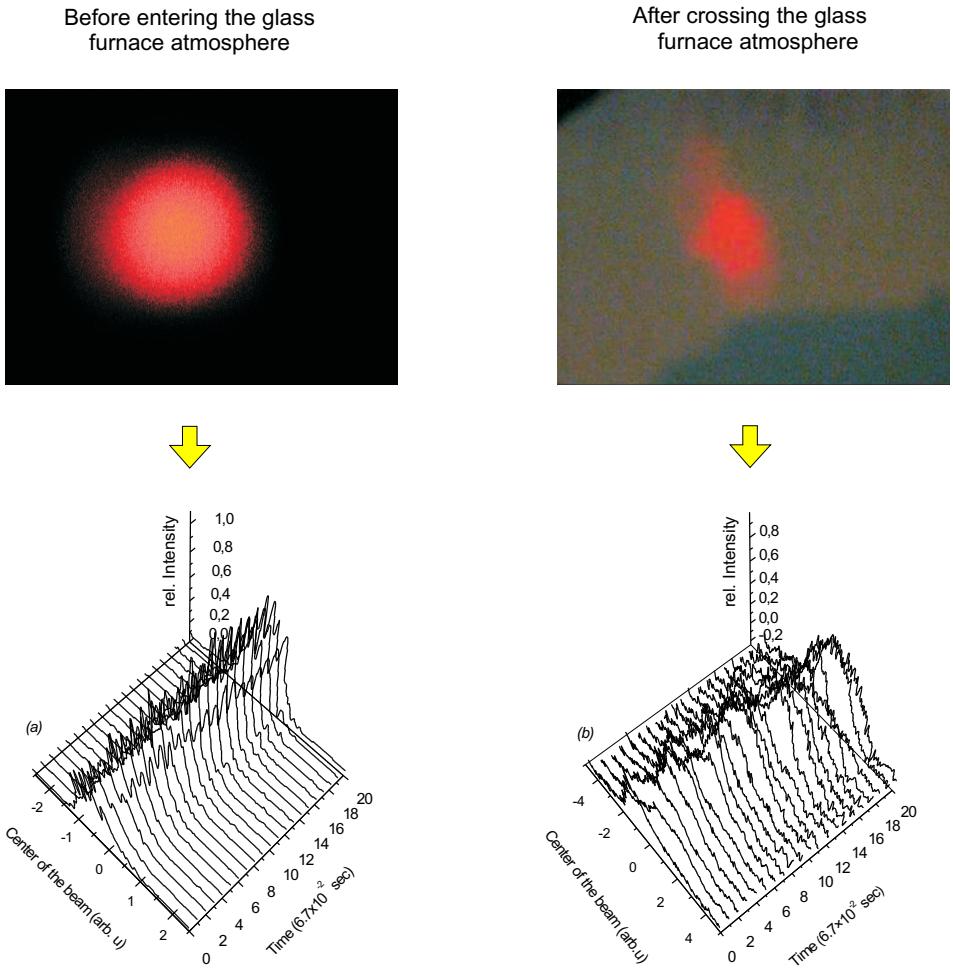

Figure 8.4: *Intensity fluctuations of the visible pump laser beam (a) before and (b) after crossing the recuperator channel of the furnace at* $T = 1100°C$.

Before entering the glass furnace atmosphere an average off-center fluctuation of $\pm 5\%$ is obtained (Figure 8.4a) while after passing the turbulent hot temperature atmosphere the fluctuation is $\pm 15\%$ (Figure 8.4b). This strong variation can be related to the strong refractive index variation of the atmosphere within the recuperator channel of the furnace[1]. The refractive index is both temperature and wavelength dependent. In the literature there are several equations given for the calculation of these dependencies [153, 154]. In this investigation the refractive index dispersion given by J. Owens (1967) [155] is used

[1]The thermal radiation of the glowing particles within the atmosphere of the furnace must also be taken into account. However, only the variations due to the refractive index variations can be considered analytically.

because in this formula the temperature values can be inserted directly. The wavelength dependence of the refractive index of the atmosphere within the furnace can be calculated by

$$[n(\lambda)-1]\times 10^8 = \left[A_1 + \frac{B_1}{C_1-\lambda^{-2}} + \frac{D_1}{E_1-\lambda^{-2}}\right] D_s + \left[A_2 + \frac{B_2}{\lambda^2} - \frac{C_2}{\lambda^4} + \frac{D_2}{\lambda^6}\right] D_w \quad (8.1)$$

where $A_1, ..., D_2$ are constant coefficients given in Table 8.1, and λ is the wavelength in microns.

Parameters	Values
A_1	2371.34
B_1	683939.7
C_1	130
D_1	4547.3
E_1	38.9
A_2	6487.31
B_2	58.058
C_2	0.71150
D_2	0.08851

Table 8.1: *The coefficients used in Equation (8.1) given by Reference [155].*

The temperature- and pressure-dependent parameters D_s and D_w are

$$\begin{aligned} D_s &= \frac{Ps}{T}\left[1 + P_s\left(a_s - \frac{b_s}{T} + \frac{c_s}{T^2}\right)\right] \\ D_w &= \frac{P_w}{T}\left\{1 + P_w\left[1 + a_w P_w\right]\left[b_w + \frac{c_w}{T} - \frac{d_w}{T^2} + \frac{a_w}{T^3}\right]\right\} \end{aligned} \quad (8.2)$$

the contributions of the water-free part and the water vapor to the refractive index of air, respectively. T is the absolute temperature. The corresponding parameters of Equation (8.2) are given in Table 8.2. P_w is the partial pressure of water in the air which can be calculated by the relative humidity rh (in percent) as

$$P_w = \frac{rh}{100} P_{sat.}$$

where $P_{sat.}$ is the saturation pressure of water. P_s is the partial pressure of the dry air and can be obtained from the atmospheric pressure P through

$$P_s = P - P_w.$$

Parameters	Values
a_s	57.90×10^{-8}
b_s	9.3250×10^{-4}
c_s	0.25844
a_w	3.7×10^{-4}
b_w	-2.37321×10^{-3}
c_w	2.23366
d_w	710.792
e_w	7.75141×10^{4}

Table 8.2: *The coefficients used in Equation (8.2).*

Although the measurements considered here were performed at a wavelength of 4.9 μm and Equation (8.1) covers only the spectral region up to 2.5 μm, it can be used to estimate the variation of the refractive index. The determination of the refractive index of the air in the NIR region (2.5 μm) yields in an estimated accuracy of 1.2×10^{-8}. Assuming a humidity of 50% within the atmosphere of the furnace and the atmospheric pressure a refractive index $n(\lambda) - 1 = 2.4 \times 10^{-4}$ results at 300 K and $n(\lambda) - 1 = 8.4 \times 10^{-6}$ at 1400 K for $\lambda = 2.5$ μm. It can be expected that the fluctuations of the laser beam due to the refractive index variation according to Equation (8.1) are less pronounced at higher wavelengths (e. g. at MIR wavelengths compared to visible wavelengths). The variation of the intensity of the MIR DFG laser is given in Figure 8.5 for 12 individual measurements after passing the glass furnace atmosphere.

Analyzing the transmitted intensity of the MIR DFG laser through the furnace indicates about 5% deviation from its maximum value which confirms less spectral fluctuation for the MIR laser during the measurement compared to the NIR pump diode-laser. This shows the advantage of using MIR wavelengths for in-situ probing of gas species in high temperature environments compared to NIR wavelengths.

Possible interferences with water absorption lines, which are always present in the atmosphere of the furnace, are also investigated. In the MIR spectral region around 4.94 μm and within the effective MIR DFG scanning range, only one strong water absorption line is present at 1100°C. It is centered at 2023.03 cm^{-1} with a line strength of 5.49×10^{-21} $\text{cm}^{-1}/(\text{molecule} \cdot \text{cm}^{-2})$ according to the HITRAN 2003 database. Even though the line strength of this water line is smaller than that of the CO P(28) absorption line by a factor of 13.6, the absorbance of the water line is stronger because of the high water concentration within the atmosphere of the glass furnace. Taking into account both the thermal-broadening and the pressure-broadening for the H_2O absorption line at 2023.03 cm^{-1} gives a pressure- and Doppler-broadening of $\Delta\bar{\nu}_{press.} = 0.015$ cm^{-1} and $\Delta\bar{\nu}_{Dopl.} =$

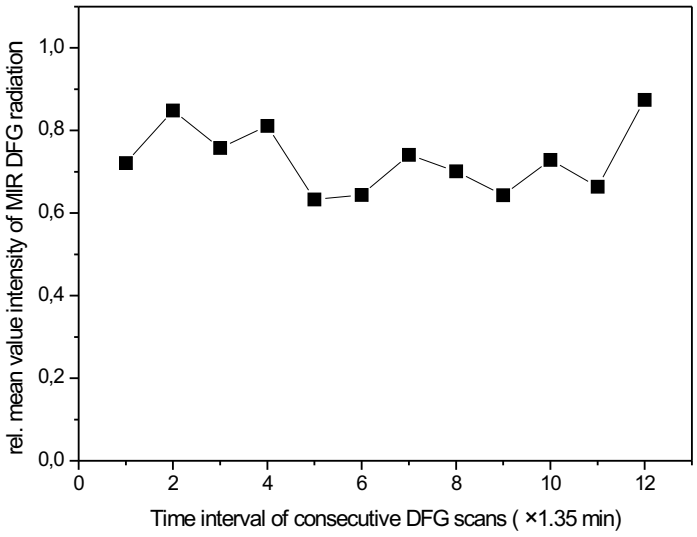

Figure 8.5: *Intensity variation of the MIR DFG light during 12 individual measurements.*

0.013 cm^{-1}, respectively. The parameters (e. g. line position, line strength, broadening coefficients, and temperature) which are obtained from the present measurement can be used in the equations for lineshape modelling in order to obtain the absorbance spectrum of the present species. The relative absorbance of the major molecular species as there are H_2O, CO and CO_2 of the glass furnace in the spectral range of interest are given in Figure 8.6.

Even though the CO P(28) line is not completely isolated from the line wings of the water absorption around 2023.03 cm^{-1} a CO line profile can be measured because of the narrow spectral linewidth of the present MIR DFG laser ($\sim 1.2 \times 10^{-2}$ cm^{-1}). Considering all loss mechanisms and noises, including scattering, the expansion of the beam cross section and the fluctuations due to the thermal effects, a transmitted MIR power of as low as $P \simeq 1$ nW can be detected and separated from the thermal noise using an InSb detector and lock-in technique (this equals 3.3% of the initial power). At the detector side the lock-in amplifier is set to 100 mV and 100 ms. Then the MIR DFG light is scanned over $\Delta\bar{\nu} = 1$ cm^{-1} and 12 MIR DFG scans of the CO P(28) absorption line are taken and averaged as shown in Figure 8.7. This averaging procedure was verified not to affect the spectral lineshape of CO P(28).

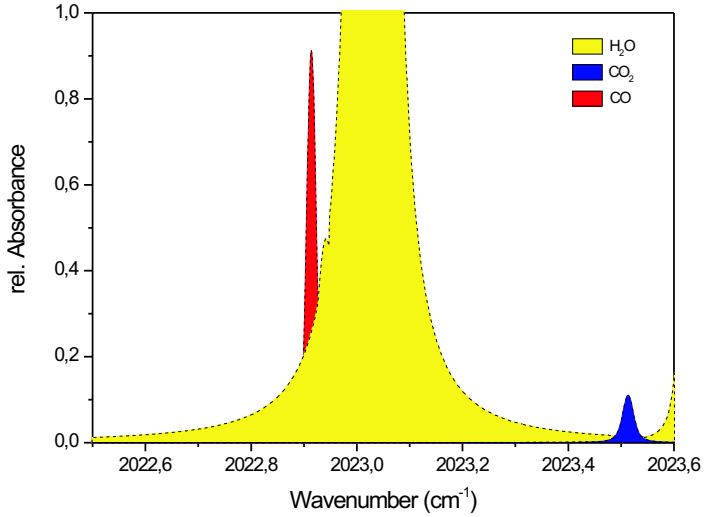

Figure 8.6: *Modelling of the relative absorbance of the typical combustion species within the atmosphere of the furnace for $T = 1400K$ and assuming 19.9% Vol. for H_2O, 13.2% Vol. for CO_2, and 0.04% Vol. for CO.*

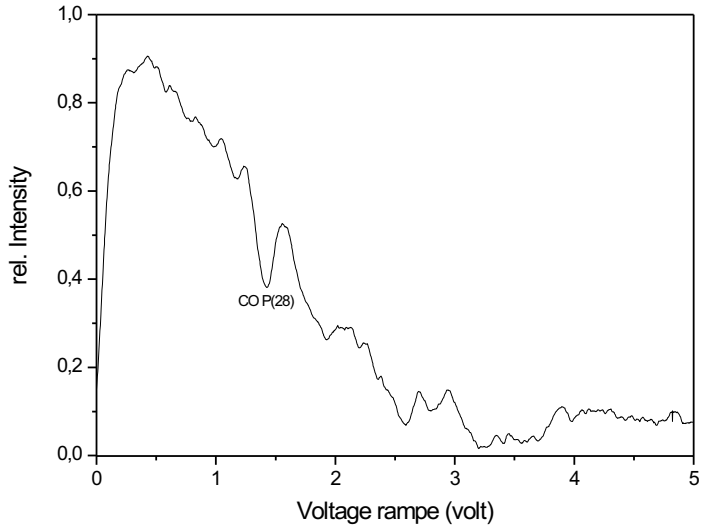

Figure 8.7: *Averaged CO P(28) line profile taken from 12 individual MIR DFG scans.*

The CO concentration in the glass furnace is obtained by fitting a Voigt profile to the background corrected CO line shape profile as indicated in Figure 8.8.

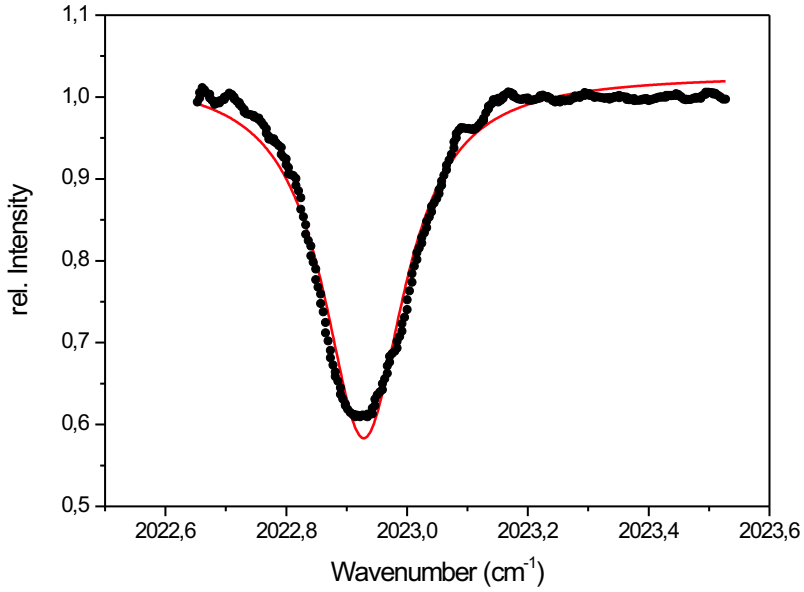

Figure 8.8: *Absorption spectra of the CO P(28) rotational line at 2022.914 cm^{-1} recorded in a 1 m path length of the glass furnace of GentheGlas company with 100 ms time constant for the lock-in amplifier. Solid line: fitted Voigt profile. Dots: average of 12 MIR DFG scan measurements.*

A concentration of about 400 ppm is obtained assuming a temperature $T = 1100°C$ that has been measured independently by conventional thermography. The above measured CO concentration is in agreement with a typical bypass measurements done by the "Hüttentechnische Vereinigung der Deutschen Glasindustrie".

9 Conclusion and outlook

In the present work we have reported a novel MIR DFG laser obtained in an $AgGaS_2$ nonlinear optical crystal. From this work, it has become clear that difference-frequency mixing of two cw diode-lasers as pump and signal sources in an $AgGaS_2$ nonlinear crystal for fast and accurate wavelength tuning is still a competitive laser source to other laser sources based on nonlinear processes like optical parametric oscillators and amplifiers and newly emerging, quantum cascade lasers. This holds especially with respect to high spectral resolution and room temperature operation. We have also demonstrated that this laser source is a well suited source for spectroscopic applications since it offers a narrow linewidth (less than 1.2×10^{-2} cm^{-1}) and a broad tuning range (more than 70 cm^{-1}).

This MIR DFG laser source is operated at room temperature and it covers the wavelength region within the strong absorption bands of the important combustion species such as CO and NO molecules. This allows to easily access absorption lines of each of those species for quantitative analysis at a spectral region that is free from interference with other absorbers, especially with water absorption lines since water is always present in high concentration in combustions. The realization of such MIR DFG laser source requires the technical modification of one of the input diode-lasers to avoid mode hops during tuning. This is done by building an external short-cavity around the diode-laser pump source of the DFG spectrometer. Such modification enables the tuning of the MIR DFG radiation in a wide mode hop free range (about 29 cm^{-1} for the DFG wavelength) at room temperature. The present results obtained for CO and NO measurements at room temperature are in good agreement with the reported values given in the HITRAN 2003 database which clearly confirms the performance of the MIR DFG laser for quantitative spectroscopy.

The obtained results for mapping CO concentrations using computerized tomographic reconstruction techniques in a methan/air flame of a standard McKenna flat flame burner not only provides a different application area of the present MIR DFG laser source but it also presents the availability of this kind of laser source to application in high temperature environments. This makes it the most important alternative to overtone spectroscopic techniques such as near-infrared absorption spectroscopy. The significant wavelength tuning range of the DFG spectrometer enables the detection of multiple CO absorption lines for additional temperature distribution measurements using the Boltzman distribution. The 2-dimensional CO concentration profiles derived by tomographic reconstruction performed 10 mm above the surface of the burner (2.5% Vol.) indicate a good agreement with prior 2-dimensional measurements that use conventional probe, infrared and LIF spectroscopic techniques as well as chemical-kinetic calculations.

During the work it has been proved that the present MIR DFG spectrometer fulfills the key requirements of a room temperature operated gas sensor such as reproducible and fast linear MIR wavelength scanning for precise monitoring of combustion systems. This is underlined by the fact that even though the output power of the present MIR DFG laser is as low as a few nW it provides considerable results. The excellent performance of this gas sensor is demonstrated by the on-line monitoring of the CO P(28) absorption line at $\bar{\nu} = 2022.914\ \mathrm{cm}^{-1}$ in a combustion. The CO concentration in the atmosphere of a gas fired glass melting furnace was measured to be 400 ppm. The previous determination of CO concentrations in the recuperator channel of the glass furnace provided by typical conventional bypass techniques represents a good agreement with our measured values. Even though the MIR DFG laser suffers from low output power it offers, in particular, good spatial and temporal resolution and does not influence the system since it operates in a nonintrusive mode. However, at least two apertures for optical access are required which is not always a trivial task to achieve in industrial environments.

Presently, the main drawback of applying the MIR DFG laser for combustion diagnostics is the low output power which is in the range of a few nW. To further increase the performance of the DFG spectrometer with respect to the output power more powerful pump and signal sources for the DFG mixing process are required. This can be achieved by either fiber and/or tapered amplifiers. Such experiments are in progress in our group. The main immediate advantage of this amplified DFG laser is the enhancement of the measurement speed which can be realized by splitting the MIR DFG laser output to a bundle of MIR fibers similar to diode-laser arrays as done in the near-infrared. Therefore, a full automated combustion diagnostic system with the interface of a computerized network can be set up on the base of an amplified MIR DFG laser source and as a consequence much of the systematic errors can be eliminated from the final results. The MIR DFG laser output power can be coupled into a fiber which can be used as evanescent-field fiber sensor as applied by Blanke et al. [84].

When an amplified pulsed Nd:YAG laser is mixed with an amplified diode-laser the resultant MIR DFG radiation can be used to image concentration profiles based on the light detection and ranging (LIDAR) technique. When a laser source with a pulse duration in the range of picoseconds is used a resolution of centimeters is achieved. Such LIDAR system is interesting particularly for the study of particle formations and distributions inside real combustion devices specially when there is only one optical access to the combustion chamber. The main task is to develop an appropriate detector system combined with a data analysis that allows LIDAR measurements with a space resolution in the range of centimeters. A picosecond LIDAR system based on a MIR DFG laser source is also in progress in our research group.

Another alternative for the output power enhancement of a MIR DFG laser is the use of a nonlinear crystal with higher nonlinearity. Quasi-phase matching in a periodically-poled $LiNbO_3$ (PPLN) nonlinear crystal provides both wide phase-matching bandwidth and fast wavelength tuning necessary for in-situ and on-line measurements of combustion chambers. However, the transparency range of a PPLN crystal is limited to about 4 μm and therefore such a MIR DFG laser could not be tuned over the spectral range centered around 5 μm where the strong absorption lines of NO molecules are present.

Presently, the unique properties of the MIR radiation based on DFG in $AgGaS_2$ such as a narrow linewidth (less than 0.01 cm^{-1}), and a broad tuning range of $\delta\bar{\nu} > 70$ cm^{-1} in the important λ = 4-5 μm spectral region make it very competitive to other MIR laser sources as there are OPO lasers and QC lasers for spectroscopic trace gas detection. The output power is sufficient for the detection of CO and NO molecules via their strong fundamental absorption lines while the system operates at room temperature. The device is portable but further miniaturization for in-situ and on-line sensing of combustion species can be achieved.

However, by application of an amplified MIR DFG laser the SNR is increased resulting in a higher sensitivity of the device. In combination with the strong absorption bands of nearly all molecules in the MIR region, the MIR DFG spectrometer is an excellent tool for remote sensing of industrial combustions nonintrusively.

Bibliography

[1] Y. R. Shen. A Few Selected Applications of Surface Nonlinear Optical Spectroscopy. *Proc. Natl. Acad. Sci. USA*, **93**(22), 12104–12111, 1996.

[2] J. Wolfrm. Advanced laser spectroscopy in combustion chemistry: From elementary steps to practical devices. *Faraday Discuss.*, **119**, 1–26, 2001.

[3] M. Reeves, P. V. Farrell, and M. P. Musculus. Demonstration of a two-photon confocal laser-induced fluorescense technique for the detection of nitric oxide in atmospheric pressure flows and hydrocarbon-air flames. *Meas. Sci. Technol.*, **10**, 285–294, 1999.

[4] U. Willer, D. Scheel, I. Kostjucenko, C. Bohling, W. Schade, E. Faber. Fiber-optic evanescent laser sensor for in-situ gas diagnostics. *Spectrochimica Acta Part A*, **58**, 2427–2432, 2002.

[5] J. Houston Miller. Comparison of Near and Mid-Infrared Tunable Diode Laser Absorption Spectroscopy for the Analysis of Combustion Gases. *Annual Conference on Fire Research, Maryland, November 2-5*, 19-20, 1998.

[6] Peter Werle. A review of recent advances in semiconductor laser based gas monitors. *Spectroscopica Acta Part A*, **54**, 197–236, 1998.

[7] S.Cheskis, I. Derzy, V. A. Lozovsky, A. Kachanov, D. Romanini. Cavity ring-down spectoscopy of OH radicals in low pressure flame. *Appl. Phys. B*, **66**, 377–381, 1998.

[8] G. Engel, W. B. Yan, J. Dudek, K. K. Lehmann, and P. Robinowitz. Ring down spectroscopy with a Brewster's angle prism resonator. *in Laser Spectroscopy XIV International Conference*, 314-315, 1999.

[9] Frank K. Tittel, Dirk Richter, and Alan Fried. Mid-Infrared Laser Applications in Spectroscopy. *Topics Appl. Phys.*, **89**, 445–516, 2003.

[10] R. F. Curl and Frank K. Tittel. Tunable infrared laser spectroscopy. *Annu. Rep. Prog. Chem. Sect. C*, **98**, 1–56, 2002.

[11] A. A. Kosterev, R. F. Curl, F. K. Tittel, M. Beck, D. Hofstetter, J. Faist. Chemical sensing with pulsed QC-DFB lasers operating at 15.6 μm. *Appl. Phys. B*, **75**, 351–357, 2002.

[12] A. Barken, F. K. Tittel, D. M. Mittleman, R. Dengler, P. H. Siegel, G. Scalari, L. Ajili, J. Faist, H. E. Beere, E. H. Linfield, A. G. Davies, D. A. Ritchie. Linewidth tuning and characteristics of THz quantum cascade laser. *Optice Letters*, **6**, 575–577, 2004.

[13] R. G. Smith, J. E. Geusic, H. J. Levinstein, J. J. Rubin, S. Singh, and Van Uitert. Continuous Optical Parametric Oscillations in $Ba_2NaNb_5O_{15}$. *Appl. Phys. Lett.*, **12**, 308–310, 1968.

[14] M. Ebrahimzadeh und M. H. Dunn. *Optical Parametric Oscillators.* In Handbook of Optics IV, Optical Society of America. McGraw Hill Press, 2001.

[15] D. Richter, A. Fried, B. P. Wert, J. G. Walega and F. K. Tittel. Development of a tunable mid-IR difference frequency laser source for highly sensitive airborne trace gas detection. *Appl. Phys. B*, **75**, 281–288, 2002.

[16] D. Richter, D. G. Lancaster, R. F. Curl, W. Neu, F. K. Tittel. Compact mid-infrared trace gas sensor based on difference-frequency generation of two diode lasers in periodically poled $LiNbO_3$. *Appl. Phys. B*, **67**, 347–350, 1998.

[17] Leonard I. Schiff. *Quantum Mechanics.* McGraw-Hill, 1968.

[18] Chung L. Tang. *Nonlinear Optics.* In Handbook of Optics V, Optical Society of America. McGraw Hill Press, 2001.

[19] A. Thorne, U. Litzen, S. Johansson. *Spectrophysics, Principles and Applications.* Springer, 1999.

[20] Mitchel Weissbluth. *Atoms and Molecules.* Academic Press, 1978.

[21] N. Bloembergen. *Nonlinear Optics.* W. A. Benjamin, INC., 1965.

[22] Amnon Yariv. *Quantum Electronics.* John Wiley and Sons, 1975.

[23] Y. R. Shen. *Nonlinear infrared generation, Vol. 16.* Springer, 1977.

[24] D. Boucher W. Chen und F. K. Tittel. Recent advances in continuous-wave laser difference-frequency generation in the mid-infrared: State of the art, applications, and perspectives. *Recent. Res. Devel. Appl. Phys.*, **5**, 27–68, 2002.

[25] F. Zernike. *Nonlinear Optical devices: in Methods of experimental physics, Vol. 15.* Academic Press, New York, 1979.

[26] Richard L. Sutherland. *Handbook of nonlinear optics.* Marcel Dekker, 1996.

[27] G. C. Bhar. A system review of infrared upconversion. *Indian Journal of Pure and Applied Physics*, **33**, 169–178, 1995.

[28] G. C. Bhar und U. Chatterjee. Analysis of phase-matching for noncollinear three-wave mixing in uniaxial crystals. *Jpn. J. Appl. Phys.*, **29**(6), 1103–1107, 1990.

[29] S. Das G. C. Bhar und U. Chatterjee. Noncollinear phase-matched second-harmonic generation in beta barium borate. *Appl. Phys. Lett.*, **54**(15), 1383–1384, 1989.

[30] A. Yariv. *Optical Electronics in Modern Communications*. Oxford University Press. Fifth edition, 1997.

[31] Y. R. Shen. *Principles of Nonlinear Optics*. John Wiley and Sons, New York, 1984.

[32] G. G. Gurzadyan V. G. Dimitriev und D. N. Nikogosyan. *Handbook of Nonlinear Optical Crystals*. Springer, 1997.

[33] J. E. Midwinter und J. Warner. The effects of phase matching method and of uniaxial symmetry on the polar distribution of second-order nonlinear optical polarization. *BRIT. J. Appl. Phys.*, **16**, 1135–1142, 1965.

[34] J. A. Giordmaine. Mixing of light beams in crystals. *Phys. Rev. Lett.*, **8**(1), 19–20, 1962.

[35] X. Zhang. *High-repetition-rate femtosecond Optical Parametric Oscillation Based on KTP and PPLN*. Dissertation, Philips-Universität Marburg, 2002.

[36] G. C. Bhar and G. C. Ghosh. Dispersion of thermooptic coefficients in nonlinear crystals. *Appl. Opt.*, **19**(7), 1029–1031, 1980.

[37] V. Petrov and F. Rotermund. Application of the solid solution $Cd_xHg_{1-x}Ga_2S_4$ as a nonlinear optical crystal. *Opt. Lett.*, **27**(19), 1705–1707, 2002.

[38] Robert D. Guenther. *Modern Optics*. John Wiley and sons, 1990.

[39] V. Petrov, F. Rotermund, and F. Noack. Generation of high-power femtosecond light pulses at 1 kHz in the mid-infrared spectral range between 3 and 12 μm by second-order nonlinear processes in optical crystals. *J. Opt. A: Pure Appl. Opt.*, **3**, R1–R19, 2001.

[40] Douglas L. Miller. *Nonlinear Optics*. Springer, 1998.

[41] N. Bloembergen. Conservation laws in nonlinear optics. *J. Opt. Soc. Am.*, **70**(12), 1429–1436, 1980.

[42] D. Richter, M. Erdelyi, R. F. Curl, F. K. Tittel, C. Oppenheimer, H. J. Duffell, M. Burton. Filed measurements of volcanic gases using tunable diode laser based mid-infrared and fourier transform infrared spectrometers. *Optics and Lasers in Engineering*, **37**, 171–186, 2002.

[43] G. D. Boyd and D. A. Kleinman. Parametric interaction of focused gaussian light beams. *J. Appl. Phys.*, **39**(8), 3597–3640, 1968.

[44] A. S. Pine. Doppler-limited molecular spectroscopy by difference-frequency mixing. *J. Opt. Soc. Am.*, **64**, 1683, 1974.

[45] Ulrike Willer. *NIR- und MIR-Evaneszenzfeldlasersensoren-Grundlagen und Anwendungen.* Dissertation, Technische Universität Clausthal, 2001.

[46] P. Canarelli, Z. Benko, A. H. Hielscher, R. F. Curl, and F. K. Tittel. Measurement of Nonlinear Coefficient and Phase Matching Characteristics of $AgGaS_2$. *IEEE J. of Quantum Electronics*, **28**(1), 52–55, 1992.

[47] A. Harasaki and K. Kato. New Data on the Nonlinear Optical Constant, Phase-Matching, and Optical Damage of $AgGaS_2$. *Jpn. J. Appl. Phys.*, **36, Part 1**(2), 700–703, 1997.

[48] P. Canerelli, Z. Benko, R. Curl, and F. K. Tittel. Continuous-wave infrared laser spectrometer based on difference frequency generation in $AgGaS_2$ for high-resolution spectroscopy. *J. Opt. Soc. Am. B*, **9**(2), 197–202, 1992.

[49] D. C. Hanna, V. V. Rample, and R. C. Smith. Tunable infrared down-conversion in silver thiogallate. *Optics Communications*, **8**(2), 151–153, 1973.

[50] U. Simon, S. Waltman, I. Loa and F. K. Tittel, L. Hollberg. External-cavity difference-frequency source near 3.2 μm, based on combining a tunable diode laser with a diode-pumped Nd:YAG laser in $AgGaS_2$. *J. Opt. Soc. Am. B*, **12**(2), 323–327, 1995.

[51] U. Willer, T. Blanke, and W. Schade. Difference frequency generation in $AgGaS_2$: Sellmeier and temperature-dispersion equations. *Appl. Opt.*, **40**(30), 5439–5445, 2001.

[52] D. S. Chemla, P. J. Kupecek, D. S. Robertson, and R. C. Smith. Silver thiogallate: a new material with potential for infrared device. *Opt. Commun.*, **3**, 29–31, 1971.

[53] G. C. Bhar and R. C. Smith. Silver thiogallate ($AgGaS_2$) part II: linear optical properties. *IEEE J. Quantum Electron.*, **QE-10**, 546–550, 1974.

[54] Y. X. Fan, R. C. Eckardt, R. L. Byer, R. K. Route, and R. S. Feigelson. $AgGaS_2$ infrared parametric oscillator. *Appl. Phys. Lett.*, **45**, 313–315, 1984.

[55] K. Kato. High-Power Difference-Frequency Generation at 5-11 μm in $AgGaS_2$. *IEEE J. of Quantum Electronics*, **QE-20**(7), 698, 1984.

[56] G. C. Bhar, S. Das, D. K. Ghosh, and L. S. Samanta. Phase-matching of infrared nonlinear laser devices using ($AgGaS_2$). *IEEE J. Quantum Electron.*, **QE-24**, 1492–1494, 1988.

[57] David A. Roberts. Dispersion equations for nonlinear optical crystals: KDP, $AgGaSe_2$, and $AgGaS_2$. *Appl. Opt.*, **35**(24), 4677–4688, 1996.

[58] E. Takaoka and K. Kato. Thermo-optic dispersion formula for $AgGaS_2$. *Appl. Opt.*, **38**(21), 4577–4580, 1999.

[59] G. C. Bhar, D. K. Ghosh. P. S. Ghosh, and D. schmitt. Temperature effects in $AgGaS_2$ nonlinear devices. *Appl. Opt.*, **22**, 2492–2494, 1983.

[60] Colin N. Banwell and Elaine M. McCash. *Fundamentals of molecular spectroscopy.* fourth edition, McGraw-Hill, 1994.

[61] Marcelo Alonso and Edward J. Finn. *Physics.* Addison-Wesely, 1970.

[62] C. Chackerian, and R. H. Tipping. Vibrational-Rotational and Rotational intensities for CO Isotops. *J. of Molecular Spectroscopy*, **99**, 431–449, 1983.

[63] M. Snels, C. Corsi, F. D. Amato, M. De Rosa, G. Madugno. Pressure broadening in the second overtone of NO, measured with a near infrared DFB diode laser. *Optics communications*, **159**, 80–83, 1999.

[64] A. Goldman and S. C. Schmidt. Infrared spectral line parameters and absorbance calculations of NO at atmospheric and elevated temperature for the $\Delta v = 1$ bands region. *J. Quant. Spectrosc. Radiat. Transfer*, **15**, 127–138, 1975.

[65] W. Demtröder. *Laser Spectroscopy.* Springer, 2004.

[66] D. Rahle, D. Leleux, M. Erdelyi, F. Tittel, M. Fraser, S. Friedfeld. Ambient formaldehyde detection with a laser spectrometer based on difference-frequency generation in PPLN. *Appl. Phys. B*, **72**, 947–952, 2001.

[67] J. Y. Wang. Laser absorption methods for simultaneous determination of temparature and species concentrations through a cross section of a radiating flow. *Appl. Opt.*, **15**(3), 768–773, 1976.

[68] S. Chandra, V. U. Maheshwari, and A. K. Sharma. Einstein A-Coefficients for vibrotational transitions in CO. *Astron. Astrophys. Suppl. Ser.*, **117**, 557–559, 1996.

[69] S. Gasiorewicz. *Quantum mechanics.* John Wiley, 1974.

[70] Jeffrey N-P. Sun and Peter R. Griffiths. Temperature dependence of the self-broadening coefficients for the fundamental band of carbon monoxide. *Appl. Opt.*, **20**(9), 1691–1695, 1981.

[71] T. Nakazawa and M. Tanaka. Intensities, half-widths and shapes of spectral lines in the fundamental band of CO at low temperatures. *J. Quant. Spectrosc. Radiat. Transfer*, **28**(6), 471–480, 1982.

[72] Torsten Blanke. *Differenzfrequenz-Lasersystem für die hochauflösende MIR-Absorptionsspektroskopie.* Dissertation, Technische Universität Clausthal, 2001.

[73] U. Simon and F. K. Tittel. Recent progress in tunable nonlinear optical devices for infrared spectroscopy. *Infrared Phys. Technol.*, **36**(1), 427–437, 1995.

[74] N. Saito, K. Akagawa, S. Wada, H. Tashiro. Difference-frequency generation by mixing dual-wavelength pulses emitting from an elactronically tuned Ti:saphhire laser. *Appl. Phys. B 69*, 93-97, 1999.

[75] D. Lee, T. Kaing, J. J. Zondy. An all-diode-laser-based, dual-cavity $AgGaS_2$ cw difference-frequency source for the 9-11 μm range. *Appl. Phys. B 67*, Seiten 363–367, 1998.

[76] A. H. Hielscher, C. E. Miller, D. C. Bayard, U. Simon, K. P. Smolka, R. F. Curl, and F. K. Tittel. Optimization of a midinfrared high-resolution difference-frequency laser spectrometer. *J. Opt. Soc. Am. B*, **9**(11), 1962–1967, 1992.

[77] U. Simon and F. K. Tittel, L. Goldberg. Difference-frequency mixing in $AgGaS_2$ by use of high-power GaAlAs tapered semiconductor amplifier at 860 nm. *Opt. Lett.*, **18**(22), 1931–1933, 1993.

[78] U. Simon, C. E. Miller, C. C Bradley, R. G. Hulet, R. F. Curl, and F. K. Tittel. Difference-frequency mixing in $AgGaS_2$ by use of single-mode diode-laser pump sources. *Opt. Lett.*, **18**(13), 1062–1064, 1993.

[79] R. J. Seymour and F. Zernike. Infrared radiation tunable from 5.5 to 18.3 μm generated by mixing in $AgGaS_2$. *Appl. Phys. Lett.*, **29**(11), 705–707, 1976.

[80] S. Haidar, K. Nakamura, E. Niwa, K. Masumoto, and H. Ito. Mid-infrared (5-12 μm) and limited (5.5-8.5 μm) single-knob tuning generated by difference-frequency-mixing in single crystal $AgGaS_2$. *Appl. Opt.*, **38**, 1798–1801, 1999.

[81] S. Haidar, E. Niwa, K. Masumoto, and H. Ito. Temperature tuning of 5-12 μm by difference frequency mixing of OPO outputs in a $AgGaS_2$ crystal. *J. of Phys. D: Applied Physics*, **36**, 1071–1074, 2003.

[82] H. D. Kronfeldt, G. Basar, and B. Sumpf. Application of a cw tunable infrared spectrometer based on difference-frequency generation in $AgGaS_2$ for self-broadening investigations of NO at 5 μm. *J. Opt. Soc. Am.*, **13**(9), 1859–1863, 1996.

[83] V. Petrov, C. Rempel, K. P. Stolberg, and W. Schade. Widely tunable continous-wave mid-infrared laser source based on difference-frequency generation in $AgGaS_2$. *Appl. Opt.*, **37**(21), 4925–4928, 1998.

[84] T. Blanke, U. Willer, and W. Schade. Spectroscopic applications of a widely tunable (6.8-12.5 μm) cw-DFG-laser spectrometer. *SPIE*, **3821**, 136–144, 1999.

[85] W. Schade, T. Blanke, U. Willer, C. Rempel. Compact tunable mid-infrared laser source by difference frequency generation of two diode-lasers. *Appl. Phys. B*, **63**, 99–102, 1996.

[86] B. Sumpf, T. Kelz, M. Nägele, H. D. Kronfeldt. A cw $AgGaS_2$ difference frequency spectrometer with diode lasers as pump sources. *Appl. Phys. B*, **64**, 521–524, 1997.

[87] J. Limpert, H. Zelimer, A. Tünnermann, D. G. Lancaster, R. Winder, D. Richter, and F. K. Tittel. Tunable continuous wave DFG-based gas sensor using fiber amplifier 1.5 μm external cavity diode laser and high power 1 μm diode laser. *Elect. Lett.*, **36**(20), 1739–1741, 2000.

[88] N. Matsuoka, S. Yamaguchi, K. Nanri, T. Fujioka, D. Richter, and F. K. Tittel. Yb Fiber Laser Pumped Mid-IR Source Based on Difference Frequency Generation and Its Application to Ammonia Detection. *Jpn. J. Appl. Phys.*, **40. Part 1**(2A), 625–628, 2001.

[89] L. Goldberg, W. K. Burns, R. W. McElhanon. Wide acceptance bandwidth difference frequency generartion in quasi-phase-matched $LiNbO_3$. *Appl. Phys. Lett.*, **67**(20), 2910–2912, 1995.

[90] M. Seiter, D. Keller, M. W. Sigrist. Broadly tunable difference-frequency spectrometer for trace gas detection with noncollinear critical phase-matching in $LiNbO_3$. *Appl. Phys. B*, **67**, 351–356, 1998.

[91] D. G. Lancaster, D. Richter, R. F. Curl, and F. K. Tittel, L. Goldberg and J. Koplow. High-power continuous-wave mid-infrared radiation generated by difference frequency mixing of diode-laser fiber amplifiers and its application to dual-beam spectroscopy. *Opt. Lett.*, **24**(23), 1744–1746, 1999.

[92] K. P. Petrov, R. F. Curl, and F. K. Tittel, L. Goldberg. Continuous-wave tunable 8.7 μm spectroscopic source pumped by fiber-coupled communications laser. *Opt. Lett.*, **21**(18), 1451–1453, 1996.

[93] K. S. Abedin, S. Haidar, Y. Konno, C. Takyu, and H. Ito. Difference frequency generation of 5-18 μm in a $AgGaSe_2$ crystal. *Appl. Opt.*, **37**(9), 1642–1646, 1998.

[94] R. A. Kaindl, D. C. Smith, M, Joschko, M. P. Hasselbeck, M. Woerner, and T. Elsaesser. Femtosecond infrared pulses tunable from 9 to 18 μm at an 88-MHz reretition rate. *Opt. Lett.*, **23**(11), 861–863, 1998.

[95] W. Chen, F. Cazier, D. Boucher, F. K. Tittel, and P. B. Davies. Trace Gas Absorption Spectroscopy Using Laser Difference-Frequency Spectrometer for Environmental Application. *Laser Physics*, **11**(5), 594–599, 2001.

[96] K. Shimoda. *Introduction to Laser Physics*. Second Edition, Springer, 1986.

[97] Peter Geiser. *Pikosekunden-MIR-DFG-Lasersystem-Aufbau und Charakterisierung*. Diplomarbeit, Technischen Universität Clausthal, 2002.

[98] Irina Kostjučenko. *Laserabsorptions- und Eveneszenzfeldspektroskopie an Fumarolengasen*. Diplomarbeit, Technische Universität Clausthal, 2002.

[99] Mark G. Allen. Diode laser absorption sensors for gas-dynamic and combustion flows. *Meas. Sci. Technol.*, **9**, 545–562, 1998.

[100] SCHÄFER&KIRCHHOFF. Hamburg. Produktkatalog. 1996.

[101] J. A. Jamieson, R. H. McFee, G. N. Plass, R. H. Grube, R. G. Richards. *Infrared Physics and Engineering*. McGraw-Hill, 1963.

[102] A. Rogalski and K. Chrzanowski. Infrared Devices and techniques. *Opto-Electronics Review*, **10**(2), 111–136, 2002.

[103] Polytech GmbH, Waldbronn-Karlsruhe. *Data Sheet : 'InSb Detector'*, 1993.

[104] Korth Kristalle GmbH, Altenholz (Kiel). *http://www.korth.de*.

[105] M. L. Meade. *Lock-in amplifiers: principles and applications*. Peter Peregrinus Ltd., 1983.

[106] L. S. Rothman et al. The HITRAN molecular spectroscopic database: edition of 2000 including updates through 2001. *J. Quant. Spectrosc. Radiat. Trans.*, **82**, 5–44, 2003.

[107] Quang-Viet Nguyen. *The Application of Laser Diagnostics to the Measurement of Concentration and Temperature in Practical Methane-Air Flames*. Dissertation, University of California at Berkeley, 1995.

[108] S. Prucker, W. Meier, and W. Stricker. A flat flame burner as calibration source for combustion research: temperature and species concentrations of premixed H_2/air flames. *Rev. Sci. Instum*, **65**(9), 2908–2911, 1994.

[109] A. J. Faber and R. Kock. High temperature in-situ IR laser absorption CO-sensor for combustion control. *10th international symposium on applications of lasers*, **10-13 July**, 2000.

[110] Laser Components GmbH. *http:/www.lasercomponents.de*, 2002.

[111] Laser Components GmbH. **Data Sheet**, 2002.

[112] S. J. Carey, H. McCann, D. E. Winterbone, and E. Clough. Near Infrared Absorption Tomography for Measurement of Chemical Species Distribution. *1st World Congress on Industrial Process Technology, April 14-17*, Seiten 480–487, 1999.

[113] D. W. Watt, T. D. Upton, M. C. Merry, and D. D. Verhoeven. Emission Tomography of Premixed Hydrogen-Air Flames. *9th International symposium of Flow Visualization*, (314), 2000.

[114] Carreia D. P. Ferrão and A. Caldeira-Pires. Advanced 3D emission tomography flame temperature sensor. *Paper in Instituto Superior Tecnico, Mechanical Engineering Department*, 1-19, 1999.

[115] Y. Sivathanu, J. Lim, V. Narayanan, R. Joseph. Fan Beam Emission Tomography for Transient Fires. *Sixth International Microgravity Combustion Workshop*, **NASA Glenn Research Center**, 369–372, 2001.

[116] S. T. Sanders, J. A. Baldwin, T. P. Jenkins, D. S. Baer, and R. K. Hanson. Diode-laser sensor for monitoring multiple combustion parameters in pulse detonation engines. *Proceedings of the combustion Institute*, **28**, 587–594, 2000.

[117] R. M. Mihalcea, M. E. Webber, D. S. Baer, R. K. Hanson, G. S. Feller, W. B. Chapman. Diode-laser absorption measurements of CO_2, H_2O, N_2O, and NH_3 near 2.0 μm. *Appl. Phys. B*, **67**, 283–288, 1998.

[118] A. Soufiani, J. P. Martin, J. C. Rolon, L. Brenez. Sensitivity of temperature and concentration measurements in hot gases from FTIR emission spectroscopy. *J. Quant. Spectrosc. Radiat. Trans.*, **73**, 317–327, 2002.

[119] Michael Schneider. *Studies for neutron tomography.* Diploma thesis, University of Heidelberg, 2001.

[120] Brian J. Kirby and Ronald K. Hanson. Infrared PLIF Imaging of Gaseous Flows. *36th AIAA Aerospace Sciences, Reno, NV*, **AIAA 98-0307**, 1998.

[121] Brian J. Kirby and Ronald K. Hanson. Infrared PLIF Imaging of CO and CO_2. *37th AIAA Aerospace Sciences, Reno, NV*, **AIAA 99-0775**, 1999.

[122] J. Ji and J. Gore. Proceedings of JPGC'01. *International joint power generation conference*, 2001.

[123] Joachim Hussong. *H_2 Q-Zweig CARS-Thermometrie bei hohem Druck.* Doktor-ingenieurs, Deutsches Zentrum für Luft-und Raumfahrt eV., 2002.

[124] X. Zhou, X. Liu, J. B. Jeffries, and R. K. Hanson. Development of a sensor for temperature and water vapor concentration in combustion gases using a single tunable diode laser. *Meas. Sci. Technol.*, **14**(3), 1459–1468, 2003.

[125] S. Cheskis, A. Kachanov, M. Chenevier, F. Stoeckel. Temperature measurements in flames using water molecule overtone spectra detected by intracavity laser absorption spectroscopy. *Appl. Phys. B*, **64**, 173–716, 1997.

[126] Kraig B. Winters and Daniel Rouseff. A filtered backprojection method for the tomographic reconstruction of fluid velocity. *Inverse Problems*, **6**, L33–L38, 1990.

[127] R. K. Hanson and P. K. Falcone. Temperature measurement technique for high-temperature gases using a tunable diode laser. *Appl. Opt.*, **17**(16), 2477–2480, 1978.

[128] J. H. Miller, S. Elreedy, B. Ahvazi, and P. Hassanzadeh. Tunable diode-laser measurement of carbon monoxide concentration and temperature in a laminar methane-air diffusion flame. *Appl. Opt.*, **32**(30), 6082–6089, 1993.

[129] A. Y. Chang, E. C. Rea, Jr., and R. K. Hanson . Temperature measurements in shock tubes using a laser-diode absorption technique. *Appl. Opt.*, **26**(5), 885–891, 1987.

[130] X. Ouyang and P. L. Varghese . Selection of spectral lines for combustion diagnostics. *Appl. Opt.*, **29**(33), 4884–4890, 1990.

[131] S. Linow, S. D. Dreizler, J. Janicka . Comparison of two photon excitation schemes for CO detection in flames. *Appl. Phys. B*, **71**, 689–696, 2000.

[132] K. Seshadri, X. S. Bai, H. Pitsch . Asymptotic Structure of Rich Flames. *Combustion and Flame*, **127**, 2265–2277, 2001.

[133] H. Shimizu, K. Kumada, N. Yamanaka, N. Iwai, T. Mukaihara, and A. Kasukawa. Extremely Low Threshold 1.3 μm InAsP n-Type Modulation Doped MQW lasers. *Furukawa Review*, **19**, 149–154, 2000.

[134] D. L. Boiko, E. LeCren, G. M. Stephan, and P. Besnard. Spectrum of Vertical-Cavity Surface-Emitted Lasers: Linewidth properties and non-degenerate of relaxation oscillation frequencies. *J. Opt. B: Quantum Semiclass. Opt.*, **3**, S166–S172, 2001.

[135] N. A. Morris, J. C. Connolly, R. U. Martinelli, J. H. Abeles,, and A. L. Cook. Single-mode distributed-feedback 761 nm GaAs-AlGaAs quantum well lasers. *IEEE Photon. Technol. Lett.*, **7**, 455–457, 1995.

[136] H. Wenzel, A. Klehr, M. Bugge, G. Erbert, J. Fricke, A. Knauer, M. Weyers, and G. Tränkle. High-power 783 nm distributed-feedback laser. *Electr. Lett.*, **40**(2), 2004.

[137] Joel A. Silver and Daniel J. Kane. Diode laser measurements of concentration and temperature in microgravity combustion. *Meas. Sci. Technol.*, **10**, 845–852, 1999.

[138] M. L. Majewski, J. Barton, L. A. Coldren, Y. Akulova, and M. C. Larson. Widely Tunable Directly Modulated Sampled-Grating DBR Lasers. *Proc. OFC 2002, Anaheim, California (March 17-22)*, Paper No. ThV2, 2002.

[139] C. J. Howthorn, K. P. Weber, and R. E. Scholten . Littrow configuration tunable external cavity diode laser with fixed direction output beam. *Review of Scientific Instruments*, **27**(12), 4477–4479, 2001.

[140] S. Lecomte, E. Fretel, G. Mileti, and P. Thomann. Self-aligned extended-cavity diode laser stabilized by the Zeeman effect on the cesium D_2 line. *Appl. Opt*, **39**, 1426–1429, 2000.

[141] E. Schlosser, J. Wolfrum, L. Hildebrandt, H. Seifert, B. Oser, V. Ebert. Diode laser based in-situ detection of alkali atoms: Development of a new method for determination of residence-time distribution in combustion plants. *Appl. Phys. B*, **75**, 237–247, 2002.

[142] M. Breede, S. Hoffman, J. Zimmermann, J. Struckmeier, M. Hofmann, T. Kleine-Ostmann, P. Knobloch, M. Koch, J. P. Meyn, M. Matus, S. W. Koch, J. V. Moloney. Fourier-transform external cavity laser. *Optics Communications*, **207**, 261–271, 2002.

[143] E. Hecht. *Optik*. R. Oldenboug Verlag, 1999.

[144] S. D. Wehe, D. M. Sonnenfroh, M. G. Allen, C. Gmachl, F. Capasso. In-situ flame measurements of NO and CO using Mid-IR QC lasers. *in OSA "Trends in Optics and Photonics (TOPS)", Opt. Soc. Am., Washington DC*, **64**, FC3–1, 2002.

[145] T. Nakazawa and M. Tanaka. Measurements of intensities and self- and foreign-gas-broadened half-widths of spectral lines in the CO fundamental bands. *J. Quant. Spectrosc. Radiat. Transfer*, **28**(5), 409–416, 1982.

[146] A. J. Faber and R. Beerkens. Sensors for glass melting processes. *Glastech. Ber. Glass. Sci. Technol.*, **73C**$_2$, 2000.

[147] I. Linnerud, P. Kaspersen, T. Jaeger. Gas monitoring in the process industry using diode laser spectroscopy. *Appl. Phys. B*, **67**, 297–305, 1998.

[148] R. Beerkens and A. J. Faber. CO sensors for glass melting process. *Abstracts 6th international conference; Advances in fusion and processing of glass*, 69-72, 2000.

[149] M. Webber, R. Claps, F. V. Englich, F. K. Tittel, J. B. Jeffries, and R. K. Tittel. Measurements of NH_3 and CO_2 with distributed-feedback diode-laser near 2.0 μm in bioreactor vent gases. *Appl. Opt.*, **40**(24), 4395–4403, 2001.

[150] A. A. Kosterev and F. K. Tittel. Chemical Sensors Based on Quantum Cascade Lasers. *IEEE J. Quantum Electronics*, **38**(6), 582–592, 2002.

[151] S. D. Wehe, M. Allen, X. Liu, J. B. Jeffries, and R. K. Hanson. NO and CO apsorption measurements with mid-IR quantum cascade laser for engine exhaust applications. *Paper AIAA 2003-0588 at 41th Aerospace Sciences Meeting, Reno. NV, January*, 2003.

[152] L. Menzel, A. A. Kosterov, R. F. Curl, F. K. Tittel, C. Gmachl, F. Capasso, D. L. Sivco, J. N. Baillargeon, A. L. Hutchinson, A. Y. Cho, W. Urban. Spectroscopic detection of biological NO with a quantum cascade laser. *Appl. Phys. B*, **72**, 859–863, 2001.

[153] P. E. Ciddor. Refractive index of air: New equations for visible and near infrared. *Appl. Opt.*, **35**(9), 1566, 1996.

[154] P. E. Ciddor and R. J. Hill. Refractive index of air. 2. Group index. *Appl. Opt.*, **38**(9), 1663, 1999.

[155] J. C. Owens. Optical refractive index of air: Dependences on pressure, temperature and composition. *Appl. Opt.*, **6**(1), 51–59, 1967.

Acknowledgements

Writing a dissertation is only successful through a lot of collaboration and discussion with other people in a group. I would like to thank to all members of our group during the three years I spent in TUC for providing a friendly atmosphere.

First of all, my sincere and deepest thanks to Prof. Dr. Wolfgang Schade for his strong support and his friendly assistance. He has taught me the way how to focus on the research and being serious in working to achieve good results. He offered me an ideal scientific atmosphere and helped me to gain a knowledge and ability beyond the reach of many attainments. Besides, he has been a great friend to me.

I would like to thank my family for all their support, despite not really knowing what I do; To my patient and affectionate wife, Maryam, for providing encouragement to help me get through many hard days; To my lovely children Mohsen, Mahdieh, and Hoda who gave me great comfort and delightful times.

During this dissertation, I had an excellent opportunity to collaborate with Dr. Ulrike Willer. I would like to express my best thanks to her since I have profited much from the numerous friendly and fruitful discussion with her. It was of my pleasure to work with her.

I am grateful to Dr. Klaus Faulian for the supporting discussion, more or less related to my work.

I wish to express my gratitude to Frau Ingrid Nietzel for her strong support during our staying in Clausthal.

Again thanks to all the member of group and special thanks to Mohammad.

List of publications

Journal papers:

1. A. Khorsandi, U. Willer, P. Geiser, and W. Schade. MIR-difference-frequency laser spectrometer for CO detection in combustions. *Iranian J. of Phys. Res.,* Vol. 3, No. 4, 97-100, 2003.

2. A. Khorsandi, U. Willer, P. Geiser, and W. Schade. External short-cavity diode-laser for MIR difference-frequency generation. *Appl. Phys. B* **77**, 509-513, 2003.

3. L. Wondraczek, A. Khorsandi, U. Willer, G. Heide, W. Schade, and G. H. Frischat. Mid-infrared laser-tomographic imaging of carbon monoxide in laminar flames by difference frequency generation. *Combustion and Flame*, **138**, 30-39, 2004.

4. L. Wondraczek, A. Khorsandi, U. Willer, G. Heide, W. Schade, and G. H. Frischat. Mid-infrared absorption spectroscopy for process and emission control in the glass melting industry. Part 1: Potentials. *Glass Sci. Technol.* **77**, No. 2, 68-76, 2004.

5. L. Wondraczek, A. Khorsandi, U. Willer, G. Heide, W. Schade, and G. H. Frischat. Mid-infrared absorption spectroscopy for process and emission control in the glass melting industry. Part 2: Difference frequency generation based MIR laser spectrometer for glass melting furnaces. *Glass Sci. Technol.* **77**, No. 3, 131-136, 2004.

6. A. Khorsandi, U. Willer, L. Wondracezek, and W. Schade. In-situ and on-line monitoring of CO in an industrial furnace by MIR-DFG laser spectroscopy. *Appl. Opt.*, accepted.

Conference contributions:

1. L. Wondraczek, A. Khorsandi, P. Geiser, U. Willer, G. Heide, W. Schade, G. H. Frischat. On-line und in-situ-laserspektroskopie der Ofenatmosphäre in Glasschmelzöfen. *GlassTec*2002, *Düsseldorf*, 2002.

2. U. Willer, A. Khorsandi, P Geiser, L. Wondraczek, W. Schade. MIR-Laserspektroskopie zur Bestimmung dreidimensionaler Konzentrationsprofile von Kohlenstoffmonoxid in Flammen. ***DFG*** *Frühjahrstagung, Hannover,* 2003.

3. L. Wondraczek, A. Khorsandi, G. Heide, W. Schade, G. H. Frischat. Laserspektroskopische Verfahren zur Hochtemperaturgas analytik im mittleren IR. *77te Glastechnische Tagung der* ***DGG****, Leipzig*, 2003.

4. A. Khorsandi, U. Willer, P. Geiser, L. Wondraczek, W. Schade. 3-dimensional imaging of CO in a flame by mid-infrared laser spectroscopy. *Conference on Lasers and Elactro-Optics in Europe (****CLEO/Europe****), München,* 2003.

5. U. Willer, A. Khorsandi, L. Wondraczek, W. Schade. Mid-infrared sensing of carbon monoxide in induastrial glass-furnaces. *Laser applications to chemical and environmental analysis,* ***OSA****, Annapolis,* 2004.

6. C. Bohling, C. Romano, A. Khorsandi, U. Willer, W. Schade, M. Rich, H. Zellmer, A. Tünnermann. Verstärkung von Cr^{4+}:Nd^{3+}:YAG Microchiplaserpolsen in einem Yb-Faserverstärker. ***DPG*** *Frühjahrstagung, München,* 2004.

7. U. Willer, A. Khorsandi, P. Geiser, C. Bohling, L. Wondraczek, W. Schade. Laser spectroscopy in high temperature combustions. ***OPDI Mon'04***, *Bacoli*, 2004.

Eidesstattliche Erklärung

Hiermit erkläre ich an Eides statt, daß ich die vorgelegte Arbeit selbständig, ohne unerlaubte Hilfe verfaßt und die benutzten Hilfsmittel vollständig angegeben habe.

Clausthal-Zellerfeld, Alireza Khorsandi

Eidesstattliche Erklärung

Hiermit erkläre ich an Eides statt, daß ich noch keine früheren Promotionsversuche unternommen habe.

Clausthal-Zellerfeld, Alireza Khorsandi